Entangled Polymer Melts in Extensional Flow: Synthesis, Rheology, Neutron Scattering

Dorokhin, Andriy

Publication date:
2018

Document Version
Publisher's PDF, also known as Version of record

Entangled Polymer Melts in Extensional Flow:

Synthesis, Rheology, Neutron Scattering

Andriy Dorokhin

PhD Thesis December 2017

DTU Nanotech
Department of Micro- and Nanotechnology

Ph.D. Thesis
Doctor of Philosophy

DTU Nanotech
Department of Micro- and Nanotechnology

Entangled Polymer Melts in Extensional Flow:

Synthesis, Rheology, Neutron Scattering

Andriy Dorokhin

Kongens Lyngby 2018

DTU Nanotech
Department of Micro- and Nanotechnology
Technical University of Denmark
Produktionstorvet, 423
2800 Kongens Lyngby, Denmark
www.nanotech.dtu.dk

Preface

The thesis was prepared in fulfillment of the requirements for acquiring a Ph.D. degree. Its manuscript presents the results of the work that was carried out at the Department of Micro- and Nanotechnology (Technical University of Denmark), Niels Bohr Institute (University of Copenhagen), Danish Polymer Centre (Technical University of Denmark), Bragg Institute (Australian Nuclear Science and Technology Organisation) and Paul Scherrer Institute (Swiss Federal Institutes of Technology Domain).

The Ph.D. project was supervised by Prof. Kristoffer Almdal (Department of Micro- and Nanotechnology, main supervisor), Prof. Kell Mortensen (Niels Bohr Institute) and Prof. Ole Hassager (Danish Polymer Centre).

This study is a part of the joint project 'Entangled Polymer Melts in Extensional Flow' between DTU Nanotech, DTU Chemical Engineering and the Niels Bohr Institute at Copenhagen University which was supported by the Danish Council for Independent Research — Natural Sciences (Grant 0602 — 02179B). The research programme comprises experimental work in model polymer synthesis, extensional rheology, small-angle neutron scattering as well as fitting the data from the SANS scattering patterns.

Summary

This thesis contains 5 chapters and reprints in Appendices, combined of both published and unpublished materials.

The first chapter is an introduction to the goals, methods and problem identification of the project of the entangled polymer melts in extensional flow, which is aimed to shed some light on certain aspects of polymer physics. This became possible because of a valuable opportunity of collaboration of scientists, whose main research areas are polymer synthesis, rheology of complex fluids and small-angle neutron scattering.

Consequently, the second chapter describes the model polymer syntheses, made by living anionic polymerization. It contains the description of well-established, as well as new block copolymer syntheses.

The third chapter briefly touches the area of the extensional rheology of complex fluids and has the description of an innovative method, filament stretching rheometry, which can measure the extensional rheology of non-Newtonian fluids during a homogeneous uniaxial elongation, providing the results for the tensile stress and molecular conformations.

Forth, the fourth chapter delineates the area of SANS, provides the characteristics of the instruments from the different beamlines and depicts some issues that are significant and specific to the quenched polymer samples. It also contains the computational algorithms of the polymer structure factors and shows the way to procure essential parameters of the macromolecular conformations.

The conclusion, Chapter 5, briefly recapitulates the progress in the area of the project.

Dansk Resumé

Denne afhandling indeholder 5 kapiteler og genoptrykt i Appendikser, både udgivet og ikke publiceret materiale.

Det første kapitel er en introduktion til formål, metoder og problemer identificeret i projektet, der omhandler komplexe polymersmelter i forlængelse flydning, i forsøg på at kaste lys over visse aspekter af polymerfysik. Dette blev muliggjort ved hjælp af et værdifuldt samarbejde mellem forskere, hvis vigtigste forskningsområder er polymersyntese, reologi af komplekse væsker og små-vinkel neutronspredning.

Følgeligt beskriver andet kapitel model polymersynteser, udført ved levende anionisk polymerisation. Det indeholder beskrivelse af veletablerede, samt nye blokcopolymersynteser.

Det tredje kapitel berører kortvarigt forlængleses reologi af komplekse væsker og beskriver en innovativ metode, strakt tråd reometri, som kan måle reologi af ikke-Newtonske væsker under en homogen uniaksial forlængelse, der giver resultater for trækspændingen og molekylære konformationer.

Yderligere, det fjerde kapitel afgrænser området for SANS, samt indeholder de særlige kendetegn ved instrumenterne fra de forskellige beamlines og beskriver nogle spørgsmål, der er væsentlige og specifikke for bratkølete polymerprøver. Det også præsenterer de beregningsmæssige algoritmer for polymerstrukturene og viser en måde at bestemme væsentlige parametre for de makromolekylære konformationer på.

Konklusionen, Kapitel 5, opsummerer kort fremskridt inden for projektet.

Acknowledgements

I would like to thank my Ph.D. supervisors: Prof. Kristoffer Almdal for teaching me the basics of anionic polymerization, tactics and strategies of a good researcher and inspiration throughout these 3 exciting years, Prof. Kell Mortensen for introducing me to the area of small-angle neutron scattering and Prof. Ole Hassager for providing an insight on the concepts of extenstional rheology of complex fluids.
I would further like to thank Prof. Jacob Kirkensgaard for the great help in both experimental and theoretical part of SANS, specifically for the part of implementing the 'Dangling Ends Model' into a Matlab code, as well as backing with finding bugs in programming code; Dr. Irakli Javakhishvili and Dr. Sergey Chernyy for the enlighting discussions in the field of polymer chemistry; Dr. Ludovica Hengeller and Dr. Qian Huang for enlightening me in some areas of polymer rheology and hands-on FSR training; all the lecturers from the '14th Oxford School on Neutron Scattering' and 'Applications of X-ray and Neutron Scattering in Biology, Chemistry and Physics' course, as well as Prof. Henrik Flyvbjerg, Prof. Bo Svensmark, Dr. Nikoline Juul Jensen, Prof. Charlotte Held Gotfredsen, Prof. Jens Øllgaard Duus, Prof. Andy Horsewell, Prof. Wolfgang Pantleon, Prof. Karen Pantleon and Prof. Masao Doi for their input into my education.
Also I would like to thank Lotte Nielsen and Ole Kristoffersen for technical assistance and help with the instruments used during my experimental work.
Finally, I am gratefully thankful to my wife Oks-ksana Nezajchonovna Rækshukhena Tikho-BRæs-Khaøshaja for the proof-reading of the draft of this thesis.

List of Acronyms

Acronym	Definition
3BnBr	1,3,5-Tris(bromomethyl)benzene
ANSTO	Australian Nuclear Science and Technology Organization
AcOH	Acetic acid
AgTFA	Silver trifluoromethanesulfonate
ATRP	atom transfer radical polymerization
BHT	2,6-Di-*tert*-butyl-4-methyl-phenol
Bu_2Mg	Di-n-butylmagnesium
CCR	convective constraint release
CLF	contour length fluctuations
CR	constraint release
CRR	constraint release Rouse
DEM	'dangling ends' model
DPE	Diphenylethylene
DPEBr1	1,3-Bis(1-phenylvinyl)benzene
DPEBr3	1-(4-(3-Bromopropyl)phenyl)-1-phenylethylene
DRI	differential refractive index
DTD	dynamic tube dilation
DVB	Divynilbenzene
Dithranol	1,8-Dihydroxy-9(10H)-anthracenone
FSR	filament stretching rheometry/rheometer
GLaMM	Graham-Likhtman and Milner-McLeish Model
HCl	Hydrochloric acid
HPLC	High-performance liquid chromatography
iPrOH	Propan-2-ol
Irganox 1010	Pentaerythritol *tetrakis*[3-(3',5'-di-*tert*-butyl-4'-hydroxyphenyl)-propionate]
Irganox 1330	1,3,5-Trimethyl-2,4,6-tris(3,5-di-tert-butyl-4-hydroxybenzyl)benzene
ISO	International Organization for Standardization
KOH	Potassium hydroxide
LVE	linear viscoelasticity
MALDI ToF MS	matrix-assisted laser desorption/ionization time-of-flight mass spectroscopy
MLD	Mead, Larson and Doi theory
MeOH	Methanol
NMP	nitroxy-mediated stable free-radical polymerization
P2VP	poly(2-vinyl pyridine)

Acronym	Definition
PB	polybutadiene
PDDPE	Para-double diphenylethylene/1,4-Bis(1-phenylethenyl)benzene
PI	polyisoprene
PP	chain primitive path
PRMA	substituted polymethacrylate
PS	polystyrene
PS-*d8*	perdeuterated polystyrene
PSD	deuterated polystyrene block
PSH	protonated polystyrene block
PSI	Paul Scherrer Institute
PSLi	polystyryllithium
RAFT	reversible addition–fragmentation chain transfer polymerization
RALLS	right angle laser light scattering
ROP	ring-opening polymerization
SANS	small-angle neutron scattering
SEC	size exclusion chromatography
sec-BuLi	*sec*-butyllithium
TCR	thermal constraint release
THF	Tetrahydrofuran
WEM	Warner-Edwards model

Contents

CHAPTER 1

Review

1.1 Timeliness and Open Questions of this Work

Theoretical rheology is a discipline of great significance for the industrial polymer processing. It describes the viscoelastic behaviour of a complex fluid based on a macromolecular structure of a material [1]. The discipline leans on the theoretical framework of one-dimensional diffusion and the Tube Model concept established by the pioneering works of de Gennes, Doi and Edwards [2, 3]. Since then, a handful of significant improvements, based on the data from rheological experiments, have been suggested. The enhancements in linear response include: contour length fluctuations [4], thermal constraint release [5, 6] and longitudinal Rouse modes [7], which were incorporated into a comprehensive model by Likhtman and McLeish [7]. The nonlinear response was further developed by adding the processes of chain stretch [8, 9] and convective constraint release [10]. Onwards, Graham et al. [1] added the mechanisms for nonlinear mode to the Likhtman theory, and made a complementary nonlinear model, that is able to predict the variation in rheological response depending on the molecular weight, chemical composition and deformation geometry. Despite the success in understanding flow and diffusion in macromolecular ensembles there is evidence of inability to prognosticate the molecular processes and rheological properties outside a small deformation range, especially for the case of extensional flow in elongation [11]. On the other hand, the development and validation of a quantitative, microscopic theory that can resolve this obstacle depends crucially on the availability of experimental and simulation data for model systems [12]. This work aims at providing the needed experimental data on stress and macromolecular orientation measurements of model polymers and polymer melts systems during a controlled uniaxial extension. In more detail, we target model branched architectures since we would like to exclude reptation relaxation mechanism and push these systems into the non-linear regime. In such a manner it is possible to fill a missing data gap in the field of molecular rheology of complex fluids and broaden our understanding in the specific area of extensional flows. To achieve these goals the method of living anionic polymerization is utilized, forasmuch as it can offer a well-established way to produce a satisfactory amount of appropriate labeled, stable, narrowly polydispersed high molecular mass polymers with a targeted molecular architecture. The monomers suited for our research need to meet at least some of the certain requirements stated below:

- A monomer has to have a commercially available deuterated analogue, which relieves us from the necessity to synthesize the deuterated version of the monomer ourselves. The advantageous analogue has to be a perdeuterated one since it will give more contrast during SANS measurements;
- The price of a monomer and its deuterated analogue has to be reasonable;
- A final polymer made of a chosen monomer preferably has a relatively high glass transition temperature, slightly higher than a maximum temperature it can encounter after

the quenching procedure on FSR. Meeting this requirement allows easy handling of the final sample with no necessity to cool it down with liquid nitrogen or dry ice to save the macromolecular conformations after the quenching;

- A monomer and a resulting polymer have to be stable at a certain temperature range. The most critical part of this is that the resulting polymer must not have to degrade at a temperature around fifty degrees above the glass transition temperature, since it is the temperature to prestretch a sample on FSR;
- The chemistry of the polymerization should be well studied and practically feasible in our laboratory with as little byproducts and competitive reactions as possible;
- The reactivity of living linear chains has to be enough to make a POM-POM or star-coupling reactions with high yields to produce high molecular weight polymers (for a POM-POM polymer made of styrene the desired molecular weight for an arm is 20 kg/mol since it is a little bit higher than the entanglement molecular weight, minimum amount of arms is equal to four and the linker connecting the arm should be five times higher in molecular weight, which results in the final molecular weight of 180 kg/mol).

Keeping all those criteria in mind, the monomer for the study was chosen to be styrene, since it satisfies to some extent all the stated requirements. Polymers are uniaxially elongated at a controlled temperature and under inert atmosphere with an online feedback control plate motion with the use of a filament stretching rheometer at a constant elongation rate, and either quenched immediately or after the stress relaxation for a determined amount of time. These kinds of experiments give reproducible data on extensional viscosity of the systems scrutinized. The data is then being associated with structural studies by SANS, providing insight on to which extent the macromolecules were strained by the flow field. In such a manner, we provide novel essential data for developing a molecular model describing the behaviour of non-Newtonian fluids under uniaxial deformation at high strain rates.

1.2 General Background and Phenomenological State-of-the-art

1.2.1 General Polymer Description

Polymer rheology is aimed to provide theoretical understanding of the dynamics and mechanics of soft matter materials in order to meet the demands of the polymer producing market, as well as a diverse set of minor problems going far beyond, such as: chromosome dynamics, cytoskeleton mechanics and protein folding [13]. Rheology involves measurements in controlled flow situations gaining information about viscosity and elasticity of complex fluids and providing crucial information on the behavior of polymeric liquids [14].

In order to describe polymers and their deformations a well-established conceptual construct comprising of conventional ideas and ratiocinations has to be declared first.

A polymer (macromolecule) is a molecule composed of repeated subunits. A polymer in equilibrium tends to take on random walk coil configuration with step size of b_K consisting of N_K random steps (Kuhn steps).

The extended polymer length (also called 'contour length') is described by the equation:

$$L = N_K b_K, \tag{1.1}$$

and the root mean square distance between the macromolecule ends is then equal to

$$R = \langle R^2 \rangle_0^{0.5} = N_K^{0.5} b_K \tag{1.2}$$

A macromolecule can be maximum stretched up to [15]:

$$\lambda_{\max} \equiv L/\sqrt{\langle R^2 \rangle_0} = \sqrt{N_K} \tag{1.3}$$

1.2.1.1 Entanglement

Entanglement (topological constraint) may be introduced as a phenomenological entity designated for long-lived binary dynamic interactions between pairs of polymer chains [16]. Even though the definition of entanglement as well as its precise nature are not completely understood or agreed upon until now [15], theories that exploit ideas of effects of entanglements make predictions about polymer rheology closer to experimental data. For example, in cases of concentrated solutions or melts, the use of mathematical apparatus of entanglements gives the ability to correctly describe intermediate time rubbery plateau of the dynamic shear modulus in the liquid state, which is analogous to crosslinked rubbers [13]. The value of the entanglement molecular weight in a polymer, M_e, is found experimentally: from plateau modulus, relating M_e to chain dimensions [17] or to packing length and density [18]:

$$M_e = 1.98 N_A \rho l_p^3, \tag{1.4}$$

with 1.98 being the coefficient of proportionality, which is independent of polymer type and temperature [19]. This experimentally found coefficient holds for a variety of flexible polymers, such as: polydienes, styrenes, acrylics and polymeric sulfurs [20–24].

The plateau modulus is defined [15] as $M_e \equiv \rho RT/G_N^0$, which means that

$$G_N^0 = \frac{kT}{1.98 l_p^3} \tag{1.5}$$

where k is Bolzmann's constant, l_p, packing length (which is proportional to the ratio of the cross-sectional area to the length of each Kuhn segment [25]), is defined as

$$l_p = \frac{M}{r_g^2 \rho N_A} \tag{1.6}$$

with r_g being a radius of gyration, N_A — Avogadro constant, ρ — polymer density.

Volume per entanglement, V_e, is the volume that occupies a macromolecule with the molecular weight of M_e:

$$V_e = \frac{M_e}{\rho N_A} \tag{1.7}$$

and introducing M_e from Eq. 1.4 it gives:

$$V_e = 1.98 l_p^3 \tag{1.8}$$

The number of entanglements per chain Z determines the linear response of a polymer and is found as the ratio of Kuhn segments in the chain N over Kuhn segments per entanglement segment N_e [26]:

$$Z = \frac{N}{N_e} = \frac{M_w}{M_e}, \tag{1.9}$$

For the complete image, M_w and M_e are given, which are the molar masses of the chain and entanglement, respectively.

The number of Kuhn segments per entanglement N_e determines to some extent nonlinear flow characteristics providing an estimate of the rigidity of entanglement segment. In a polymer melt N_e is preconditioned by the chemistry of a polymer, while adding a solvent will increase the space between entanglements simultaneously increasing the number of Kuhn segments per entanglement ($N_e(\phi)$) [26]:

$$N_e(\phi) = N_e(1)\phi^{-\alpha}, \tag{1.10}$$

with ϕ being polymer concentration, $N_e(1)$ — the number of Kuhn segments per entanglement segment for the undiluted system and α being the dilution exponent [26].

Even though a detailed description of the Tube Model is given in the following subsections, important variables introduced there are used universally and need to be declared here. A virtual tube consisting of the surrounding molecules restricting motions of chains has a diameter d_t (also called an average transverse dynamic localization length) defined by:

$$\frac{d_t^2}{M_e} = \frac{R^2}{M}, \tag{1.11}$$

with M being overall molar mass and R^2 — end-to-end vector, may be more conveniently used as:

$$d_t = l_p n_t/6 = n_t^{1/3} V_e^{1/3} \tag{1.12}$$

with n_t being the number of Kuhn segments per M_e and l_p being obtained from SANS measurements of chain dimensions [24, 27]. Tube diameter is a fundamental length scale for a macromolecule depending only on polymer chemistry, concentration and amount of monomeric units [13] which is used in Tube Model [Sec. 1.2.3] to predict the large-scale behavior of chains in a polymer melt [28].

Another valuable variable is critical molecular weight, M_c, after which the zero-shear viscosity starts having power law function depending on M. This value is fitted empirically [25]:

$$M_c = M_e[l_p^*/l_p]^{0.65} \tag{1.13}$$

with l_p^* value of approximately 6 nm. M_c ticks the crossover from unentangled polymer behavior (called 'regime 1') to entangled regimes (regime 2 — reptation combined with other processes like 'contour length fluctuations' and 'constraint release'; regime 3 — pure reptation) [28]. Above the critical molecular weight in a melt or higher than the entanglement concentration in solution, the Brownian motion of a polymer chain happens in less than three-dimensional space [29], which will be more thoroughly described within the Tube Model subsection.

1.2.2 Rouse Model

Originally proposed to describe the macromolecular dynamics in dilute solutions, the Rouse model [30] or its later successor, the Zimm model [31], which includes hydrodynamic interactions, correctly describes dynamics of short polymer chains in melts and solutions. For example, macromolecules shorter than the entanglement length n_e show the self-diffusion constant and viscosity for a melt of chains of length n proportional to n^{-1} and n respectively, which was predicted by the Rouse model [32]. The Rouse model may predict the dynamics in concentrated solutions in case of the $M_w < M_e$, since hydrodynamic interactions are screened

out by other molecules [33], or even the dynamics at intermediate time and length scales, while the dynamics at longer scales is affected by the temporary topological constraints [34].

In the Rouse model, a polymer chain is represented as a set of beads with defined coordinates R_i and friction coefficient ξ_0. The beads are interconnected using harmonic springs with constant $k = \frac{3k_BT}{b^2}$, where b^2 is the mean-squared length of each bond. For a bead i the equation of motion is [35]:

$$\xi_0 \frac{dR_i}{dt} = \frac{3k_BT}{b^2}(R_{i+1} + R_{i-1} - 2R_i) + f_i(t), \tag{1.14}$$

with $\langle f_i(t)\rangle = 0$ and $\langle f_i(t) f_j(t')\rangle = 2k_BT\xi_0\delta_{ij}\delta(t-t')$.

Despite its success, the Rouse model is not a universal answer to the subject of polymer dynamics of unentangled chains, since it breaks down in cases when the length scale probed by a mode is too short to allow for Gaussian distributed intramolecular distances on that scale [36], when a length scale is affected by local excluded volume interactions and chain stiffness [34], or at temperatures close to the glass transition, where the relaxation time of local segments has stronger temperature dependence than that of Rouse normal modes [33].

Some improvements were introduced to the Rouse model in order to account for the increase in relaxation time in the viscoelastic response of an unentangled polymer melt undergoing a glass transition by fitting a temperature dependent monomer friction coefficient in the form of a Vogel-Fulcher-Tammann law [36]:

$$\zeta(T) = \zeta_\infty \exp\left[\frac{E}{T - T_0}\right], \tag{1.15}$$

with T_0 being the extrapolated temperature of divergence and ζ being monomer friction coefficient.

Summarizing, the Rouse model is an isotropic oversimplification that does not correctly describe macromolecular behavior because of the effects of hydrodynamics in solutions, entanglements in long chain liquids and nonlocal viscoelastic effects near the glass transition temperature [13]. This became motivation behind an enhanced segment-scale, self-consistent, force-based theory model with intermolecular force memory function matrix which captures arrested segmental correlations that are nonlocal in separation along a tagged chain [13].

1.2.3 Tube Model

Originally presented by de Gennes [2] and developed further by Doi and Edwards [3], the Tube Model simplifies interpenetrations of chains and entanglements effects that restrict their motion into a tube-like region around the chain [37].

Having two ends, a linear chain (chain primitive path, PP) undergoes Rouse dynamics inside the tube and may curvilinearly diffuse forwards and backwards along the axis of this tube. This quasi-1D stochastic motion, which is responsible for chain diffusion as well as flow and long-time relaxation was named reptation [13].

The phenomenon of reptation has been lately evidentiated directly with the use of fluorescence microscopy, acknowledging the relaxation mechanism without transversal movements [38].

The key parameter, that is introduced in tube theory is a tube diameter or, rather, the ratio of the tube diamater to the global polymer size [16]. In entangled polymer melts the number of monomers along the chain between neighboring entanglements N_e and a microscopic

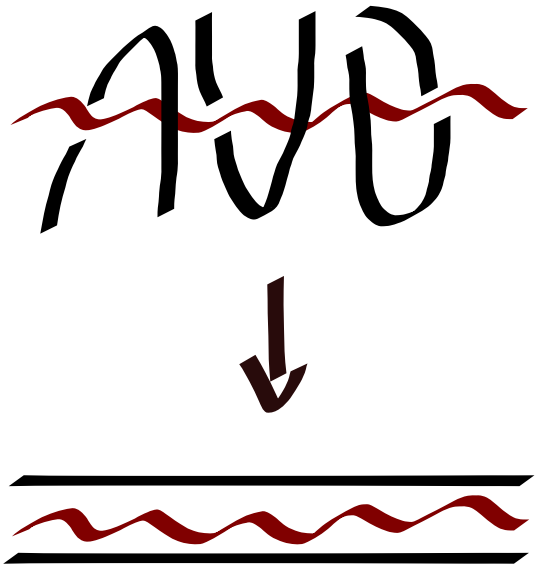

Figure 1.1: The concept of the tube: chain interpenetrations (black color, top) make a so-called 'tube' (black color, bottom) around a polymer chain (dark red).

length scale for one monomer a are introduced to calculate the tube diameter [39]:

$$d_t = aN_e^{0.5} \tag{1.16}$$

It was shown that in solutions the tube diameter is decreasing with increasing concentration [38]. Even though present phenomenological theories [40, 41] are exploiting the idea of non-deformable, non-intrinsically dynamical tubes with the exception of deformations following the macroscopic affine strain, the concept of tubes changing their diameter may help to interpret some macroscopic experiments [16].

In case of long chains the process of chain stretching, occurring on the time scale of τ_R, may be decoupled from the process of chain orientation, occurring on the time scale of τ_d. This means that in case of external deformation rate $\dot{\gamma}$ higher τ_d^{-1} and lower than τ_R^{-1} the Tube Model mostly predicts chain orientation and not as much chain stretching during the shear deformation, leading to such deductions as: the radius of gyration should increase monotonically during startup shear, the contour length of the PP and stress for step shear should decline on time scales of τ_R and the chain alignment in the tube should result in stress overshoot [37].

The improved Tube Model [Sec. 1.2.4] predicts the scaling of zero-shear viscosity η_0 depending on the M_w of the chain [28]:

- providing expected viscosity proportional to M_w in case of chain molecular weight less than critical molecular weight;
- proportional to the M_w^3 in case of chain molecular weight greater than the reptation molecular weight M_r;
- proportional to $M_w^{3.4}$ if the molecular weight of a chain is in between of the critical molecular weight, M_c, and M_r for monodisperse homopolymer melts with linear architecture.

The state-of-the-art expression for the relaxation modulus also accounts for the following supplementary mechanisms [42]:

- First term — constraint release term;
- Second term — longitudinal relaxation of segments;
- Third term — fast Rouse relaxation of segments within the tube.

$$G(t) = G_e \left[\frac{4}{5}\mu(t)R(t) + \frac{1}{5Z}\sum_{p=1}^{Z-1} \exp\left(-\frac{p^2 t}{\tau_R}\right) + \frac{1}{Z}\sum_{p=Z}^{N} \exp\left(-\frac{2p^2 t}{\tau_R}\right) \right], \tag{1.17}$$

with $G_e = \rho RT/M_e$ being the plateau modulus, $\mu(t)$ — single chain relaxation function, $R(t)$ — relaxation function due to constraint release, $\tau_R = \tau_e Z^2$ — the Rouse time of a chain in a tube and p denoting a relaxation mode.

A significant part of this work was devoted to the synthesis and rheo-SANS characterization of star polymers, which show different rheological response, particularly, a logarithmically decaying plateau for $G(t)$. Since on account of the branching point a polymer can not reptate, the relaxation of star polymers within the Tube Model is described with the help of thermal constraint release and arm retraction, yielding in an expression for stars zero-shear viscosity [42]:

$$\eta_0 \approx G(\tau_{arm})\tau_{arm} \sim \left(\frac{M_{arm}}{M_e}\right)^{1.5} \exp\left(\frac{\gamma'}{2}\frac{M_{arm}}{M_e}\right), \tag{1.18}$$

with γ' being a constant set to 3/4.

1.2.3.1 Relaxation Times

Time constants describe polymer motion after chain stretch:

- τ_e (entanglement time) points at the empirical crossover from the short length scale relaxation to the regime that is affected by topological constraints, which can also be defined as the relaxation time of the strand between two entanglements [43];
- τ_R (Rouse relaxation time) is the longest chain relaxation time for a given chain length and reptation time;
- τ_d (reptation time) is the time it takes a chain to diffuse out of its original tube [44].

1.2.3.2 Tube Model Criticism

The Tube Model describes polymer dynamics problems of flow and equilibria properties of multiple chains in simplistic and mathematically convenient terms, simplifying a many-body problem into a single chain problem. Such reduction, as well as assumptions of nondeformability of the tube, lower the power of the theory to describe experimental data [45]. Selected studies [46–48] have shown that a tube is dynamic in its nature and some reconsiderations have to be made in this model.

The Tube Model also does not include such essential processing parameters as temperature, concentration, density and degree of semiflexibility in its core approximating these

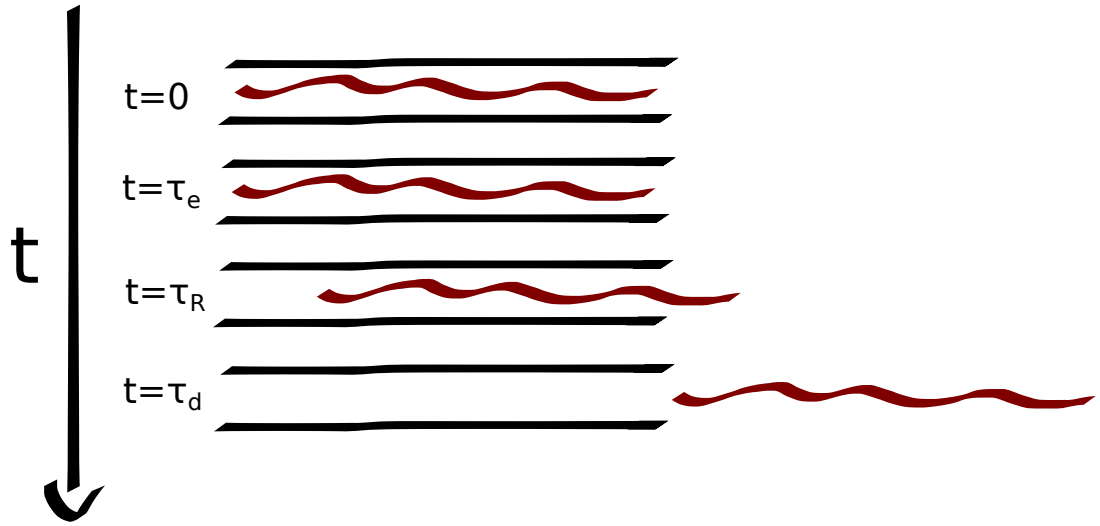

Figure 1.2: Polymer motion with respect to the relaxation times: τ_e being the entanglement time, τ_R — Rouse relaxation time and τ_d — reptation time.

correlations into a 'confining tube', while other theories [49, 50] include the dynamics of entanglements as interacting chains.

At this point, a heterogeneous set of equations (Rouse and reptation models) is employed to depict polymer rheology for unentangled and entangled polymers, while neither the thermodynamics nor the structural properties of polymers show any dynamics discontinuity, indicating the situation of present microscopic formalism that does not properly represent the polymer dynamics [51].

1.2.4 Tube Model enhancements in linear response

1.2.4.1 Contour Length Fluctuations

The Tube Model predictions [52] were contradicting experimental data [53, 54], so a number of supplements were introduced as the model enhancements to quantitatively address observed aspects in properties of linear entangled macromolecules [55].

In order to correctly describe linear viscoelasticity (LVE), particularly the dependence of M (above M_e) on zero shear viscosity with the scale of $(M/M_e)^{3.4}$ instead of predicted $(M/M_e)^3$ [56] the concept of contour length fluctuations ('the fluctuation-driven stretching and contractions of the chain along the tube', 'CLF') was proposed [52]:

$$\eta_0(M) = 9.6\eta_0(M_c)(M/M_c)^3[1 - 1.04(M_c/M)^{0.5}]^3, (M \gtrsim 10M_c,) \tag{1.19}$$

with $M_c = 2M_e$, which is numerically close to the empirical power law, $\eta_0(M) = \eta_0(M_c)(M/M_c)^{3.4}$ for $10M_c \lesssim M \lesssim 100M_c$.

The message of CLF is that at the point of chain contraction and stretching within the tube, the orientation of the ends of the tube is 'forgotten' and stress associated with the alignment of those parts of the tube is already relaxed [57].

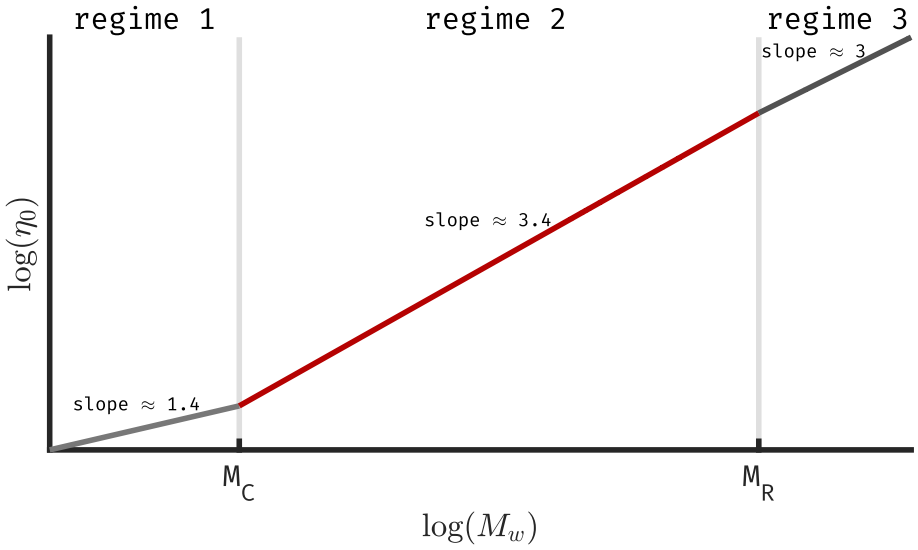

Figure 1.3: Expected zero shear viscosity profiles for polymer solutions at different molecular weights. M_c and M_r represent the critical and reptation molecular weights respectively.

It is worth noticing that CLF mechanism of stress relaxation is significant only for a certain chain length and beyond a limit of M_r the effect fades away leaving pure reptation as the only way for stress relaxation [28].

1.2.4.2 Thermal Constraint Release

Tube reorganization by the way of thermal constraint release (CR) was originally introduced to describe polydispersity effects [42, 58]. At this point, among different theories behind the CR model, the release of constraints on a test chain, as other chains retract away from their environment, providing effective widening of the tube following a step strain is widely accepted because of good agreement between the theory and experiments [59]. The CR effects are treated supposing that relaxed segments work as a solvent for strained chains, that reduces the number of entanglements in the system by a factor of $(1 - s)$ resulting in a gradual dilation of the confining tube. This relaxation mechanism, 'dynamic tube dilation' (DTD), reasonably predicts the stress relaxation function for monodisperse linear and symmetric polymer stars, but not the dielectric or arm end-to-end vector relaxation [60]. A possible explanation of these deficiencies could be that a tube dilation process occurs faster than the transverse Rouse motion of the arm when the dangling end retracts [60]. In order to account for these errors, a multichain 'slip-link' model was proposed, which assumes entanglements as topological constraints coming from pairs of neighboring chains while the relaxation in terminal regime is governed by the creation of entanglements between the branch point and the inmost entanglement is pushing the original entanglements towards the arm ends allowing them to vanish by shallow arm retractions [60].

1.2.4.3 Longitudinal Relaxation of Segments

Another significant contribution to stress relaxation at short times, the longitudinal relaxation modes, may elucidate the 4/5 factor in the plateau modulus expression $G_N^0 = (4/5)\rho RT/M_e$ in the frequency region of the minimum of the loss modulus G'' [58].

The factor is taken from the Doi-Edwards theory prediction, where it shows that the plateau modulus has to be 4/5 of the rubber modulus, with 1/5 of the stress being stored in the tubes and relaxed after deformation by longitudinal motion along the tube [7].

1.2.5 Tube Model enhancements in nonlinear response

The original Tube Model is a constantly developing theory, aiming to explain such experimental phenomena in nonlinear polymer melt/solution deformation, as [15]:

- Shear thinning (nonlinear flow rate/stress/pressure drop, shear banding, wall slip);
- Normal stress differences in shear (rod climbing, edge fracture in torsional shearing flow, elastic instabilities);
- Extensional thickening (tubeless siphon flow, turbulent drag reduction);
- Nonlinear memory of the deformation history (large elastic recoil, extrudate swelling, fluid bouncing).

To account for some of these phenomena, such mechanisms as convective constraint release (CCR) and chain stretch were introduced to the description of entangled polymers behavior in nonlinear flow [55].

1.2.5.1 Convective Constraint Release

In strong flows regimes (e.g. $\dot{\gamma}_0\tau_d \gg 1$), the relative chain motion removes entanglements allowing faster relaxation. This phenomenon was named convective constraint release (CCR) and included to the Doi-Edwards model, making shear stress predictions approach a plateau at higher shear rates which agrees better with experimental observations [45]. The mechanism was initially developed to attenuate predicted excessive shear thinning leading to an unstable flow curve [58]. The release of topological constraints is believed to originate from the continual retraction of the chain contour length, that was generated by a flow. While being stretched, entangled chains are also relaxing to equilibrium by retracting along their tubes, making steady flow a superposition of continuous stretch and relaxation. Therefore the topological constraints are relaxed together with chains at a certain rate. This mechanism needs anisotropic chain conformations to operate, thus emerging in strain rate at second order [61]. Also, the original tube theory mismatch in ratio $-\Psi_2/\Psi_1$ (Ψ_1 and Ψ_2 being the first and second normal stress differences) in the slow shear rate regime was also corrected with a new strain measure $\mathbf{Q} = \mathbf{C}^{-0.5}/tr(\mathbf{C}^{-0.5})$ instead of tensor $\mathbf{Q} = \langle \mathbf{uu} \rangle$ in the original theory [45].

1.2.5.2 Constraint Release Rouse

Constraint release motion may also have a different microscopic mechanism laying in hopping motion of the tube on the time scale of the frequency of constraint release events, where the tube undergoes Rouse motion mediated by constraint release, scaling as the inverse constraint release rate times n^2, with n being the number of steps of PP, $n = Nb^2/t_d^2 = 5/4N/N_e$, N — chain length and b — chain Kuhn segment [61].

1.2.5.3 Chain Stretch

The stretched chain accelerates reptation proportional to the chain length because a monomer diffuses longer to relax stress in a stretched (longer) chain. To account for this relaxation mechanism, the displacement because of reptation is reduced by $Z/Z^*(t)$, with $Z^*(t)$ being the number of tube segments of stretched chain, giving a reptation term [41]:

$$\mathbf{R}(s,t+\Delta t) = \mathbf{R}\left(s + \frac{Z}{Z^*(t)}\Delta\xi(t), t\right) \tag{1.20}$$

with $R(s,t)$ being the space curve denoting the position vector of tube segment s at time t and with $Z^*(t)$ being the instantaneous number of entanglements defined as:

$$Z^*(t) = \int_0^Z \sqrt{\langle \mathbf{R}'(s)\cdot\mathbf{R}'(s)/a^2\rangle}\,ds = \frac{1}{a}\int_0^Z \sqrt{Tr\mathbf{f}(s,s)}\,ds, \tag{1.21}$$

assuming that

$$\langle\sqrt{\mathbf{R}'(s)\cdot\mathbf{R}'(s)}\rangle \approx \sqrt{\langle\mathbf{R}'(s)\cdot\mathbf{R}'(s)\rangle} \tag{1.22}$$

1.2.6 GLaMM Model

GLaMM (Graham-Likhtman and Milner-McLeish) Model [41, 62] is the most up-to-date mesoscopic model [63], which implements the relaxation mechanisms of reptation, CLF, CR (thermal and convective [10, 64]) and chain retraction at the length scale of the tube diameter [65], providing a microscopically derived stochastic equation for the macromolecular dynamics of a chain in its mean field tube [66]. It features the change of the ensemble-averaged conformational correlation between the segments of the primitive path and its neighbors, while previous works [67, 68] still handle the segments as uncorrelated [69]. Also, in contrast to MLD theory [67], in the GLaMM Model CR is being implemented as a completely distinct relaxation mechanism — local hops of the tube — which arises from lateral hops of the tube on the length scale of the tube diameter leading to Rouse-like motion of the tube itself [65]. Mathematically the GLaMM Model is described as the sum of convention:

$$\frac{\partial f}{\partial t} = \cdot\,\mathbf{f} + \mathbf{f}\cdot^T \tag{1.23}$$

CLF and reptation:

$$\frac{1}{3\pi^2\tau_e}\frac{a}{\sqrt{Tr\mathbf{f}(s_{\min},s_{\min})}}\left(\frac{\partial}{\partial s}+\frac{\partial}{\partial s'}\right)\left(\frac{aD_{CLF}(s,s')}{\sqrt{Tr\mathbf{f}(s_{\min},s_{\min})}}\left(\frac{\partial}{\partial s}+\frac{\partial}{\partial s'}\right)\mathbf{f}\right) \tag{1.24}$$

CR:

$$\frac{3va}{2}\left[\frac{\partial}{\partial s}\left(\frac{a}{\sqrt{Tr\mathbf{f}(s,s)}}\frac{\partial}{\partial s}(\mathbf{f}-\mathbf{f}^{eq})\right)+\frac{\partial}{\partial s'}\left(\frac{a}{\sqrt{Tr\mathbf{f}(s',s')}}\frac{\partial}{\partial s'}(\mathbf{f}-\mathbf{f}^{eq})\right)\right] \tag{1.25}$$

Retraction:

$$\frac{\mathscr{R}_s}{2\pi^2\tau_e}\left[\frac{\partial}{\partial s}\left(\mathbf{f}\frac{\partial}{\partial s}\ln[Tr\mathbf{f}(s,s)]\right)+\frac{\partial}{\partial s'}\left(\mathbf{f}\frac{\partial}{\partial s'}\ln[Tr\mathbf{f}(s',s')]\right)\right]. \tag{1.26}$$

With equilibrium configuration being:

$$\mathbf{f}^{eq}(s,s') = \begin{cases} \frac{1}{3}\mathbf{I} & for|s-s'|<1/2 \\ 0 & otherwise \end{cases} \tag{1.27}$$

Degree of entanglement being:

$$Z^*(t) = \frac{1}{a}\int_0^Z \sqrt{Tr\mathbf{f}(s,s)}ds \tag{1.28}$$

CLF diffusion being:

$$D_{CLF}(s,s') = \begin{cases} \frac{\alpha_d^2}{s_{\min}^2} & s_{\min} < \alpha_d\sqrt{Z} \\ 1/Z & otherwise \end{cases} \tag{1.29}$$

$$s_{\min} = \min(s,s)', Z-s, Z-s', \alpha_d = 1.15 \tag{1.30}$$

Constraint release rate being:

$$\nu = c_\nu\left(\lambda + \frac{1}{3\beta_{rcr}(Z,c_\nu)Z^*(t)Z^2\tau_e}\right) \tag{1.31}$$

Retraction rate being:

$$\lambda = -\frac{\mathscr{R}_s}{2aZ^*(t)\pi^2\tau_e}\int_0^Z \frac{1}{\sqrt{Tr\mathbf{f}(s,s)}}\frac{\partial}{\partial s}\left[Tr\mathbf{f}(s,s')\frac{\partial}{\partial s}\ln[Tr\mathbf{f}(s,s)]\right]_{s'=s} ds \tag{1.32}$$

Stress being:

$$= \frac{12G_e}{5Z}\int_0^Z \mathbf{f}(s,s)ds + \frac{G_e}{Z}\int_{-\inf}^t \sum_{p=Z}^N \exp\left(-\frac{2p^2(t-t')}{Z^2\tau_e}\right)[(t') + (t')^T]dt' \tag{1.33}$$

The GLaMM Model can reliably predict the stresses [41, 62, 70] and neutron scattering patterns [71–73] of monodisperse linear polymer melts under both strong and weak flows [74]. Also, apart from being able to compute the tube configuration and stress tensor for an arbitrary homogeneous non-linear deformation [75], the GLaMM Model has been shown to predict the start-up flow adequately [76]. On the other hand, a recent critique [77] of the model shows that even though it captures transient shear viscosity rather well, it fails completely for the case of elongational flow showing infinite viscosity, predicting strain hardening for high elongational rates and high strains, while experimental data shows a steady state.

1.2.7 Future Research in the Area of Polymer Rheology

Despite the great success in the area of polymer rheology, several open questions regarding the experimentally observed phenomena of arrested wall slip [78], metastable shear banding [79–81], yielding in start-up extensional flow [82], as well as quantification of tumbling, orientation and stretching transition [83–85] still require enhancements in the present or new theories to describe [63, 76].

CHAPTER 2

Synthesis and the Molecular Mass Determination

2.1 Synthetic Pathways to the Star and POM-POM Polymers

The introduction to the targeted types of macromolecules for this project was given in the review part of this thesis. This section will focus on the available synthetic approaches to the needed polymers namely with the star and double star (H-shaped, super-H-shaped/POM-POM) architectures since these types of molecular architecture prevent reptation relaxation mechanism after a strain.

According to Zhao [86], star polymers can be produced by:

- 'Core first' approach, employing the multifunctional core synthesis as the first step with further arm growth usually via vinyl monomer polymerization;
- 'Arm first' approach, when a living or functionalized linear polymer is produced first with further linking reactions;
- 'In-out' approach, when succesive arms are grown from multiple initiating sites in a core via different polymerization techniques.

Polymer arms in the 'arm first' approach can be made using ATRP [87–90], NMP [91, 92], RAFT [93–96] and ROP [97] polymerization techniques [86], and assembled into a star with the help of specific coupling agents, click-reactions [98–100], hydrosylilation [87, 101, 102], napthalene chemistry [103] and ruthenium (III) complexes [104], but this section will focus solely on the star polymer synthesis made by the means of the living anionic polymerization technique.

The use of anionic polymerization (for the mentioned synthetic pathways) is governed mainly by high reactivities of the living anionic species, ability to produce high molecular weight polymers and low polydispersity of the starting building blocks for the stars — linear arms. The arm can be coupled to the final stars employing homopolymerizable, non-homopolymerizable or multifunctional linking agents, such as divynilbenzene (DVB), *para*-double diphenylethylene (PDDPE) or tetrachlorosilane respectively. Each method has its benefits and implications which will be discussed in the corresponding subsection below.

2.1.1 Divynilbenzene

The first star polymer synthesis employing DVB was done by Decker [105]. Since this method does not allow to precisely control the amount of arms due to the similar reactivity of the two vinyl groups, the product in their case was a mixture of polystyrene stars with the range of arms from 6 to 15. The remaining drawbacks of the method include the fact that there is a

chance of network/loop formation in case of intra-/intermolecular reactions of the polyfunctional living species and the fact that the number of arms depends on the molecular weight of the linear block and the molar ratio of the coupling agent to the living species. All these implications limit the amount of possible polymer architectures to the range of those that are not suitable for the purposes of this research.

2.1.2 PDDPE

Despite the fact that PDDPE (1,4-bis(1-phenylethenyl)benzene) also has two double bonds as DVB, the phenylethylene double bonds cannot undergo polymerization due to steric hindrance, allowing to couple linear chains to produce a macroinitiator which is capable of continued addition of monomer offering a way for both symmetric and non-symmetric stars. It was found by Yamagishi [106] that the rate constants of the addition reactions to the two reactive sites differ in a factor of 13. This feature also allows to produce so-called μ-star polymers, where different arms in a star are made of different monomers. Not only the rate constants of the addition reactions, but also the two rate constants of initiation differ, possibly giving a bimodal distribution of polymers, so it should be noted that often certain polar compounds are used to alter the reactivity of those two sites, which have to be taken into account in case of certain polymer syntheses (for example, in case of polydienes).

2.1.3 Chlorosilanes

The first successful attempt to synthesize star polymers employing chlorosilanes was made in 1962 [107]. In this research Morton used tetrachlorosilane as the linking agent to produce a mixture of 3- and 4-arm polystyrene stars. The inability to convert all the 3-arm stars to 4-arm ones even with a large excess of living anions is attributed to the steric hindrance at the silicon atom and decrease in reactivity with the increase of molecular weight of polymers. In more detail, this issue is described in Appendix A. Since then, a number of papers has been published describing the star synthesis with the use of other chlorosilanes, such as 1,2-Bis(trichlorosilyl)ethane [108], Hexadecachlorosilane [109] and Tetrahexicontachlorosilane [110].

2.1.4 Chloro- and Bromomethylbenzene Derivatives

Chloro- and Bromomethylbenzene derivatives are now used as the star coupling agents mostly for living anions of polar nature [111], but the first star synthesis employing Tri(chloromethyl)-benzene was made to produce 3-arm polystyrene stars [112]. The method is well suited for block copolymers, as has been shown by Mayer [113] for the case of *block*-PI-*block*-PS and *block*-PS-*block*-PI-*block*-PS 4-arm stars with the use of 1,2,4,5-Tetra-(chloromethyl)benzene, however has a shortcoming expressed in the lithium-halogen exchange side reaction that can be suppressed in case of anionic polymerization done in polar solvents at -78°C with potassium counter ions [111].

2.1.5 Other Coupling Agents

It has been documented that star polymers can be made employing such terminators as Hexachlorocyclotriphosphazene [114, 115], 2,4,6-Triallyloxy-1,3,5-triazine [116], 1,1,4,4-tetraphenyl--1,4-bis(diallyloxytriazine)butane [117], tin tetrachloride [118], and phosphorus trichloride [119].

Although the typical shortcoming of these coupling agents is deemed to be the inability to extent star functionality behind six arms, those synthetic approaches has not been considered by our group since there is no data on star core stability of such polymers at elevated temperatures to the best of our knowledge.

2.1.6 Iterative Methodology Coupling Agents

Iterative methodology concept that was developed by the Hirao group, aims to overcome the typical drawback of star synthesis procedures allowing to produce polymers pushing the limit of arms to unknown. The methodology offers two consecutive synthetic steps: the first being arm introduction, when a two-functional coupling agent is added to living anions and the second — the reintroduction of the same reaction site. In such a manner arms of different chemical nature can be introduced to a polymer and this subsequence can be repeated with no predicted limit [120]. The methodology offers two synthetic designs. The first employs diphenylethylene and 1,3-butadiene reactive sites to be reintroduced with a halogen being the other functionality. This approach allows star polymer synthesis of a highly reactive anionic species, such as PS, PB and P2VP since they are reactive enough to react with DPE and/or 1,3-butadiene sites. The typical coupling agents for DPE-based synthetic approaches are:

- 1-(4-(3-Bromopropyl)phenyl)-1-phenylethylene (DPEBr3) [121];
- 1,3-Bis(1-phenylethenyl)benzene [122];
- 1,1-Bis(3-(1-phenylethenyl)phenyl)ethylene [123];
- 3,5-Bis(3-(4-(1-phenylethenyl)phenyl)propoxy)benzyl bromide [124].

6-Bromo-3-methylene-1-hexene [125, 126] — the linking agent introducing 1,3-butadienyl reactive site can be used when the forthcoming oxidation or Diels-Alder reactions are followed to transform the functional group into an epoxide or acid anhydride functions.

The second generation of iterative methodology coupling agents consists of compounds bearing such groups as:

- α-Phenylacrylate [127, 128];
- 2-Tetrahydropyranyl ether [129];
- 1,3-Dioxolane [130].

that are reintroduced upon Trimethylsilyl and tert-Butyldimethylsilyl ether hydroxyl protection cleavage, that makes a new reaction site, giving a possibility to use most of the polymers (PS, PB, PI, P2VP, PRMA etc.) within this synthetic star polymer concept.

Finally, this methodology also offers the ability to combine star polymer synthesis by the means of anionic polymerization with other polymer synthesis methods, like ‘click’ reactions, employing, for example, star polymers with aminogroups in the core [131].

2.2 Preparation to Syntheses

2.2.1 Glassware

Before syntheses, all the glassware was cleaned in an iPrOH/KOH ‘base-bath’ and washed with $1N$ HCl to protonate any possible potassium silanolates, that could favor 1,2-addition of butadiene during the polymerization in cyclohexane. Henceforth, the glassware was ‘baked’ in

an oven at the temperature of approximately 570°C for two hours in order to remove tensions in the glass preventing a breakage under an increased pressure environment and with the aim of condensing all surface silanols that are acidic enough to terminate the living anionic polymerization. Subsequently, the glassware was allowed to slowly cool down, assembled and 'baked' at 250°C and 10^{-2} $m$bar vacuum overnight so that traces of water are removed from the reactor.

2.2.2 Solvent Preparation

Cyclohexane (Aldrich, 99%) or benzene (Aldrich, 99.8%) were refluxed under argon atmosphere (Aga, 99.9999%, ISO 14175-I1-Ar) with oligostyryllithium, made of *sec*-butyllithium (Aldrich, 1.4M solution in hexanes, 1 ml per liter of cyclohexane) and styrene (Aldrich, 99%, stabilized with 4-*tert*-butylcatechol, 5 ml per liter of cyclohexane).

THF (Aldrich, 99.9%, inhibitor-free) was refluxed under argon atmosphere with sodium (oxidodiphenylmethyl)sodium made of an excess of sodium (Aldrich, 98%) and benzophenone (Aldrich, 99%).

After the preparations, the solvents were distilled directly into reactors.

2.2.3 Monomers Preparation

Styrene and styrene-d8 (Cambridge Isotope Laboratories, 98%, stabilized with 4-tert-butylcatechol) were filtrated through a column with aluminum oxide (to remove the stabilizer and water) to a flask with calcium hydride, degassed and distilled to a vacuum-dried di-n-butylmagnesium (Aldrich, 1M solution in heptane). Afterwards, the monomers were distilled into ampoules.

Butadiene (Aldrich, 99.6%, stabilized with 4-tert-butylcatechol) was transferred to a liquid nitrogen cooled flask with a vacuum-dried Bu_2Mg and degassed. The flask was left overnight at -18°C. Afterwards, the monomer was distilled into an ampoule.

2.2.4 Initiator Preparation

sec-BuLi was purchased from Aldrich (1.4M solution in hexanes). Its concentration was determined according to the Gilman double titration method [132], obtaining the value of active *sec*-BuLi by subtracting the amount of degraded *sec*-BuLi (determined by titrating bases after neutralizing the active *sec*-BuLi with 1,2-dibromoethane) from the amount of overall bases (determined by titrating the water-quenched solution of the initiator).

A handful of alternative titration methods have been also tested with the aim of replacing Gilman double titration protocol that employs carcinogenic 1,2-dibromoethane with no particular success: 1,3-diphenyl-2-propanone tosylhydrazone in THF did not give sharp color change at the equivalence point assigned to the tosylhydrazone dianion formation [133], whereas the titration [134, 135] with 2,2'-biquinoline indicator did not give reproducible results.

Naphtalenides of alcali metals were prepared according to the standard procedure [136].

2.3 Linear Polymers Synthesis

The narrow molecular weight polystyrenes were synthesized using the method of living anionic polymerization according to the standard procedure [137]. Reactions were carried out for 4-5 hours at 30-35°C in cyclohexane. Living anions were neutralized with degassed methanol. After this step, the reaction mixtures were precipitated into methanol. Polymers were collected and dried in vacuum at 50°C for 24 hours.

2.4 Star (co)Polymers Syntheses

2.4.1 Three-Arm Star Polystyrene with a Silicon Core

Reactions were carried out in freshly distilled THF. The synthesis consisted of two stages: first, linear polymer growth at -78°C was carried out for 30 minutes; second, the star formation stage at the same temperature with methyltrichlorosilane as the coupling agent took from 4 to 20 hours, depending on the molecular weight of the linear species. The 1.3 molar excess of living anions (used to avoid the doubling of the molecular weight of the linear polymer) was neutralized with degassed MeOH. The resulting polymer solution was fractionated, precipitated, collected and dried in vacuum at 50°C for 24 hours.

2.4.2 Three-Arm Star Polystyrene with a Carbon Core

The synthesis was done the same way as in Sec. 2.4.1, but with the use of 1,3,5-tris(bromomethyl)benzene as the coupling agent and took 8-30 hours for coupling because of the lower reactivity of the bromomethylbenzene species.

2.4.3 Three-Arm Star *block*-PSH-*block*-PSD Star Polymers with the Silicon Core

Reactions were carried out in THF. The synthesis consisted of three stages:
first, linear polystyrene-*d8* block growth was started at -108°C with the use of a melting THF bath, giving a narrow polidispersity for the case of low molecular weight blocks in THF (PDI of 2.08 at -78°C and PDI of 1.09-1.16 at -108°C, as shown in Tables 2.1, 2.4).

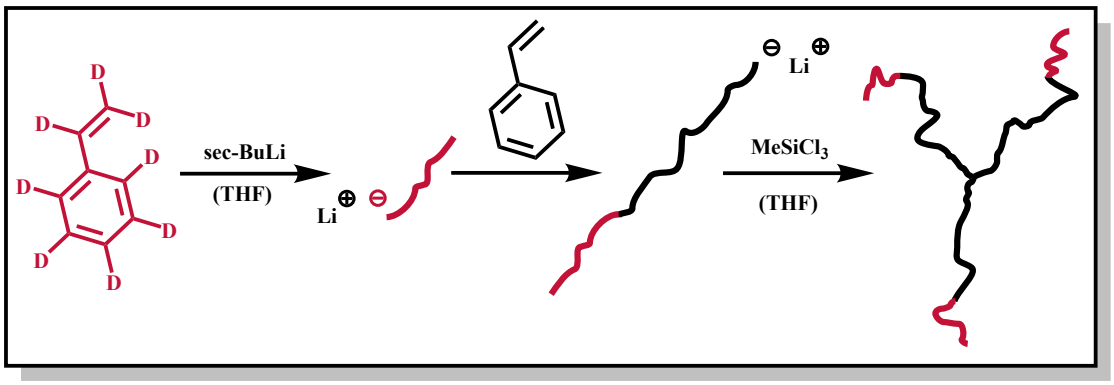

Figure 2.1: Synthetic route to the block-copolymer stars.

The stage took 20 minutes. The second stage started at -108°C and the reaction mixture was allowed to slowly warm up to -78°C upon the addition of the second monomer. The stage took 30 minutes. The final stage and polymer handling were identical to the ones described in Sec. 2.4.1.

2.4.4 Three-Arm Star *block*-PSH-*block*-Oligobutadiene Star Polymers with the Silicon Core

Reactions were carried out in cyclohexane. The synthesis consisted of two stages: first, linear polymer growth, was done according to the procedure, described in Sec. 2.3. The star formation stage at 35°C with methyltrichlorosilane as the coupling agent took 6 hours. The 1.3 molar excess of living anions was neutralized with a degassed 10% solution of AcOH in iPrOH. AcOH was used as the terminator instead of MeOH to avoid formation of lithium methanolate that could favour pentacoordinate silicon compounds obtainment through the alkoxide donation to the organosilane and the silicon-carbon bond cleavage reactions [138]. The resulting polymer solution was precipitated into 1% methanol solution of butylated hydroxytoluene (BHT), fractionated with the use of 1% solutions of BHT both in solvent and nonsolvent, precipitated again, collected and dried in vacuum at 50°C for 24 hours.

2.5 Fractionation

The process of collecting of the precipitated phases in succession gives the ability to fully separate significant amount of polymers of different molecular masses. Employing this technique, the fractionations were done using either toluene or THF or cyclohexane as solvents and n-heptane, n-hexane, methanol and isopropanol as the non-solvents, except for the polymers with oligobutadiene blocks, where THF was not used. The mentioned fractionations were done from 0.25-1% polymer solutions: a sample was dissolved in a solvent and, upon stirring, the amount of non-solvent was added until the turbidity of the solution. Then the solution was heated in order to dissolve the precipitates and left to slowly cool down in a separation funnel giving the separated phases, which were collected. The size-exclusion chromatograms of consecutive steps of fractionation are shown in Fig. 2.2. The peak in the high molecular weight region (less retented at a size-exclusion column) is assigned to a star polymer, while the second peak is coming from the excess of linear chains, used for the coupling reaction. The different width of the normalized overlayed peaks may originate from different concentrations of used samples, whereas the peak position distribution is, within the experimental error, coming from the flow instabilities.

2.6 Size Exclusion Chromatography

The size exclusion chromatography (SEC) method excludes polymer molecules utilizing the partition equilibrium of polymer chains between common solvent phases located at the interstitial space and the pores of the column packing materials, typically in the form of uniformly sized porous beads. The stationary and mobile phases are chosen to minimize the enthalpic interaction of the polymeric solutes such that the partition equilibrium is mainly governed by the conformational entropy difference of the polymer chains in the two phases. SEC separates the polymer molecules according to the size of a macromolecule in the elution solvent. If a simple relationship exists between the chain size and the molecular weight of polymers

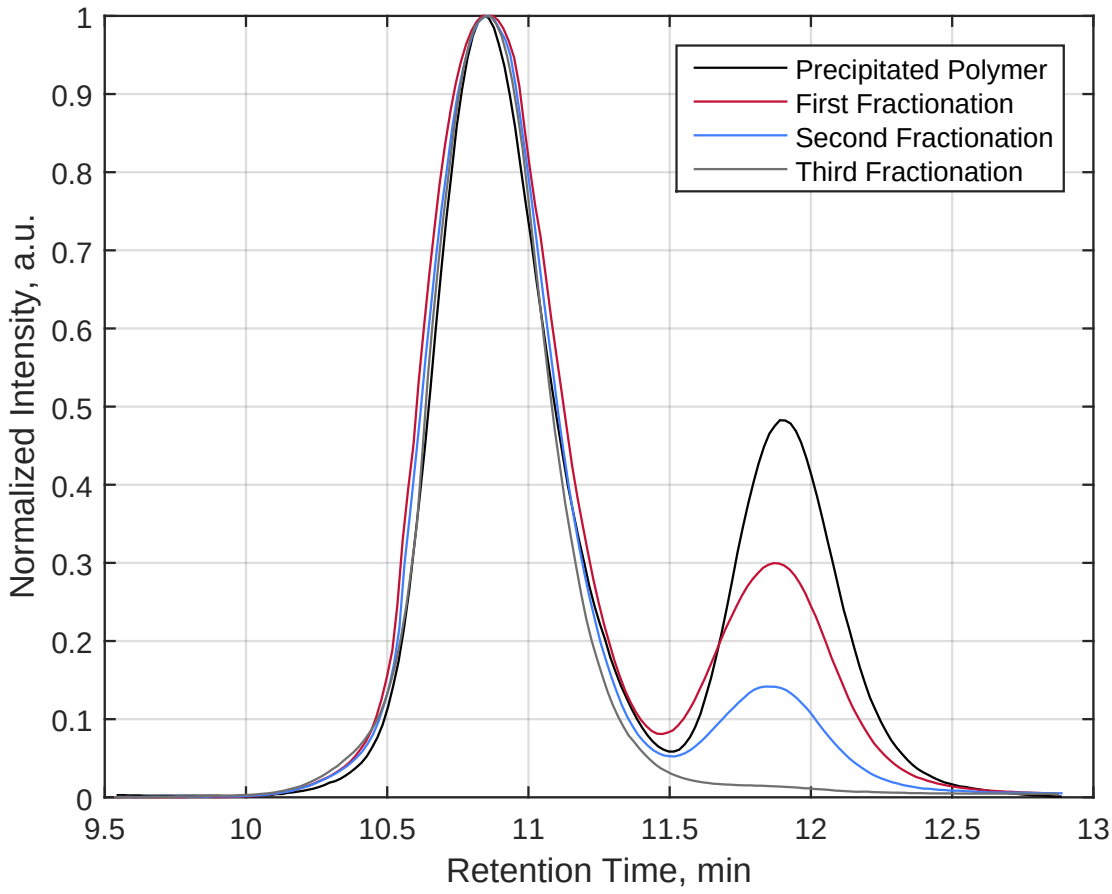

Figure 2.2: Size-Exclusion Chromatograms of a Star Polymer at Different Fractionation Stages.

such as for linear and chemically homogeneous polymers, SEC retention is well correlated with the molecular weight [139].
The molar masses of the polystyrene samples were determined with the help of SEC with non-stabilized THF as the eluent and with the use of a column set consisting of a 5μm guard column and two 300 × 8 mm^2 columns (PLgel Mixed C and Mixed D). The system was equipped with a triple detector system (a combined Viscotek model 200 differential refractive index (DRI) and a differential viscosity detector plus a Viscotek model LD 600 right angle laser light scattering detector (RALLS)).
Columns were calibrated with a number of narrow molar mass distribution linear polystyrene standards. On the basis of calibration and flow rate signal adjusting according to either Irganox 1010 or Irganox 1330 or BHT signals, the values of M_w and M_w/M_n (PDI) were determined.
The application of this calibration to branched macromolecules may underestimate the molar mass to some extent, depending on the present molecular architecture. To check the molar mass of the branched polymers, a method that is independent on the measured retention time, but employs both the DRI and RALLS signals was used:

$$DRI = k_1 c \frac{\partial n}{\partial c} \tag{2.1}$$

$$RALLS = k_2 c M \left(\frac{\partial n}{\partial c}\right)^2 \tag{2.2}$$

In the Eq. (2.1) and (2.2), k_1 and k_2 are the proportionality constants, c corresponds to the mass concentration, and $\partial n/\partial c$ is the refractive index increment.

These equations may serve for obtaining the expression for the molecular mass:

$$M_w = \frac{RALLS(k_1/k_2)}{DRI(\partial n/\partial c)} \tag{2.3}$$

The relation (2.3) was used to compute the molecular mass knowing the two signals and instrumental constants. Since the relation is independent on the molecular architecture, the quantity for $(k_1/k_2)/(\partial n/\partial c)$ is determined from the SEC signals of a narrow linear polystyrene standard. Thus, weight average molecular weight of a polymer is obtained regardless of the column calibration [140–144].

2.7 Matrix-Assisted Laser Desorption/Ionization Time-of-Flight Mass Spectroscopy

The molecular weight of polymers in some cases was additionally checked by the means of MALDI ToF MS.

MALDI ToF MS is a known powerful technique able to provide the molar mass, composition, and functionality of polymers. The molar mass distribution data of narrowly distributed polymers may be provided with good accuracy up to molar mass values of about 200 kg/mol [144]. The spectra were recorded according to the standard interlaboratory protocol for polystyrene samples using a Bruker Autoflex Speed instrument with a UV laser source at 337 nm in linear mode.

External mass calibration was performed with the use of a standard peptide mixture (insulin, thioredoxin) or porphyrin derivatives. The procedure of sample preparation involves dissolution of a compound, matrix and silver trifluoroacetate (added to enhance ionization by cation attachment) in solvents with known concentrations.

In short, 5 μl of a 3 mg/ml polymer solution in THF was mixed with 10 μl of 0.1M dithranol matrix in THF and 1 μl of 0.02M AgTFA solution in toluene. The mixture was put on the Anchor chip samples holder, air-dried at ambient temperature and transferred to the instrument. Samples were ionized with 60-90% laser power and the final spectra were averaged out of 1000-2000 scans.

2.8 Polymer Samples

2.8.1 Linear Samples

The table in this subsection shows the list of linear polystyrenes initiated by sec-BuLi. The time of the syntheses is given in hours or an approximate estimate ‘overnight’ is written.

#	M_w, kg/mol	PDI	Solvent	T,°C	Time
1	7.8	2.08	THF	-78	0.25
2	138.5	1.68	THF	-78	0.5
3	2.3	1.09	Cyclohexane	35	4
4	1.5	1.09	Cyclohexane	35	72
5	95	1.05	Cyclohexane	30	4
6	156.5	1.06	Cyclohexane	35	4
7	916.3	1.18	Cyclohexane	35	4
8	171.8	1.09	Cyclohexane	35	4
9	84.2	1.06	Cyclohexane	35	overnight

Table 2.1: Linear PS Samples.

2.8.2 POM-POM Samples

Two unsuccessful synthetic routes to POM-POM polymers were tested. The idea behind one route was to create a living dianion and terminate it with an excess of 1,3,5-Tris(bromomethyl)-benzene (3BnBr), fractionate from the terminator, and attach another linear living monoanions at the methylenebromide sites.

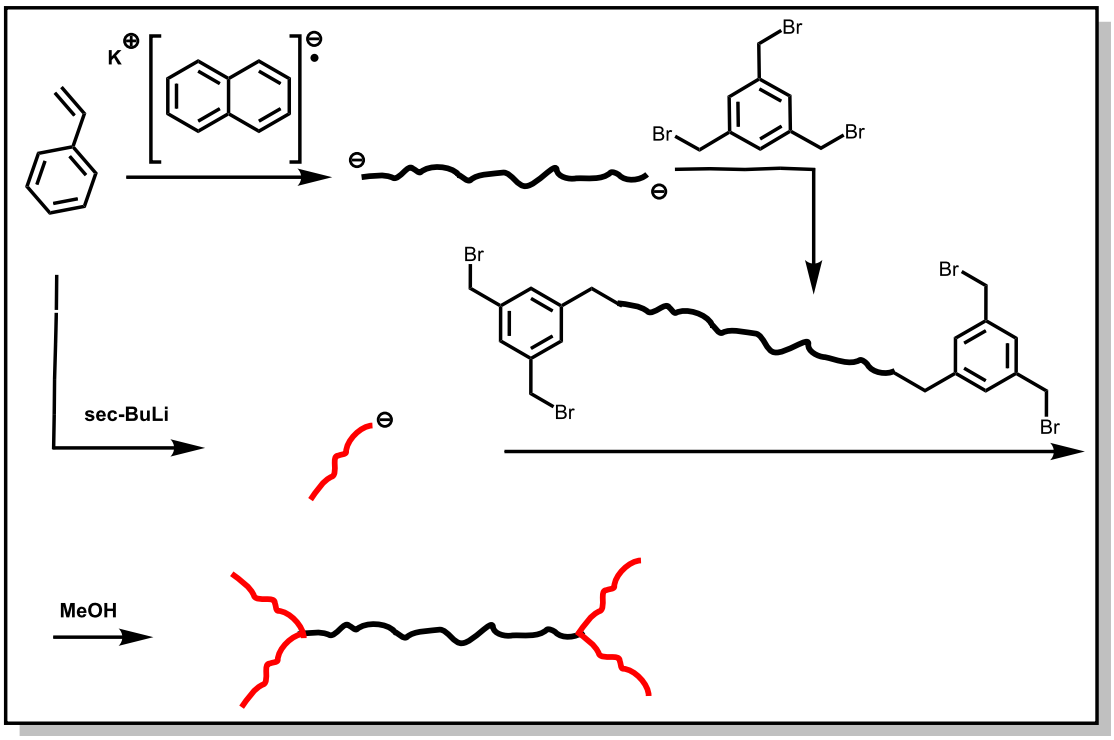

Figure 2.3: The reaction scheme describing the unsuccesfull POM-POM polymer synthesis with the use of the excess of 3BnBr terminator.

This was impossible at the conditions we were using since at those conditions some fractions of molecular weight doubling occurred. The reaction scheme for this route is shown in Fig. 2.3. Another approach was to use the specifically synthesized terminators, 1,3-bis-(1-phenylvinyl)benzene (DPEBr) and 1-(4-(3-Bromopropyl)phenyl)-1-phenylethylene (DPEBr3), synthesized according to the method suggested by the Hirao group [124]. The use of these terminators to living anions in the molar ratio 3:4 would allow to create a linear polymer with a reactive double bond in the middle of the molecule. The next hypothetical step would be to attack this double bond by living dianions, producing a POM-POM polymer. This synthetic route was not succesful because it was impossible to fully separate the terminator from its predecessor, the corresponding ketone and its low reactivity. The terminator synthesis is shown in Fig. 2.4 and the reaction scheme is shown in Fig. 2.5.

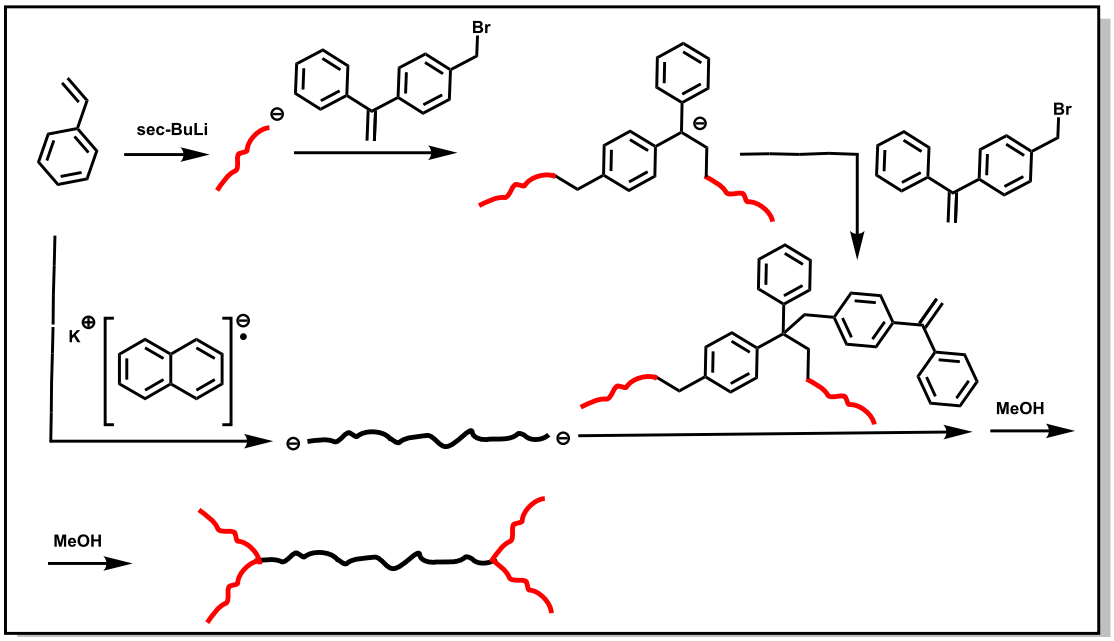

Figure 2.5: The reaction scheme describing the unsuccesfull POM-POM polymer synthesis with the use of the DPEBr1 terminator.

In the table below, 'RT' stands for room temperature, 'lin.' — linear, 'lpp.' — linear part of a POM-POM, i.e. POM-POM without arm, 'UCD' — until the living anion color disappearance, 'MNapht' — naphtalenide of an alkali metal, 'CH' — cyclohexane and 'PhH' — benzene.

The reactions were initiated by sec-BuLi until something else is written in square brackets in 'Comments' section of the table.

2.8.3 Star Samples

All the linear polymers for the star samples were initiated by sec-BuLi.

The coupling agent was 1,3,5-Tris(bromomethyl)benzene (3BnBr), except for the sample #14, which was coupled with $MeSiCl_3$. '#fr.' stands for the number of fractionations made to exclude the needed polymer.

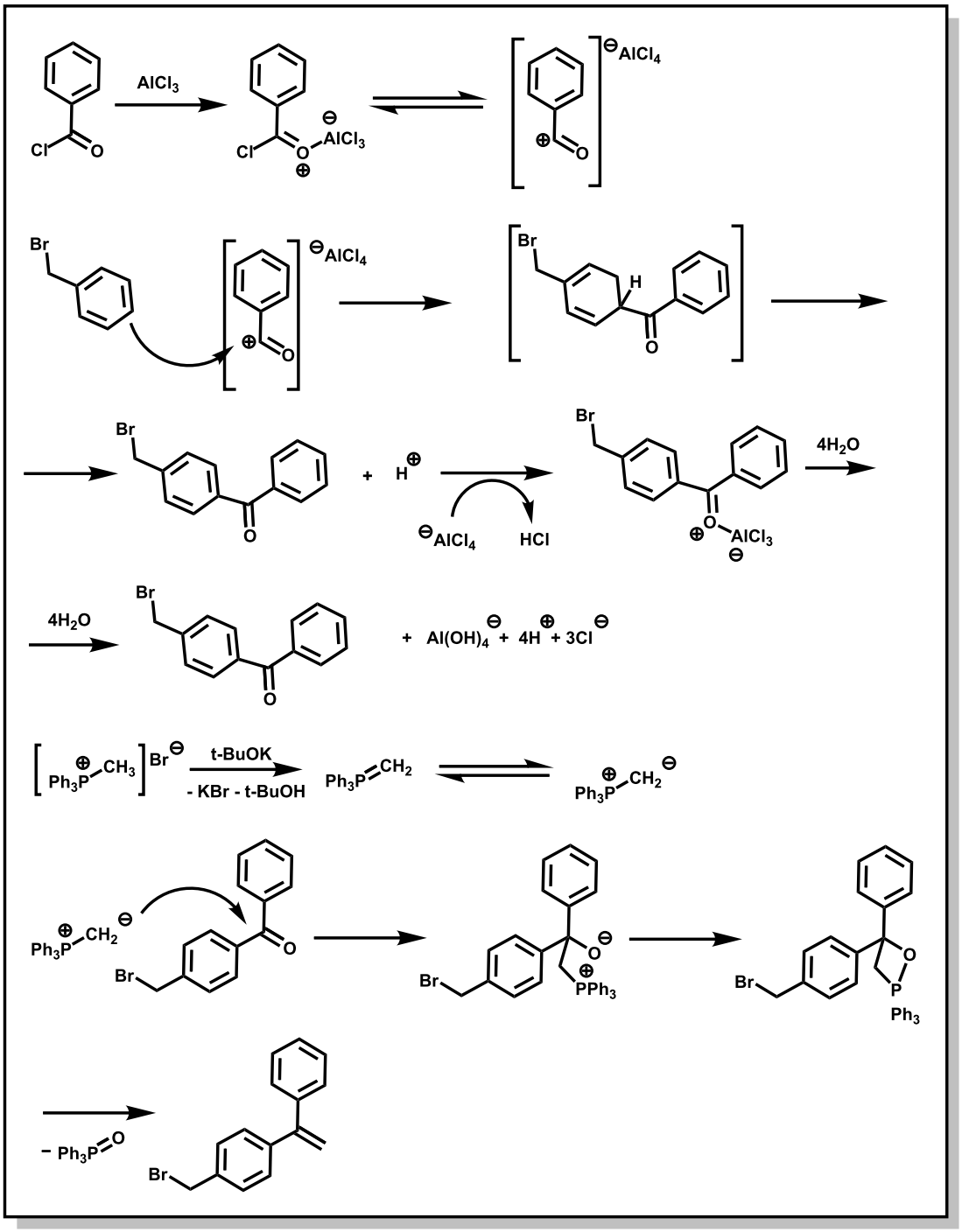

Figure 2.4: The reaction scheme describing the synthesis of the DPEBr1 terminator.

#	Arch.	M_w	PDI	Solv.	T,°C	Time	Comments
1	lin.	1757.0	1.70	CH	35	4	[KNapht], Unexpectedly long PS
2	lin.	124.8	1.87	CH	35	4	[KNapht], broad PD
3	lin.	70.4	1.62	THF	-78	0.5	[NaNapht], broad PD
4	lin.	146.2	1.22	THF	-78	0.5	[KNapht]
	lpp.	438.2	2.36	THF	-78	UCD	Unexpected coupling
5	lin.	53.6	1.61	THF	-78	0.5	[KNapht]
	lpp.	72.0	2.11	THF	-78	UCD	Unexpected coupling
6	lin.	107.8	1.30	PhH	RT	2	[LiNapht]
	lpp.	733.6	4.24	PhH	RT	UCD	Unexpected coupling
7	lin.	63.9	1.33	THF	-78	0.5	[KNapht]
	lpp.	214.7	2.36	THF	-78	UCD	Living anion added dropwise
8	lin.	35.2	1.07	THF	-78	0.5	Terminated with DPEBr
	lpp.	42.6	1.19	THF	-78	UCD	Impossible to fractionate
9	lin.	174.3	1.13	THF	-78	0.5	Terminated with DPEBr3
	lpp.	307.0	1.29	THF	-78	UCD	Impossible to fractionate

Table 2.2: List of polymers obtained according to unsuccessful strategies.

#	Arch.	M_w	PDI	Solv.	T,°C	Time	#fr.	Comments
1	lin.	37.6	1.08	CH	35	4		
	star	72.1	1.37	CH	35	overnight		Incomplete coupling
2	lin.	1085.0	2.11	CH	35	6		Unexpectedly long PS
	star	1206.0	2.01	CH	35	overnight		
3	lin.	144.6	1.11	CH	35	4		
	star	211.1	1.49	CH	35	overnight		Incomplete coupling
4	lin.	30.7	1.13	THF	-78	1		
	star	57.4	1.34	THF	-78	4		Incomplete coupling
5	lin.	28.7	1.23	THF	-108	0.5		
	star	64.9	1.14	THF	-78	6		Incomplete coupling
6	lin.	64.8	1.90	THF	-78	0.5		
	star	105.3	1.77	THF	-78	overnight		Solution became too viscous
7	lin.	74.2	2.39	THF	-78	0.5		Broad PD
8	lin.	53.1	2.10	THF	-78	0.5		Broad PD
9	lin.	33.6	1.20	THF	-78	0.5		
	star	88.2	2.60	THF	-78	overnight		Broad PD
10	lin.	9	1.10	THF	-108	0.5		
	star	26.5	1.10	THF	-78	overnight	7	
11	lin.	70.3	1.52	THF	-78	0.5		
	star	171.1	1.32	THF	-78	overnight	2	
12	lin.	34.5	1.17	THF	-78	1		
	star	91.9	1.10	THF	-78	overnight	4	
13	lin.	38.1	1.14	THF	-78	1		
	star	100.8	1.09	THF	-78	overnight	4	
14	lin.	34.8	1.03	THF	-78	0.5		
	star	88.2	1.05	THF	-78	overnight	3	Coupled with $MeSiCl_3$

Table 2.3: Star polymer samples.

2.8.4 Deuterated Star Samples

All polymerization were initiated by sec-BuLi. $MeSiCl_3$ as the coupling agent was used.

'linDH' stands for linear copolymer made of randomly distributed deuterated and protonated styrenes, 'linD' — linear deuterated polystyrene block, 'linH' — linear protonated polystyrene block, 'linDlinH' — linear living copolymer made of consecutive linear blocks of deuterated and protonated polystyrenes used for the star-coupling reaction.

#	Arch.	M_w	PDI	Solv.	T,°C	Time	#fr.	Comments
1	linDH	95.8	1.20	THF	-78	0.5		
	star	389.5	1.80	THF	-78	overnight		Broad PD
2	linDH	98.8	1.06	THF	-78	0.5		
	star	290.4	1.09	THF	-78	20	3	
3	linDH	99.7	1.04	THF	-78	0.5		
	star	303.0	1.07	THF	-78	20	8	
4	linD	10.0	1.40	THF	-78	0.25		Broad PD
5	linD	10.0	1.12	THF	-108	0.25		
	linDlinH	268.1	1.70	THF	-108	0.5		Broad PD
6	linD	5.9	1.05	THF	-108	0.25		
	linDlinH	86.1	1.80	THF	-108	0.5		Broad PD
7	linD	4.4	1.09	THF	-108	0.25		
	linDlinH	108.1	1.14	THF	-108	0.5		
	star	236.9	1.18	THF	-78	6	2	Incomplete coupling
8	linD	6.2	1.16	THF	-108	0.25		
	linDlinH	116.7	1.60	THF	-108	0.5		Broad PD
	star	282.8	1.80	THF	-78	6		Incomplete coupling
9	linD	7.8	1.14	THF	-108	0.25		
	linDlinH	101.7	1.40	THF	-108	0.5		
	star	309.1	1.30	THF	-78	20		Broad PD

Table 2.4: PSD-PSH Star Samples.

2.8.5 *block*-PSH-*block*-Oligobutadiene Star Samples

All the polymerization were initiated by sec-BuLi and $MeSiCl_3$ was used as the coupling agent.

'linPS' — linear protonated polystyrene block, 'linPSlinPB' — linear living copolymer made of consecutive linear blocks of protonated polystyrene and polybutadiene used for the star-coupling reaction

#	Arch.	M_w	PDI	Solv.	T,°C	Time	#fr.	Comments
1	linPS	49.2	1.07	CH	35	4		Degraded
	linPSlinPB	53.8	1.09	CH	35	0.5		during
	star	130.0	1.30	CH	35	4	6	fractionation
2	linPS	45.8	1.03	CH	35	4		
	linPSlinPB	46.0	1.03	CH	35	0.5		
	star	135.8	1.03	CH	35	6	2	

Table 2.5: PS-PB Star Samples.

2.8.6 Comparison of SEC and MALDI ToF MS data

SEC was the main method to estimate the M_w and M_w/M_n of the synthesized polymers since MALDI ToF MS underestimates the high-mass components of the polymer distribution which results in lower average molecular weight values [145, 146]. MALDI ToF MS was used to cross-check the results of SEC, especially for the case of star polymers. The crucial information, that was taken from the absolute quantitative technique of MALDI ToF MS data is the molecular weight of the highest peak, which, for the case of star polymer sample #10, is equal to 27.1 kg/mol, as shown in Fig. 2.8. This information was later used to control the data from SEC, which is a relative technique and is dependent on column calibration and is known to have uncertainties in case of branched polymers, as was mentioned before. The final chromatogram for the star sample #10, which is shown in Fig. 2.7, gives M_w of 26.5 kg/mol for the sample, which is comparable to the result, obtained by MALDI ToF MS.

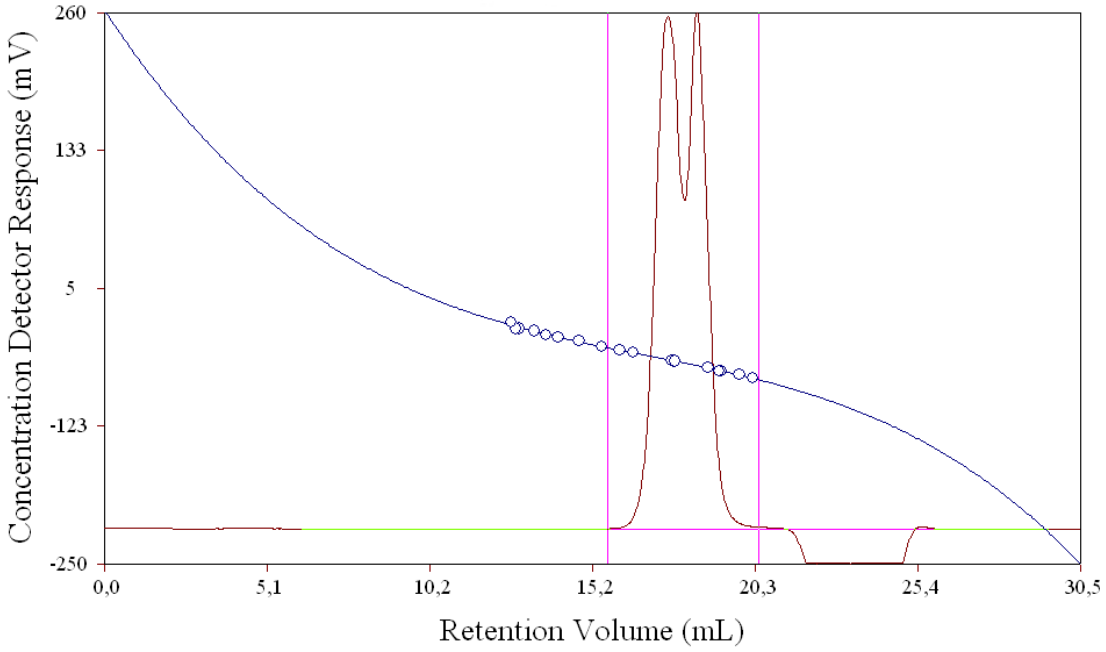

Figure 2.6: SEC chromatogram of the star polymer sample after the coupling reaction. Left peak represents the 3-arm star polymer, while the peak to the right is an excess of linear arm.

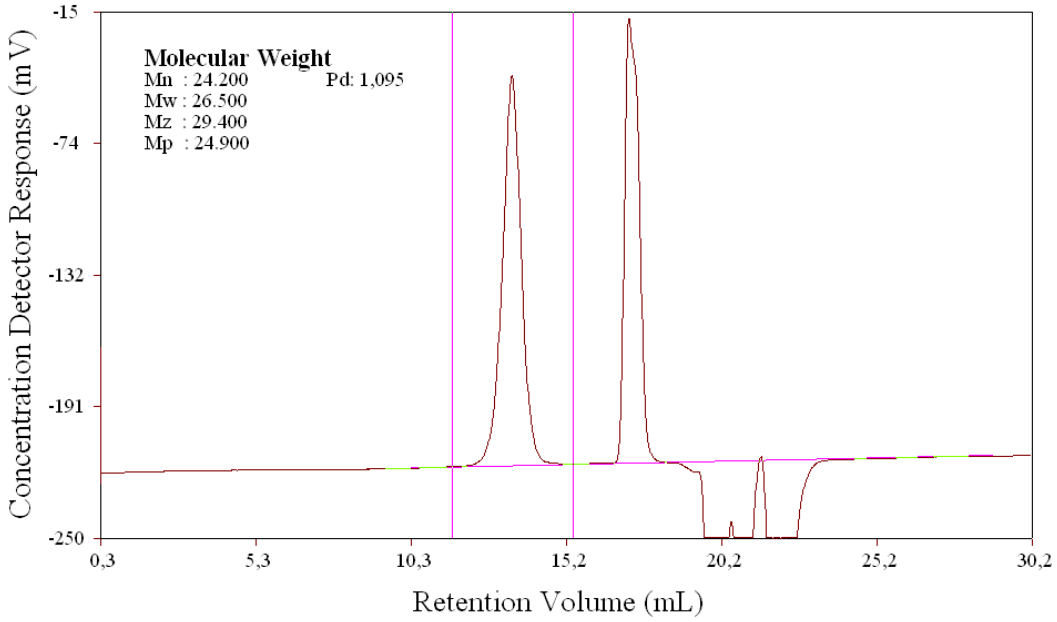

Figure 2.7: SEC chromatogram of the star polymer after 7 fractionation steps. The peak to the right — Irganox 1330 standard. The shape of the standard peak is due to a high concentration of Irganox which resulted in so-called 'column overload'.

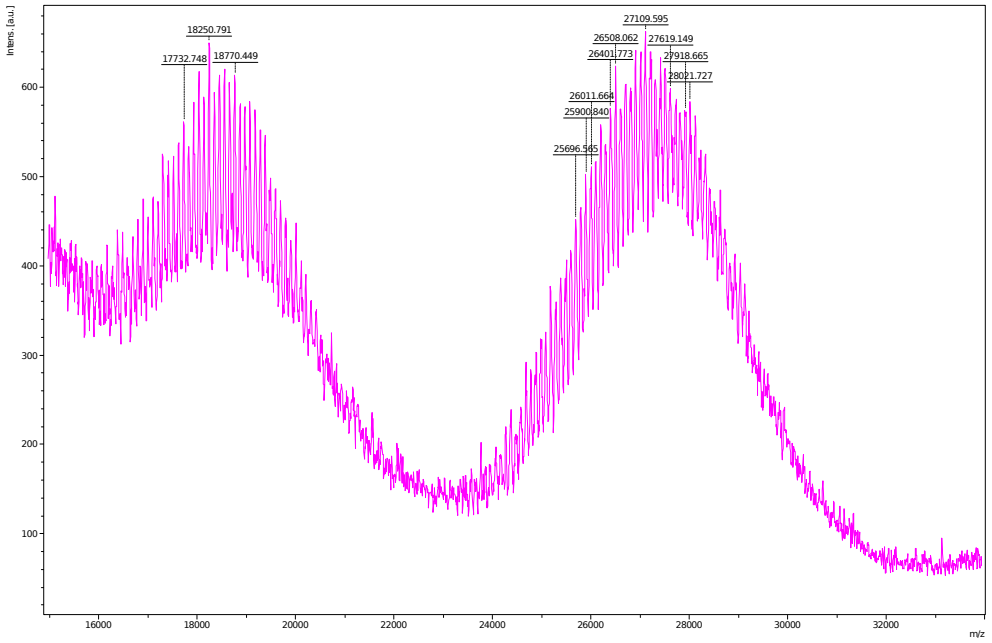

Figure 2.8: MALDI ToF Mass Spectrum of the star polymer sample after 2 fractionation steps.

CHAPTER 3

Filament Stretching Rheometer

For the purpose of experimental realization of uniaxial extension such types of extensional rheometers as Münsted tensile rheometer [147], the Meissner elongational rheometer [148], the filament stretching rheometer (FSR) [149] and the Sentmanat extensional rheometer [150] are employed [151]. Rheometers except for FSR utilize integral methods, applying uniform deformations with the use of prescribed mechanical motion related to a known strain [151]. In FSR, which measures stress during uniaxial extension, the rheological properties of a liquid between two plates are determined by pulling apart the top plate and measuring the force by a load cell at the bottom plate. The ideal uniaxial extension is recorded when a constant strain rate is directed towards the middle part of a filament [152, 153], with an active control loop system that defines the top plate motion depending on the middle diameter of the filament [151].

3.1 Principle of the Instrument

The FSR is composed of a bottom plate with a compression/tension load cell (Futek lrf400: 4.5 N capacity, 0.05% error on the maximum capacity, placed outside the thermostated environment) which is stationary and a mobile upper plate, which movement is generated by a step motor (Stebon FD8L604 with a Parker OEM650 step drive and an AT6200 controller). A sample is placed between the two plates and then covered with a thermostated oven. The heat in the oven is produced by eight heat elements and the temperature is regulated with the aid of six temperature sensitive pickers. Nitrogen that ensures an inert atmosphere during experiments is preheated at the bottom of the oven and flows into the chamber nullifying temperature gradients and good heat conduction in the oven. There are two slits at both sides of the oven which are covered with glass which is penetratable by Keyence LS7500 laser while measuring the diameter of a filament during a stretching experiment. The laser micrometer is placed in the middle between the two plates and motioned at the half of the speed of the upper plate, recording the middle filament diameter during the uniaxial extension. The laser is also capable of recording video images of the filament, giving a possibility to check the initial shape of a filament and possible sample neckings. The diameter is determined within a ± 10 μm error with a lower limit of 0.3 mm. The FSR is able to produce the possible Hencky strain of max. $\approx$6.8 [151, 155].

Figure 3.1: FSR (left) in a position when a sample is covered by the oven and the part inside the oven (right) with a sample (light red) between the two plates [154].

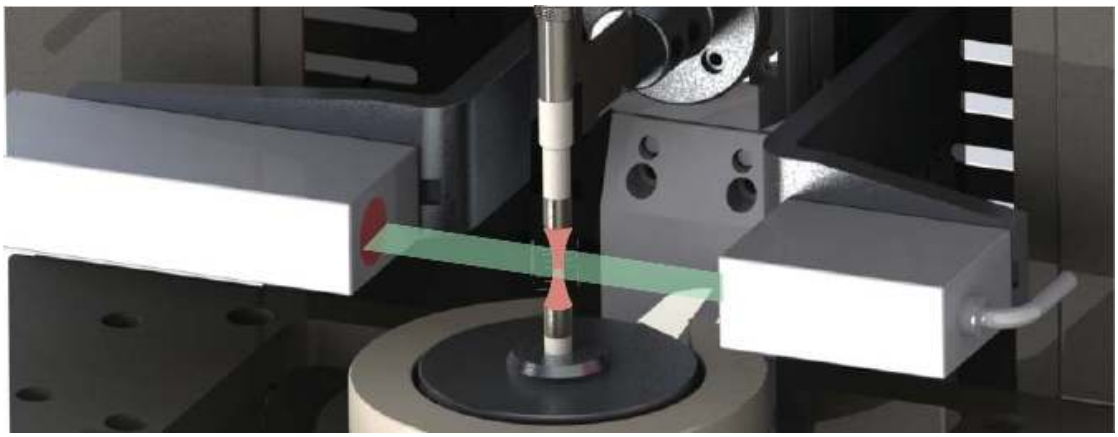

Figure 3.2: FSR measures the diameter at midfilament position, i.e. at the point of highest stress [156].

3.2 Sample Preparation

Polystyrene samples after the synthesis procedure are precipitated into MeOH, collected and dried for 24 hours at 50°C. If the needed sample consisted of several polymers, blends were produced by dissolving the weighted amount of polymers in THF overnight at room temperature and then poured into methanol and filtrated. Polymers and polymer blends are then dried in vacuum for 2 weeks at 70°C to remove all solvents. After that, approximately 0.1 g of the dried polymer or blend is hot-pressed into a cylindrical pellet (diameter — 9 mm, height — 2.5 mm) for 10 minutes at 140°C and allowed to cool down. A pellet is mounted on the bottom plate of the FSR, pre-heated to 150°C, and the upper plate is moved down to the sample. Before the experiments, the sample is left at this temperature to fully relax from any stresses which were monitored by the load cell [157].

3.3 Uniaxial extension

The load cell at the bottom plate of the FSR measures the force, $F(t)$, during the uniaxial extension. At the same time, the diameter in the middle of the filament, $2R(t)$, is measured by the laser micrometer. This data is then used to calculate the Hencky strain:

$$\epsilon(t) = -2 \ln\left(\frac{R(t)}{R_0}\right), \tag{3.1}$$

with R_0 being the initial radius of the sample. The strain rate is then defined as:

$$\dot{\epsilon} = \frac{d\epsilon}{dt} \tag{3.2}$$

Since filament radius decreases exponentially at:

$$R(t) = R_0 \exp(-0.5\dot{\epsilon}_0 t), \tag{3.3}$$

the value of the stress difference is calculated based on the acquired data from $R(t)$ and $F(t)$ (ignoring inertial and surface tension effects) [158]:

$$\langle \sigma_{zz} - \sigma_{rr} \rangle = \frac{F(t) - m_f g/2}{\pi R(t)^2}, \tag{3.4}$$

with m_f being the filament weight and g — gravitational acceleration. It has to be noted that at small aspect ratios $\Lambda_0 = L_0/R_0$ with L_0 being the initial length of the sample, a part of stress difference originates from the radial variation because of small shear components in the field of deformation. This effect is nullified with the use of correction factor with the corrected mean value of the stress difference being [157, 159]:

$$\langle \sigma_{zz} - \sigma_{rr} \rangle_{corr} = \langle \sigma_{zz} - \sigma_{rr} \rangle \left[1 + \frac{\exp\left(-5\epsilon/3 - \Lambda_0^3\right)}{3\Lambda_0^2}\right]^{-1} \tag{3.5}$$

The radial variation of the stress is insignificant at large strains and therefore this correction becomes unnecessary [152]. Dividing the mean difference stress value by the Hencky strain rate, the value for extensional stress growth coefficient is then obtained [154]:

$$\overline{\eta}^+ = \frac{\langle \sigma_{zz} - \sigma_{rr} \rangle_{corr}}{\dot{\epsilon}} \tag{3.6}$$

3.4 Stress relaxation

Stress relaxation is measured after uniaxial extension. At a certain Henky strain ϵ_0 the extension is stopped resulting in $\dot{\epsilon} = 0$. Even though necking instabilities cause problems during the stress relaxation procedure [160], the use of a close loop controller enables to control the diameter of a filament precisely giving the needed Hencky strain during the necking phase [157, 160, 161].

3.5 Filament quenching

After uniaxial extension or stress relaxation procedures polymer samples are quenched below the polymer glass transition temperature by cold nitrogen flow saving the macromolecular configurations. The 'frozen' samples [Fig. 3.3] are stored at room temperature and then used for the small-angle neutron scattering experiments.

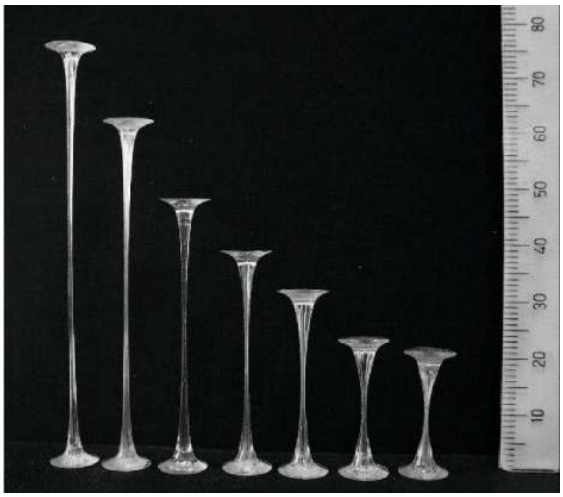

Figure 3.3: Polymer samples, left to right: 0, 10, 20, 80, 320, 1260 and 12000 seconds after stress relaxation.

The cooling rate was sufficiently enough to freeze filaments faster than the Rouse time of the polymer chain, which ensures the stability of molecular configurations [154].

3.6 Data for the SANS series

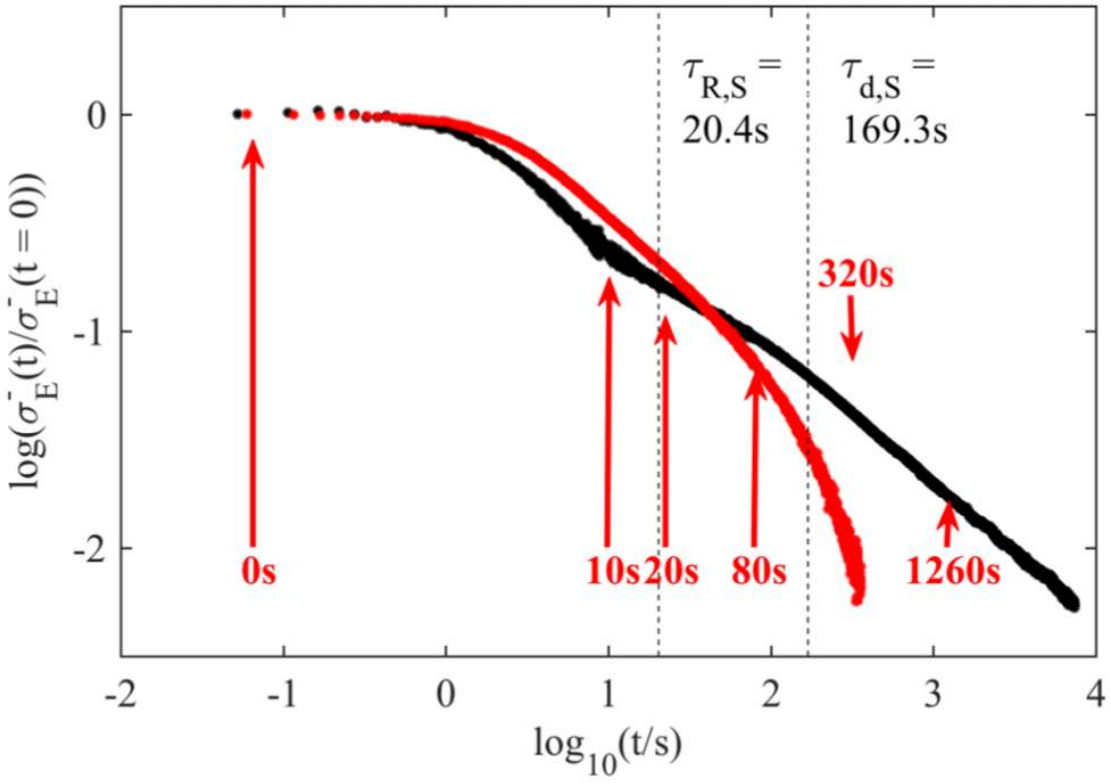

Figure 3.4: Tensile stress relaxation of the polymer blend made of 545 and 95 kg/mol linear PS (black) and the blend of 95 and 86 kg/mol linear PS (red) samples at 130°C after cessation of fast uniaxial elongational flow at Hencky strain = 3 and strain rate = $0.1\ s^{-1}$. Dashed vertical lines indicate the short chain Rouse and reptation time. Red arrows indicate times where a quenched sample was produced for scattering studies [162].

3.7 Stability of the Star Polymers during the Rheological Studies

Despite the inert atmosphere during the FSR measurements, some macromolecular architectures are liable to degrade [157] under experimental conditions. A part of our studies was allocated to synthesize branched high molecular structures able to survive increased temperatures and to establish reasons why similar macromolecules can either degrade or not.

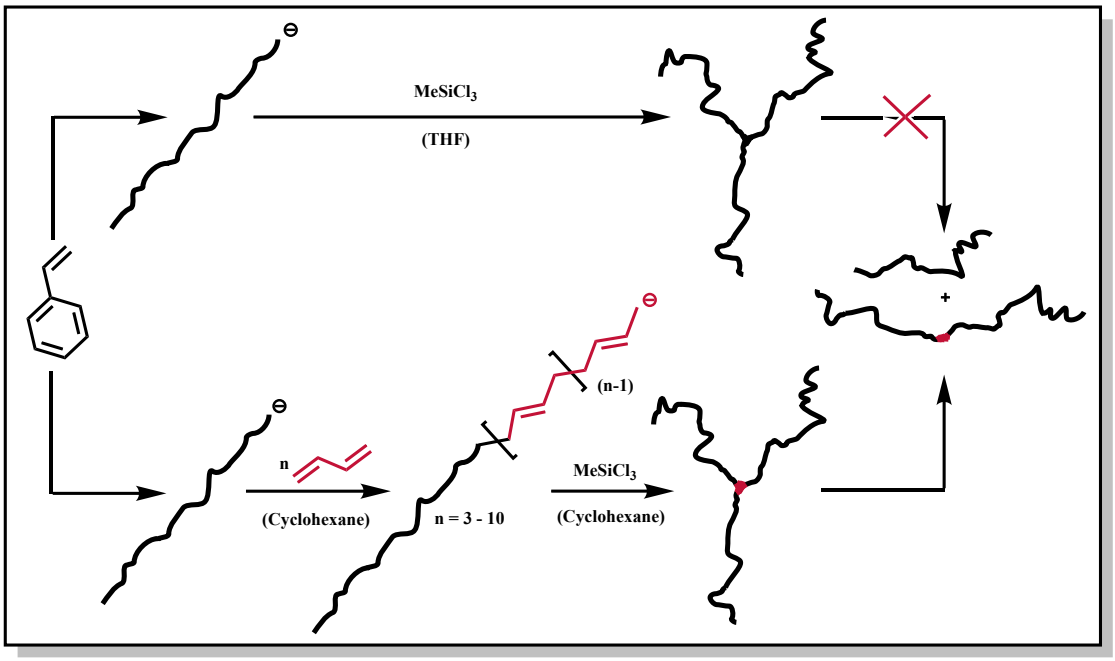

Figure 3.5: Two synthetic routes to the same branched molecular architectures with different stabilities against radicals at elevated temperatures.

The output for these investigations is that the macromolecular architectures with the butadienyl block linked with the silicon atom are prone to degradation during the FSR experiments. The trick of converting sterically hindered living anions to a smaller butadienyl anionic moiety, which is used among synthetic chemists [163] in order to obtain higher yields of higher molecular weight polymers introduces a weak point near the branching site, that can be easily attacked by radicals at elevated temperatures. The two synthetic routes for 3-arm star polymers are shown in Fig. 3.5, while the detailed information on the star polymers stability is given in Appendix A.

CHAPTER 4

Neutron Scattering

4.1 Overview

In this chapter general scientific nomenclature and basic theory behind neutron scattering and specifically, small-angle neutron scattering will be introduced. The chapter presents well-established knowledge taken from the book 'Neutron Scattering and Other Nuclear Techniques for Hydrogen in Materials' [164], otherwise a reference to a specific paper is provided.

4.2 Why Neutrons

Neutron scattering is a technique which is able to effectively probe atomic positions of light elements on mesoscale and, at the same time, to distinguish the scattering power of two lighter hydrogen isotopes which is crucial for the compounds of current research that are labeled with deuterium, thus giving insight into the structural characteristics depending on stretching and relaxation. Moreover, it is the only method to see conformation of a whole polymer chain, using the labelling method described thereinbefore. Polymers of interest for the rheology studies in this work are represented by light elements only, making other research techniques (X-ray/electron scattering, etc.) pointless to use. Since there is no alternative to neutron scattering for such studies, researchers in this area have to deal with pale neutron fluxes, weak scattering and limited beamtimes.

4.3 Production of Neutrons

There are two well-established routes to produce neutrons: nuclear spallation, which is caused by collision of accelerated high-energy protons targeted at a heavy metal and nuclear fission, for which ^{235}U is commonly used. We used both types of neutron sources in this work. Neutrons, once created, are guided to moderators in order to tune their energies so they can be used in scattering experiments. Neutrons reach thermal equilibrium with the moderator and by means of that slow down. Typical moderators at this stage are H_2O and D_2O at room temperature, that tune the Maxwell-Boltzmann distribution of wavelengths to the one with a peak at 0.18 nm. Wavelengths of neutrons can also be tuned at hot (graphite, 2000 K) or cold (D_2 or H_2, 20 K) moderators to be suitable for different experiments. Further, the wavelength spread of neutrons is either cut by a monocrystal of a reflective material (monochromator) allowing only those neutrons that satisfy the Bragg law pass in the direction of an instrument or a specific wavelength is selected by a mechanical velocity selector. Monochromized beam consists only of $\approx$ 1% of the total number of neutrons.

4.4 Detection of Neutrons

Neutrons are detected indirectly, registering positively charged particles that are made after such nuclear reactions, as:

$$n + {}^{3}He \longrightarrow {}^{3}H + p + 765\ keV, \tag{4.1}$$

$$n + {}^{10}B \longrightarrow {}^{7}Li + {}^{4}He + 2310\ keV, \tag{4.2}$$

in an ionization medium made of carbon dioxide, methane or argon. Since the gases for detection (^{3}He or $^{10}BF_3$) are either extremely expensive or highly toxic, nowadays a certain effort is headed towards the production of a new type of detectors without these drawbacks and that are possibly able to provide a higher count rate for brighter fluxes that are expected at, for example, European Spallation Source. A potential replacement could be the neutron scintillator with the nuclear reaction:

$$n + {}^{6}Li \longrightarrow {}^{4}He + {}^{3}H + 4790\ keV, \tag{4.3}$$

followed by ZnS excitation by the energy of the reaction. ZnS is then emitting light of a wavelength of 470 nm, which is further photomultiplied and recorded via a CCD-camera. Neutron scintillators are, though, limited in counting rate because of the long afterglow after a neutron capture due to the thickness of the material used, which is set by opaqueness of its own light.

Some research is aimed at the boron-lined converter as a promising alternative to the present neutron detectors. It utilizes the idea of $^{10}B_4C$ film for a counting tube. If a neutron is captured by a ^{10}B atom, the reaction product ionizes the gas inside the tube, which is then recorded. The use of this detector design is though limited by a lower detection rate compared to ^{3}He detectors.

4.5 Neutron Interactions with Matter

Neutrons are non-charged particles interacting with atom nuclei and, due to the existence of magnetic dipole momentum raised from three charged quarks in the composition of neutrons, with the unpaired electrons or magnetic nuclei in magnetic atoms. Neutrons may be scattered elastically and inelastically or absorbed by matter. The further description will be narrowed to one type of scattering, since for the needs of present studies only the repertoire of elastic scattering techniques was in demand, while the inelastic part of the scattering data gave rise to some background noise in the raw scattering data and was therefore disregarded.

4.6 Basic SANS theory

SANS is a non-destructive low-resolution method giving averaged information on structures from about 10 Ångströms to thousands of Ångströms within the volume subjected to a neutron beam. This specificity is crucial for the application of the method in polymer research, since there is no necessity to visualize each individual macromolecule, while on the other hand there is a need to probe the bulk which is not possible with transmission electron or atom force microscopy. The power of SANS was utilized with the help of specific synthesis of targeted macromolecules bearing hydrogen and deuterium atoms that provide the difference in scattering length densities in order to highlight the domains of specific interest, as in our case, the individual (statistically averaged) molecules for polymer physics studies.

4.6.1 Scattering Vector

Neutron waves/particles [165] are scattered on nuclei of materials, spreading out as spherical waves. In this thesis we focus only on elastic, non-magnetic scattering of neutrons, the case where no energy has been transferred from a neutron to a nucleus. The scattering vector, Q, is then defined as the vector equal to the difference between the scattered, $\mathbf{k}_f$, and incident, $\mathbf{k}_i$, neutron wave numbers:

$$Q = |\mathbf{k}_f - \mathbf{k}_i| = \frac{4\pi}{\lambda} \sin\theta, \tag{4.4}$$

with λ being the neutron wavelength and θ being a half of a scattering angle.

4.6.2 Interaction Radiation/Sample

When a neutron wave is scattered by one atom, the incoming plane wave/particle is then defined as:

$$a(\mathbf{r}) =_o e^{i\mathbf{k}_i \cdot \mathbf{r}}, \tag{4.5}$$

with $e^{i\mathbf{k}_i \cdot \mathbf{r}}$ being the standard exponential notation with no time dependence and $\mathbf{r}$ being the positional variable. If we introduce a distance, D, from a detector to this equation, we can express it as:

$$a_1^f(\mathbf{D}) = a_o b_1 \frac{e^{i\mathbf{k}_f \cdot \mathbf{D}}}{D}, \tag{4.6}$$

with $1/D$ being a term, accounting for the spherical wave and b_1 being the scattering length for neutrons, the term that accounts for the interaction with a nucleus.

If a neutron wave is scattered by another nucleus, the scattered wave will have a path difference with respect to the first neutron wave. It is expressed as $-\frac{\mathbf{Q}}{k} \cdot \mathbf{r}$, with $\mathbf{r}$ being the vector between two nuclei. The resulting phase difference hence will be $-\mathbf{Q} \cdot \mathbf{r}$. Further introduction of a distance r between two nuclei, will end up in the sum expressed as:

$$a_2^f(\mathbf{D}) = a_o b_2 \frac{e^{i\mathbf{k}_f \cdot \mathbf{D}}}{D} e^{-i\mathbf{Q} \cdot \mathbf{r}} + a^{f_1}(\mathbf{D}), \tag{4.7}$$

with b_2 being the scattering length of the second atom, the index in term a_2 to show that this is a system of 2 atoms and the phase term accounting for the interference. In a system of n atoms the total scattered wave may be expressed as:

$$a_f(\mathbf{D}) = \frac{a_o}{\mathbf{D}} e^{i\mathbf{k}_f \cdot \mathbf{D}} \sum_{j=1}^{n} b_j e^{-i\mathbf{Q} \cdot \mathbf{r}_j}, \tag{4.8}$$

where r_j is the position of nuclei j relative to nuclei 1 and with the averaged scattered intensity being:

$$\left\langle I_f(\mathbf{D}) \right\rangle = \left\langle a_f(\mathbf{D}) a_f^*(\mathbf{D}) \right\rangle = \frac{a_o^2}{D^2} \left\langle \sum_{j=1}^{n} b_j e^{-i\mathbf{Q} \cdot \mathbf{r}_j} \sum_{k=1}^{n} b_k^* e^{-i\mathbf{Q} \cdot \mathbf{r}_k} \right\rangle \tag{4.9}$$

which is then rewritten as:

$$\left\langle I_f(\mathbf{D}) \right\rangle = \frac{a_o^2}{D^2} \left\langle \sum_{j,k=1}^{n} b_j b_k^* e^{-i\mathbf{Q} \cdot \mathbf{r}_{jk}} \right\rangle \equiv \frac{a_o^2}{D^2} \frac{d\sigma}{d\Omega}(\mathbf{Q}) \tag{4.10}$$

where the term $d\Omega$ is the solid angle, which is covered by a detector, and the term $\frac{d\sigma}{d\Omega}$ is the differential scattering cross section, which shows the number of neutrons per second which are scattered into a solid angle and normalised to the neutron flux. The second term may be also rewritten in terms of unit sample volume, V, giving the differential scattering cross section per unit sample volume:

$$\frac{d\Sigma}{d\Omega}(\mathbf{Q}) = \frac{1}{V}\frac{d\sigma}{d\Omega} = \frac{1}{V}\sum_{j,k=1}^{n}\left\langle b_j b_k^* e^{-i\mathbf{Q}\cdot\mathbf{r}_{jk}}\right\rangle \tag{4.11}$$

This equation shows the interaction between the beam and the sample providing the information about the structure of the sample independent from the experimental setup.

4.6.3 Form and Structure Factors

A pattern which is recorded at a detector is the sum of all the interfered neutron wave amplitudes squared and may be mathematically represented using the terms that describe the shape of particles in a sample; their position, i.e. how they arranged with respect to each other; a constant term to which particle contrast, volume and concentration contribute. To deduct the final equation for this idea we have to start from the scattering length density of an inhomogeneous particle:

$$\rho(\mathbf{r}) = \sum \phi_j(\mathbf{r}) b_j \tag{4.12}$$

with ϕ_j being the local number density of a given isotop of an atom type in the particle of volume V_p (which could be a monomer volume). Now we define the scattering length density of a mixture of deuterated and non-deuterated polymers giving the scattering length difference:

$$\Delta\rho(\mathbf{r}) = \rho_H(\mathbf{r}) - \rho_D(\mathbf{r}) \tag{4.13}$$

The scattering amplitude is then calculated by integrating the scattered wave over all the atoms in volume of the whole sample V_p:

$$a_f(\mathbf{Q}) = \int_{V_p} \Delta\rho(\mathbf{r}) e^{-i\mathbf{Q}\cdot\mathbf{r}} d\mathbf{r} \tag{4.14}$$

In a system of N identical scattering elements at positions r_j between them the total scattered wave is expressed as:

$$A_f(\mathbf{Q}) = \sum_{j=1}^{N} a_j^f(\mathbf{Q}) e^{-i\mathbf{Q}\cdot\mathbf{r}_j} \tag{4.15}$$

with $e^{-i\mathbf{Q}\cdot\mathbf{r}_j}$ being the phase term that describes the position of the particles.
The resulting scattering is then:

$$\frac{d\Sigma}{d\Omega}(\mathbf{Q}) \propto \frac{1}{V}\left\langle A_f(\mathbf{Q}) A_f^*(\mathbf{Q})\right\rangle \tag{4.16}$$

We assume that the scatterers are randomly oriented resulting in the spherical symmetry of the scattered intensity:

$$\frac{d\Sigma}{d\Omega}(\mathbf{Q}) = I(\mathbf{Q}) = I(Q) \tag{4.17}$$

Further development including intermolecular correlations gives rise to a structure factor $S(Q)$, that in the simple approximation may be multiplied to the form factor $P(Q)$ according to:

$$I(Q) \propto \frac{N}{V} \langle \Delta\rho \rangle^2 V_p^2 P(Q) S(Q) \tag{4.18}$$

with $\langle \Delta\rho \rangle^2$ being the contrast factor, $\frac{N}{V}$ — concentration, V_p — particle volume, $P(Q)$ — form factor, bearing information about individual particles and $S(Q)$ — structure factor, with the information about interactions between the particles.

4.6.4 Guinier Law

Guinier Law [166–168] is derived [169] substituting the McLaurin series (Taylor series expansion of a function about 0):

$$\frac{\sin(Qr)}{Qr} = 1 - \frac{Q^2 r^2}{6} + \frac{Q^4 r^4}{120} - \cdots \tag{4.19}$$

into the equation of intensity of scattering:

$$I(Q) = 4\pi \int_0^D \gamma(r) \frac{\sin(Qr)}{Qr} r^2 dr \tag{4.20}$$

with D being the largest dimension in a particle. The substitution gives:

$$\begin{aligned} I(Q) &= 4\pi \int_0^D \gamma(r) \left[1 - \frac{1}{6} Q^2 r^2\right] r^2 dr \\ &= 4\pi \int_0^D \gamma(r) r^2 dr - \frac{4\pi}{6} Q^2 \int_0^D \gamma(r) r^4 dr \\ &= I(0)(1 - \frac{1}{3} R_G^2 Q^2) \end{aligned} \tag{4.21}$$

where

$$I(0) = 4\pi \int_0^D \gamma(r) r^2 dr \tag{4.22}$$

and

$$R_G^2 = \frac{\frac{1}{2} \int_0^D \gamma(r) r^4 dr}{\int_0^D \gamma(r) r^2 dr} \tag{4.23}$$

In proximity $Q = 0$ the right side of Eq. 4.19 can be rewritten as the first two terms of the McLaurin series of function $\exp(-R_G^2 Q^2/3)$. Finally, for $Q_{\max} \cdot R_G \leq 1.2$ [170], one can write the Guinier equation:

$$I(Q) = I(0) \exp(-R_G^2 Q^2/3) \tag{4.24}$$

4.6.5 Deuterium Labelling

For the contrast variation tables with scattering length, b, are utilized, and the total scattering cross section is defined as:

$$\sigma_s = \sigma_c + \sigma_i, \tag{4.25}$$

with σ_c being the coherent scattering, proportional to b_c^2, and σ_i — the incoherent scattering, proportional to b_i^2, giving background noise. The scattering lengths of two hydrogen isotopes are presented in Fig. 4.1. The elastic cross section at low energies is determined by the scattering length only.

Scattering length, b, $[10^{-15}m]$	^{1}H	^{2}H
Coherent b_c	-3.74	6.67
Incoherent b_i	25.3	4.04

Table 4.1: Scattering lengths for hydrogen and deuterium [171].

The present research utilizes deuterium labelling of either the whole or a part of a macromolecule in order to 'highlight' polymer behavior during stress and relaxation. The synthetic part of these studies was planned in a manner that enabled contrast by either mixing deuterated and protonated polymers of the same molecular weight or by the synthesis of D- and H-blocks in a *block*-copolymer in a certain proportion, which ensures enough contrast for SANS studies and absence of phase separation. The excess of incoherent scattering, and, thus, problems with background subtraction came from the majority of protonated polymer species with a minority of deuterated ones due to the limited budget of the project, which did not allow buying a lot of deuterated monomers.

4.6.6 Background Subtraction. Porod Approximation

Porod Law [172–174] states that the wave/particle intensity that is elastically scattered by an amorphous system should decrease with the momentum transfer h as h^{-4} [175] if scattering from a sample is dominated by two phases with sharp interface between them.

Its derivation [176] utilizes the formula for scattering intensity of an infinitely dilute solution of spheres of radius R and smooth surfaces:

$$I(Q) = \left(\frac{N}{V}\right) \Delta\rho^2 V_p^2 F^2(QR) \tag{4.26}$$

with (N/V) being the spheres number density, $\Delta\rho^2$ — contrast factor, V_p — sphere volume and $F(QR)$ is the form factor amplitude for a single sphere:

$$F(QR) = \frac{3j_1(QR)}{QR} = \frac{3}{QR}\left(\frac{\sin(QR)}{(QR)^2} - \frac{\cos(QR)}{(QR)}\right) \tag{4.27}$$

The form factor for single sphere $P(QR) = F^2(QR)$ may also be defined as:

$$P(QR) = \int d^3r \exp[-i\vec{Q}\vec{r}]P(\vec{r}) = \frac{1}{V_p}\int_0^\infty dr 4\pi r^2 \frac{\sin(Qr)}{Qr}\gamma(r) \tag{4.28}$$

with $P(\vec{r})$ being the pair correlation function, $\gamma(r)$ — radially defined probability distribution, representing the relative fraction of area of one sphere inside a larger sphere integrated over all possible locations, defined as $p(r, r')$:

$$p(r, r') = 1p(r, r') = \frac{1}{2} + \frac{1}{4}\left[\frac{R^2 - r^2 - r'^2}{rr'}\right] \tag{4.29}$$

The first line here represents the case of $(R - r > r')$ and the second $(R - r \leq r')$. Next one can find the radial pair correlation function for a sphere [177]:

$$\gamma(r) = \frac{\int_0^{R_A} dr' 4\pi r'^2 p(r, r')}{\int_0^{R_A} dr' 4\pi r'^2} = 1 - \frac{3}{4}\left(\frac{r}{R}\right) + \frac{1}{16}\left(\frac{r}{R}\right)^2 \tag{4.30}$$

With the use of this form, $P(QR)$ may now be expressed as:

$$P(QR) = \frac{1}{V_p}\int_0^{\infty} dr 4\pi r^2 \frac{\sin(Qr)}{Qr}\left[1 - \frac{3}{4}\left(\frac{r}{R}\right) + \frac{1}{16}\left(\frac{r}{R}\right)^3\right] \tag{4.31}$$

If we integrate this expression by parts three times in order to obtain the highest order in the high-Q expansion, we will end up with the Porod law:

$$P(QR) \sim -\frac{4\pi}{V_p}\frac{2\gamma'(0)}{Q^4} = \frac{S_p}{V_p R^2}\frac{3}{2Q^4 R} = \frac{3}{2R^3}\left(\frac{S_p}{V_p}\right)\frac{1}{Q^4} \tag{4.32}$$

with (S_p/V_p) being the surface to volume ratio. From this equation the scattering intensity can be expressed as $I(Q) = A/Q^4 + B$, with B being the constant background scattering. Now one can compute the background as the slope of the regression line on a plot IQ^4 vs Q^4 and subtract it.

4.6.7 Phase Behavior of *block*-Copolymers and Polymer Blends

Even though universally used techniques of deuterium labelling for neutron scattering research assume thermodynamical identity between the two long-lived hydrogen isotopes [178], it is well known that blends of block copolymers and homopolymers at a range of molecular weights, temperatures and concentrations will likely phase separate [178–184] while pure *block*-copolymers may undergo order-disorder transitions [185–188] that will disturb homogeneity of the samples and cause critical scattering. In brief, the effect behind these observations [179] is due to small differences in segment volume between deuterated and protonated macromolecules. In the case of nearly identical molecular weight ($N_D = N_H = N$), the critical degree of polymerization for an amorphous isotopic polymer blends is given by [179]:

$$N_c = 4k_B T_k / V(\Delta V/V)^2, \tag{4.33}$$

with k_B being the Boltzmann constant, T — upper critical solution temperature, V — average segment volume for the mixture and ΔV — the difference in volumes between protonated and deuterated segments. On the other hand, according to symmetric with respect to the two polymers version of the Flory-Huggins approximation to the mixing free energy [189] , N_c is:

$$N_c = 2/\chi, \tag{4.34}$$

with χ being segment-segment interaction parameter, which may be approximated [190] as:

$$\chi = \frac{V_m}{RT}(\delta_H - \delta_D)^2 \tag{4.35}$$

with V_m being the segment molar volume, and δ_H and δ_D being the Hildebrand solubility parameters.

Since isotopic substitution changes the molecular volume of species, all polymer blends exhibit an interaction parameter, $\chi \propto T^{-1}$, greater than zero, with the limiting single-phase stability χ_s:

$$\chi_s = \frac{(N_D\phi)^{-1} + (N_H(1-\phi))^{-1}}{2} \tag{4.36}$$

where ϕ is the volume fraction of the deuterated species. Fig. 4.1 [181] shows the phase diagram for perprotonated and perdeuterated polybutadienes calculated according to the Flory-Huggins theory.

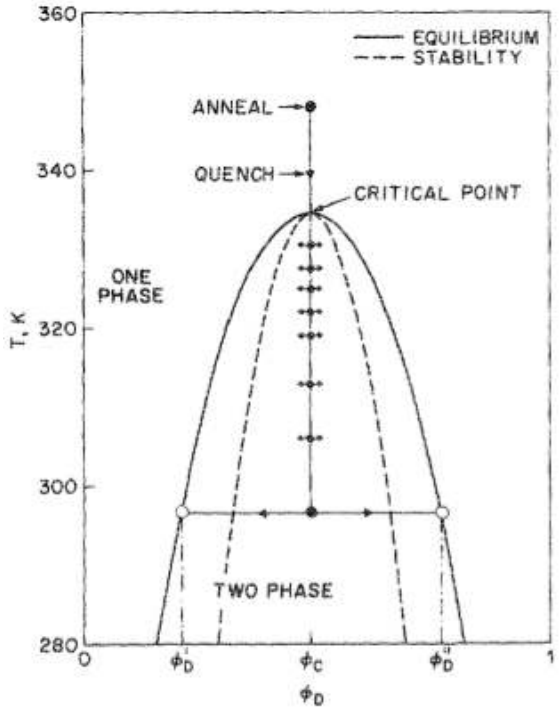

Figure 4.1: [181] Calculated phase diagram for $N_H = 3180$ and $N_D = 3550$, $T_c = 334.5K$ and $\chi = AT^{-1}$. Filled symbols indicate temperatures at which experiments were conducted, open symbols correspond to the equilibrium compositions at 298 K.

4.7 Neutron Facilities

The SANS measurements for these studies were performed at two neutron sites, namely SANS-I instrument at the Swiss Spallation Neutron Source (Paul Scherrer Institute, Villigen, Switzerland) and Quokka instrument at the Bragg Institute of the Australian Nuclear Science and Technology Organization (Lucas Heights, NSW, Australia). The descriptions of the instruments are taken from the papers, written by the instrument scientists [191, 192] or the online guides [193, 194] and are given thereinunder.

4.7.1 SANS-I

SANS-I instrument covers the q-range from $6{\cdot}10^{-3}$ $n\text{m}^{-1}$ to 5.4 $n\text{m}^{-1}$ in a normal regime and up to 10.5 $n\text{m}^{-1}$ with a vertically displaced detector, which gives a possibility to investigate structures from 1 to 400 nm. Neutrons are being produced at the spallation source, guided through a cold D_2 moderator to filter epithermal and higher energy neutrons, monochromized by a mechanical helical slot velocity selector (giving the resolution of the beam $\Delta\lambda/\lambda \approx 10\%$), hit a sample and then measured by an area sensitive ^{3}He detector, where the data is acquired in a 128×128 pixel memory corresponding to pixel sizes of 7.5×7.5 $m\text{m}^2$, capable to work at 20 kHz count rate per pixel. The direct beam is blocked by a B_4C movable beamstop, the area of which is masked on the resulting scattering intensity map. The Fig. 4.2, which is taken from Paul Scherrer Institute website [195], shows the schematic of the used instrument, describing its components.

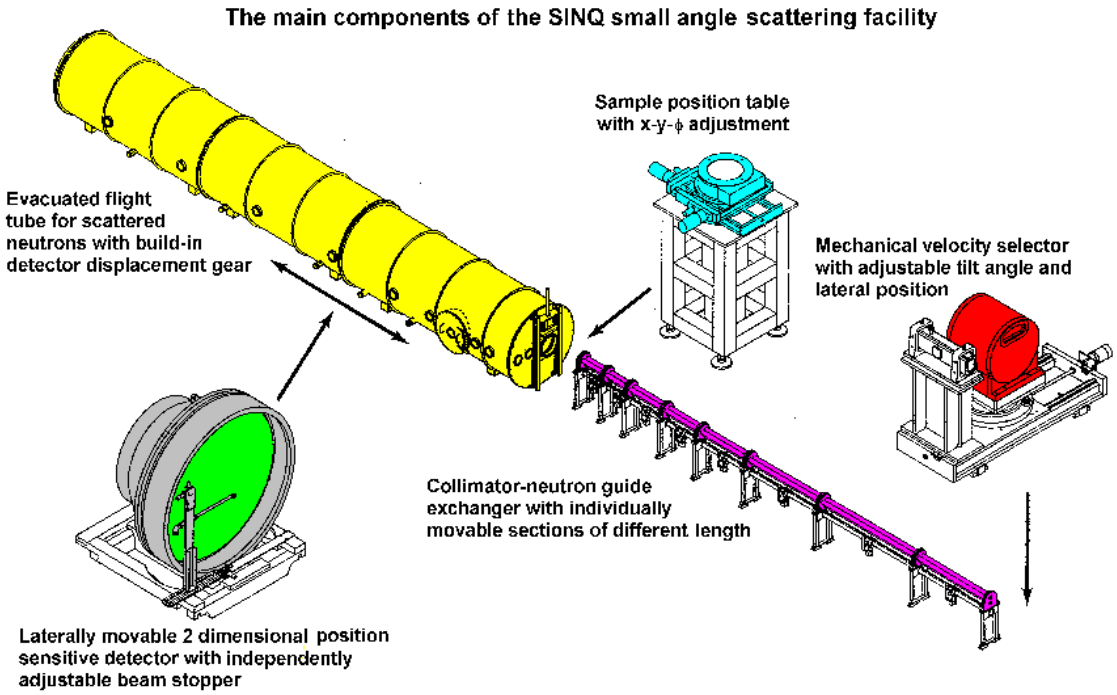

Figure 4.2: The main components of the SANS-I instrument.

4.7.2 Quokka

Quokka is the SANS instrument that receives cold neutrons from the high brilliance cold source of the open-pool Australian lightwater nuclear research reactor (OPAL, 20 megawatt). Neutrons are selected according to velocity with the use of a short rotor (25 cm) and can have the wavelength from 4.5 to 40 Å. Quokka so far has the largest high count rate 2D ^{3}He detector of all SANS instruments: 921600 $m\text{m}^2$, 192×192 pixels, each pixel having the size of 5×5 mm. The detector can be moved laterally by up to 450 mm and from 1.3 up to 20.1 m forth and back inside a vacuumed tube, giving an accessible q-range from $4{\cdot}10^{-3}$ Å^{-1} (or even from

$6{\cdot}10^{-4}$ Å^{-1} with focusing lens optics) to 0.7 Å^{-1} with a conventional resolution $\Delta\lambda/\lambda = 7$-18%. The Fig. 4.3, which is taken from the instrument description paper [192], shows the scheme of the instrument.

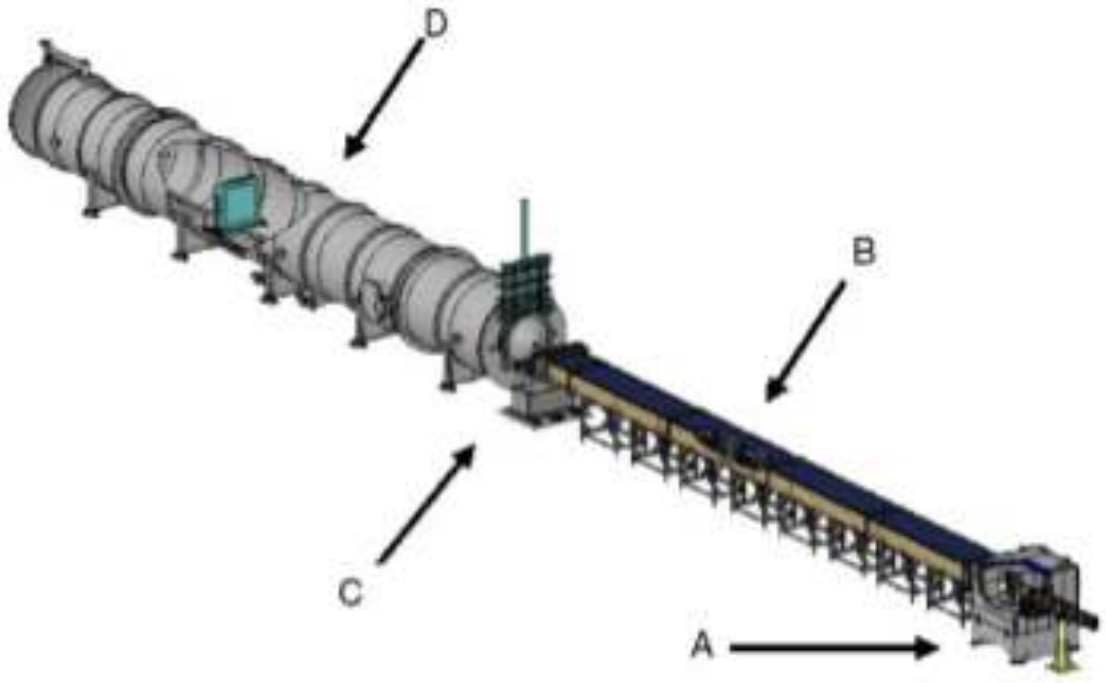

Figure 4.3: The scheme of Quokka SANS instrument at OPAL. A — a mechanical velocity selector, B — collimation system, C — sample area and sample environment, D — secondary flight path to detector in vacuum.

4.8 Data Acquisition

Samples of 'frozen' below the glass transition temperature polystyrenes were mounted on a conventional sample holder, as shown in Fig. 4.4.

Even though the volume of the samples [Fig. 4.4] in the beam was thoroughly calculated in order to correctly subtract the background coming from purely protonated polymers, additional correction based on the slopes of intensity versus scattering vector coming from 1D data was used, as described before [Sec. 4.6.6], since it is almost impossible to estimate the volume of thin rod-like samples subjected to a neutron beam precisely due to the irregular geometry of the samples (some part of the beam passes through no sample and the other part of the beam passes through the PS-filaments) and thereby the correct background to subtract.

For the case of SANS-I, the full q-range for the experiments ($5{\cdot}10^{-3}$ Å^{-1} – 0.25 Å^{-1}) was recorded through 3 overlapping settings of the detector distances (2, 6 and 18 meters) with a neutron wavelength λ = 6 Å at ambient temperature. For the case of Quokka, a similar q-range was obtained through 3 overlapping settings (2, 5 and 18 meters) with a neutron wavelength

Figure 4.4: Mounted samples.

λ = 5 Å at room temperature. All measurements were done until the total count of at least 2 million neutrons.

4.9 Data Treatment

Initial data treatment was done with the use of either BerSANS software package from HMI Berlin (Germany) or the Quokka macros for Igor Pro [196] (NIST Center for Neutron Research, Gaithersburg, MD, USA). Each sample at each detector distance was handled with the following algorithm:

- The area around the beamstop and 1-2 pixels at the edges of the detector is masked;
- The beam center value is corrected according to the one found from the empty beam measurements;
- The scattering pattern is corrected with respect to empty beam radiation;
- The scattering pattern is corrected with respect to each pixel of the detector efficiency with the help of incoherent H_2O scattering;

- The scattering pattern is corrected with respect to the same volume of background — fully protonated polystyrene.

4.10 *Block*-PSD-*block*-PSH 3-Arm Star Small-Angle Neutron Scattering Pattern

Before the experiments, we expected to see the correlation between the end-blocks of the stars, with the idea that at the highest stretch rate, two arms will fall into one tube. This idea is shown in Fig. 4.5.

But during this work, we unexpectedly found coherent intensity peaks in the direction, which is perpendicular, and not parallel to the stretch. Inability to attribute these peaks to chains correlations, voids, impurities and degraded catalyst residues inspires an in-depth research with these types of samples. The two-dimensional scattering data is shown in Fig. 4.6.

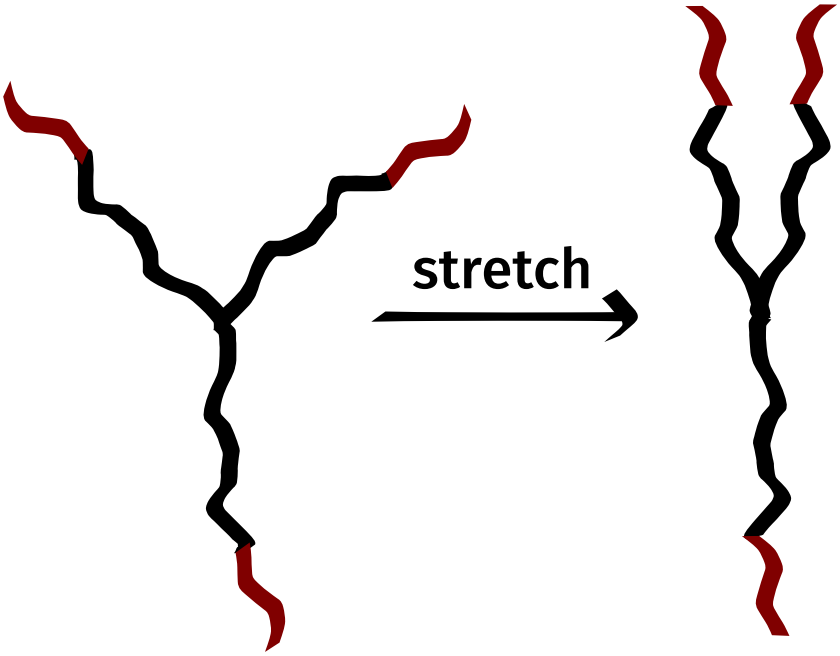

Figure 4.5: Stretching of end-labeled polymer stars.

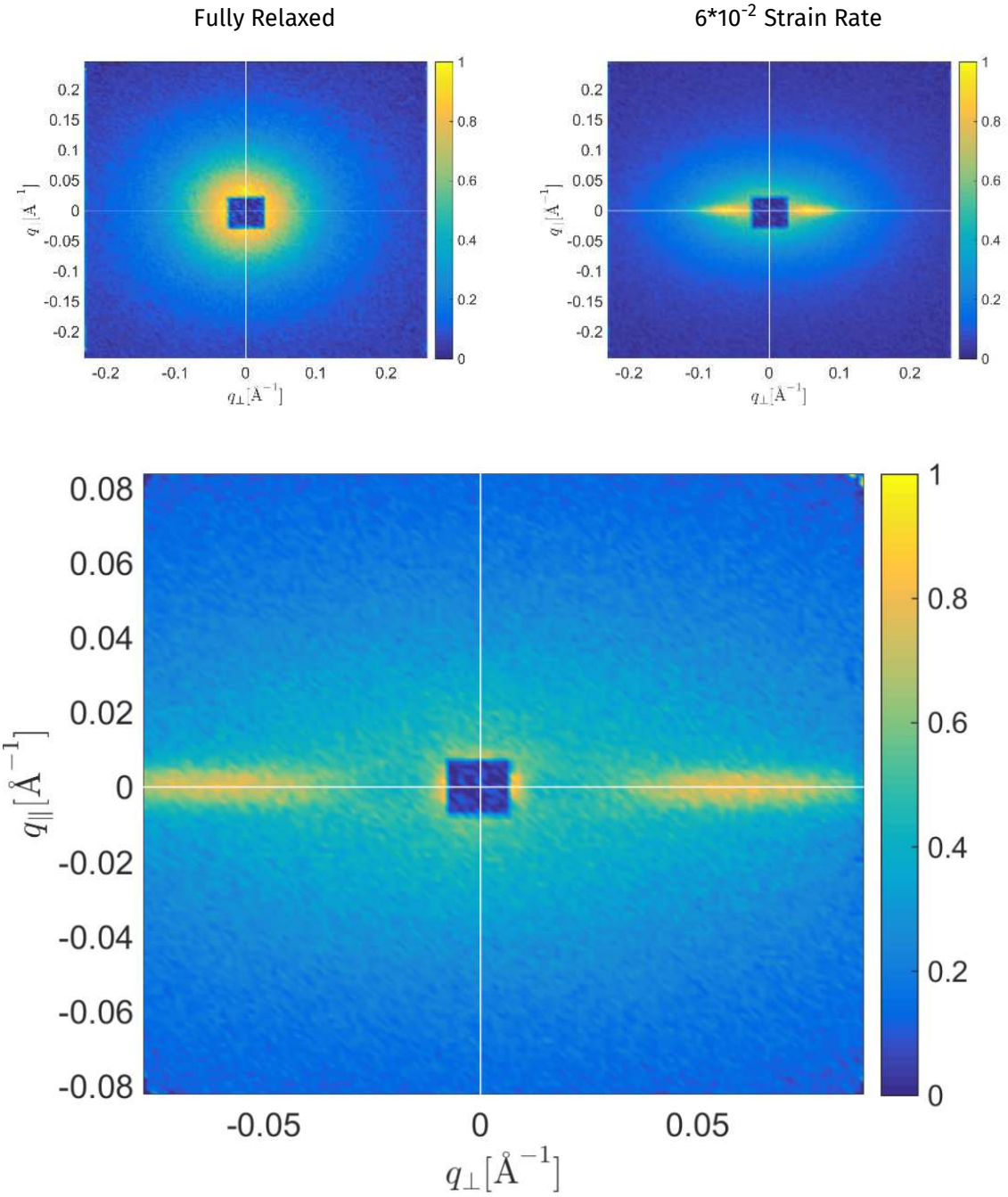

Figure 4.6: Two-dimensional scattering data of *block*-PSD-*block*-PSH 3-arm star polymer in fully relaxed and a stretched state, recorded at two detector distances: 2 (top) and 6 (bottom, stretched only) meters.

4.11 Data Fitting

The data fitting to a large extent was done together with and by prof. Jacob J.K. Kirkensgaard, as it was mentioned in Acknowledgements section.

SANS experiments provide an intensity distribution in reciprocal space and considerable effort has to be invested in the data analysis in order to obtain the corresponding real space structures [197]. This section presents fitting procedures, based on least-squares minimization between a model and a dataset, providing crucial information of radii of gyration in the directions parallel and perpendicular to the flow field. Sections 4.11.1, 4.11.3 and 4.11.4 contain the analytically calculated form factors which were used as the fitting routines for the fully relaxed polymers while Sec. 4.11.2 describes the case of stretched polymer melts.

4.11.1 Linear Polymers with Gaussian Statistics

Debye [198] analytically found the expression for the form factors of flexible polymers that obey Gaussian statistics:

$$P(\mathbf{q}) = \frac{2\left[\exp(-u) + u - 1\right]}{u^2} \tag{4.37}$$

with $u = \langle R_g^2 \rangle q^2$, where $\langle R_g^2 \rangle$ is the ensemble average radius of gyration squared: $\langle R_g^2 \rangle = \frac{Lb}{6}$, and L being the contour length, while b is the statistical segment length.

```
function out = debye(qX,qZ,rgX,rgZ)
x2=(qZ.*rgZ).^2+(qX.*rgX).^2;
out  = 2*(exp(-x2) + x2 - 1)./x2.^2;
```

Listing 4.1: Debye function as used in Matlab.

The form factor may be sometimes used [199] to fit anisotropic data from stretched polymers using $u = \left[q_{\parallel} R_{g\parallel}\right]^2 + \left[q_{\perp} R_{g\perp}\right]^2$, with $R_{g\parallel}$ and $R_{g\perp}$ being the radii of gyration in the directions parallel and perpendicular to the flow field. This assumes the ellipticity of the isointensity contour lines in SANS scattering patterns, with $R_{g\parallel} = \lambda_{\parallel} R_{g0}$ and $R_{g\perp} = \lambda_{\perp} R_{g0}$.

The computer code on Listing 4.1 minimizes the difference between the model and the data fit with the use of the Debye function translated to a Matlab script.

The data for radii of gyrations for fully relaxed samples extracted during the fitting are then also used to check the operability of the computer code made for more advanced theories described in Sec. 4.11.2. An example of datasets together with fitted patterns is shown in Fig. 4.7. The detailed description of the samples and scattering patterns for these fits is given in Appendix C.

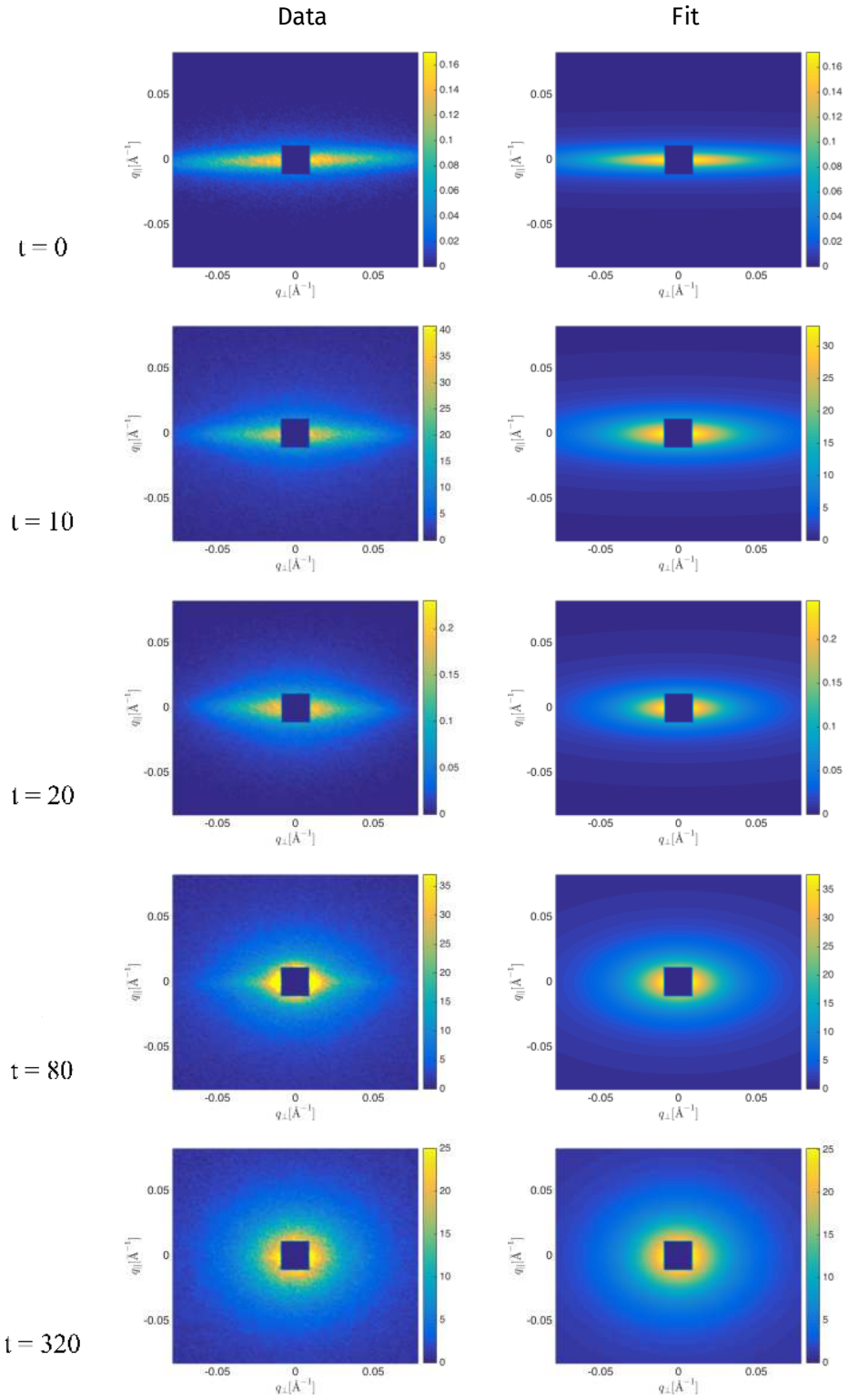

Figure 4.7: Two-dimensional scattering data and accompanying 2D Debye fits for relaxation series of a polymer melt consisting of short (95 kg/mol) and long (545 kg/mol) polystyrene chains.

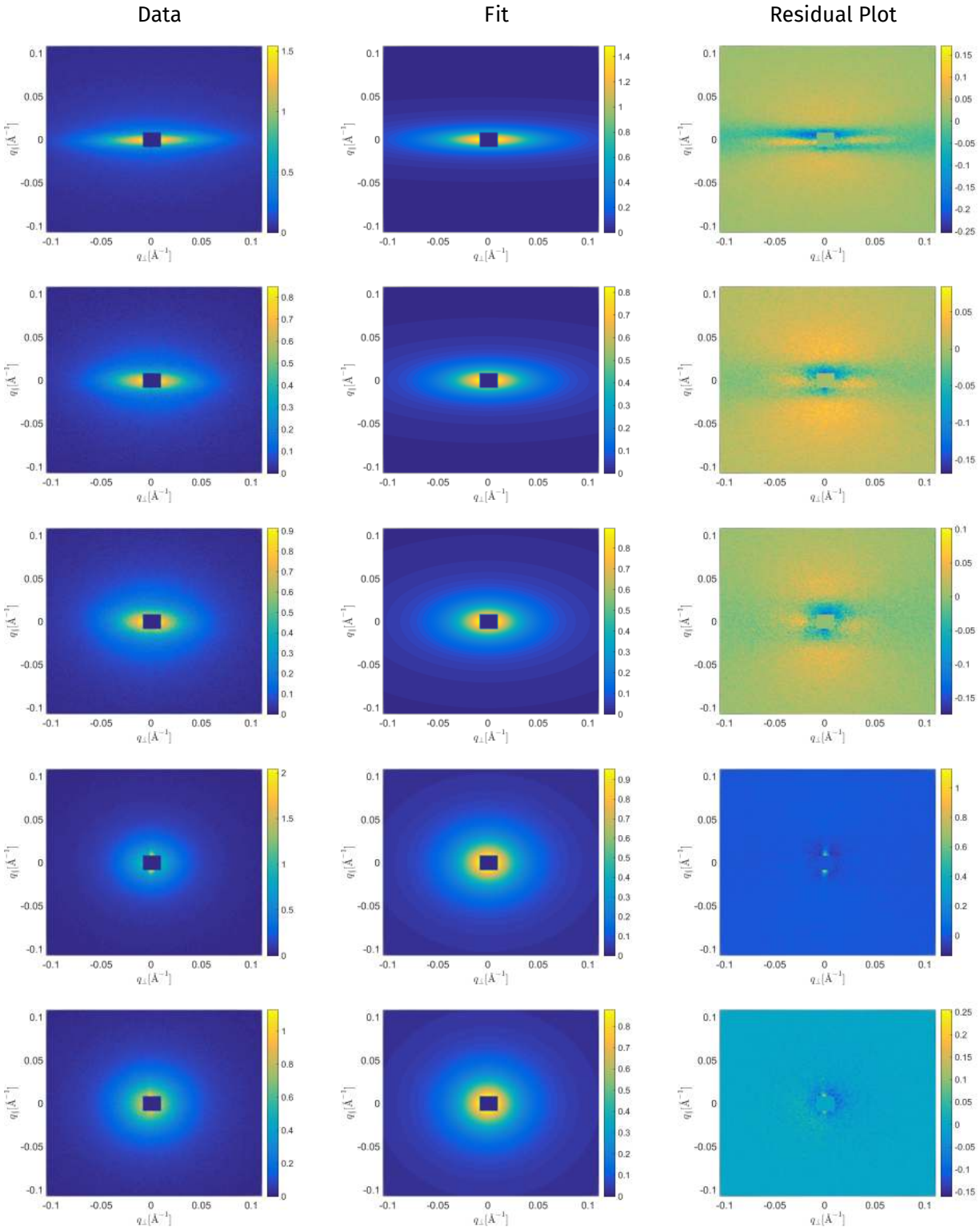

Figure 4.8: Two-dimensional scattering data accompanying 2D Debye fits and residual plots for relaxation series of a polymer blend consisting of short (95 kg/mol — perprotonated, 86 kg/mol — perdeuterated) polystyrene chains. The series consist of stretched polymers, polymers that were relaxed for 10, 20, 80, 320 seconds as shown on consecutive lines respectively.

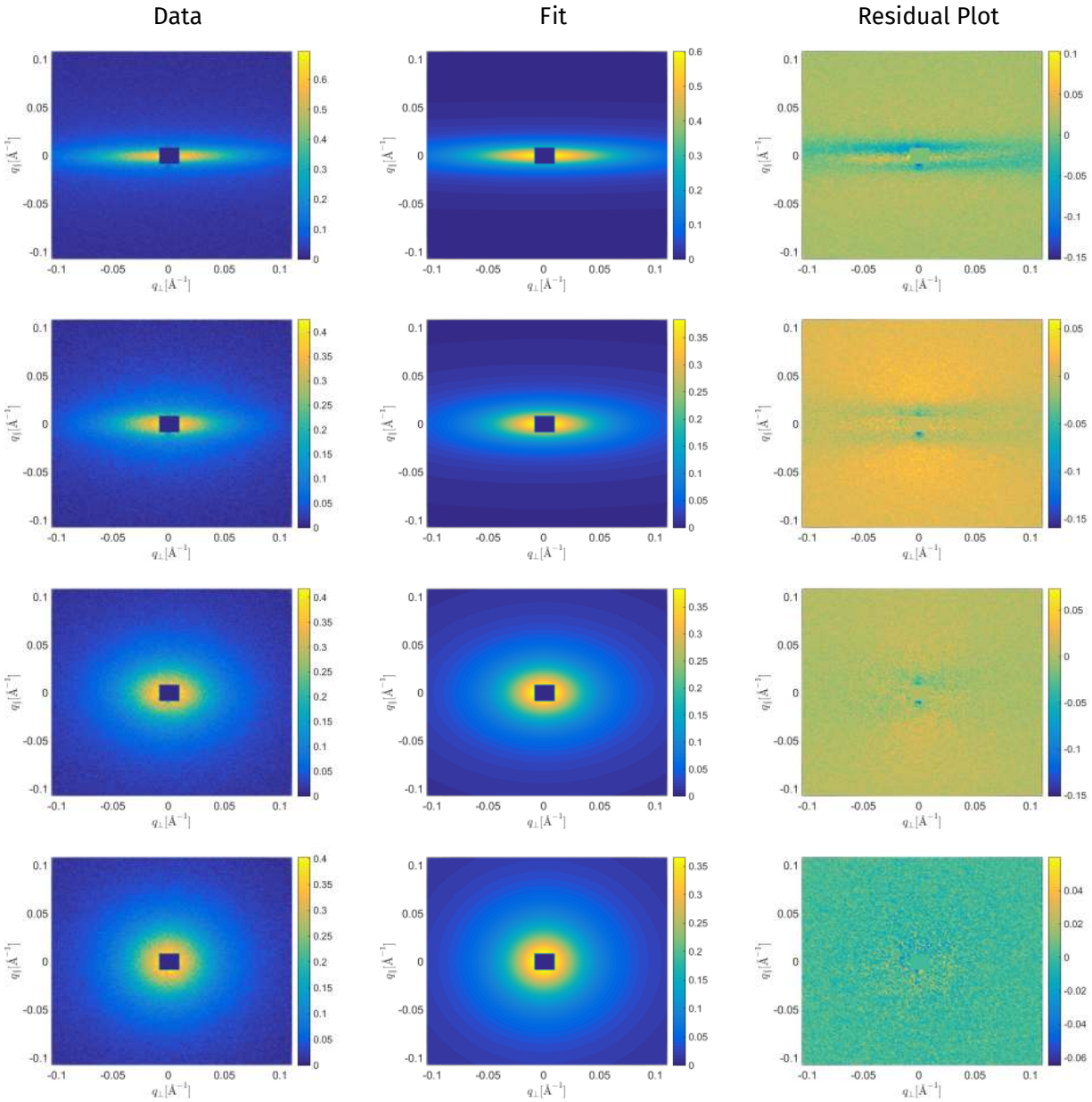

Figure 4.9: Two-dimensional scattering data accompanying 2D Debye fits and residual plots for relaxation series of a polymer melt consisting of short (95 kg/mol) and a *block*-copolymer with deuterated end polystyrene samples. The series consist of strain rates stretched at $6*10^{-2}$, $6*10^{-3}$, $6*10^{-4}$ and a fully relaxed sample, as shown on consecutive lines respectively.

No regression analysis was done to figure out to which extent the Debye model can accurately predict stretched polymer scattering data, however the presented plots are believed to be satisfactory since the residual plots have less than 5% difference between the fit and the model if the points near the beamstop are disregarded, which means that statistical significance of the data fit to the model is less than 5%.

4.11.2 Dangling Ends Model

The inability of the Debye fits to take the scattering contributions from partially relaxed polymer chains that work as a solvent for the strained macromolecules into account necessitates to take the advantage of the 'dangling ends' model (DEM) by Read and McLeish [40]. The model was originally developed for the case of crosslinked polyisoprene networks and is a modified Warner-Edwards model (WEM) [200] with consideration for relaxing macromolecular 'tails'. The model solves 'lozenge' (also called 'diamond') shapes in contour plots of SANS patterns with the use of WEM for the central stretched region represented by η_q:

$$\eta_q(x,x') = \sum_{\mu} Q_\mu^2 \lambda_\mu^2 \mid x - x' \mid + \\ Q_\mu^2(1-\lambda_\mu^2)\frac{d_\mu^2}{2\sqrt{6}R_g^2}\left[1-\exp\left[\frac{2\sqrt{6}R_g^2 \mid x-x' \mid}{d_\mu^2}\right]\right] \tag{4.38}$$

and with the help of Gaussian chain statistics represented by κ_q for the case of either relaxed 'tails' of a polymer chain or isotropic material remained undeformed by the flow field:

$$\kappa_q(x,x') = \sum_{\mu} Q_\mu \mid x - x' \mid \tag{4.39}$$

The index μ represents the cartesian directions, $\mu = (x,y,z)$, $Q_\mu = q_\mu R_g$ being a normalized wave vector, while d_μ is the tube diameter given by

$$d_\mu = d_0 \lambda_\mu^\nu \tag{4.40}$$

with λ_μ being the macroscopic strain ratio in the direction μ. The parameter ν represents the tube potential, that can be either isotropic ($\nu = 0$) or deformed ($\nu = 1/2$). The R_g value is calculated with the Debye or Benoit fits from a fully relaxed sample and the perpendicular strain ratios are related to λ_z as $\lambda_x = \lambda_y = 1/\sqrt{\lambda_z}$.

The model introduces the concept of 'dangling ends', denoted as a fraction f of the total chain being relaxed (Gaussian), and suggests a mechanism of stress relaxation in entangled macromolecules from an end of a structure to its center. The contour length variables for monomeric units l, l' along the chain are defined as $x = l/N$ and $x' = l'/N$, while the total scattering function is represented by

$$S(\mathbf{q}) = 2\int_0^1 \int_0^x dx' \exp\left[-G_q(x,x')\right] \tag{4.41}$$

With $G_q(x,x')$ being

$$G_q(x,x') = \begin{cases} \kappa_q(x,x') & \{x,x'\} \le f \\ \kappa_q(f,x') + \eta_q(x,f) & f < x \le 1-f, x' \le f \\ \kappa_q(f,x') + \eta_q(1-f,f) & 1-f < x, x' \le f \\ \quad +\kappa_q(x,1-f) & \\ \eta_q(x,x') & f < \{x,x'\} \le 1-f \\ \eta_q(1-f,x') + \kappa_q(x,1-f) & 1-f < x, f < x' \le 1-f \\ \kappa_q(x,x') & 1-f < \{x,x'\} \end{cases}$$

The six cases of the functions describe all the possible theoretical positions in a macromolecule:

- the first case represents two theoretical positions, both in the first end;
- the second — one in the first end, one in the central part;
- the third — one in each end;
- the fourth — both in the central part;
- the fifth — one in the second end, one in the central part;
- the sixth — both in the second end.

DEM was used for the case of two polymer blends: first, containing short (86 kg/mol) PSD in the matrix of short (95 kg/mol) PSH, and the second — short (86 kg/mol) PSD in the matrix of long (545 kg/mol) PSH.

The fits to the data are done employing a custom code written in Matlab (The MathWorks Inc., MA, USA) and the general overview of the fitting routine is given onwards.

First, reduced dataset is plotted and the data is checked for consistency: the areas around the beamstop and detector edges should be masked, dataset should be centered around zero.

```
if isempty(gcp('nocreate'));
    myCluster=parcluster('local');
    NW=myCluster.NumWorkers;
    parpool(myCluster,NW);
end;
```

Listing 4.2: Code to implement the parallel computing.

Fitting the theory to experimental scattering patterns is a computationally heavy task, which is why all the fitting procedures were parallelized to increase the speed of the fitting by the factor of the amount of processor cores, which is shown on the Lst. 4.2. This code checks whether a parallel pool is already created and starts one if not. Using this code allows execution of parallelized numerical algorithm operators like **parfor** and **spmd**.

Afterwards, constants should be declared. We define a vector of q-values for each detector distance, where if a pixel on a detector has this q-value, it will be converted to a point of a contour that will be fitted. Also the boundary conditions are declared, since the fitting procedure will only minimize the difference between the model and the experimental datasets and it is not necessarily guaranteed that the output of the fitting will have physical meaning. The boundary conditions have the next constraints: fraction of the relaxed chains f, radius of gyration of a macromolecule in a direction that is perpendicular to the stretch $R_{g\|}$ of each next

sample cannot be smaller than a value from a previous sample in a row of samples relaxing from the highest stretch rate to a fully relaxed state.

Further comes a parallel loop to fit data from each sample. It takes a dataset, all the elements of which are representing the neutron counts, checks it and all the values that are below zero or not numbers are turned into zeros. Next, it imports auxilary information of a beamtime, instrument, distance from a sample to a detector, sample name, sample description and neutron wavelength and creates a coordinate grid in values of scattering vector q (Lst. 4.3) for the case of beamtimes at Paul Scherrer Institute because they are not created automatically during the scattering experiment on SANS-I.

```
for ii = 1:128;
    thetax = 0.5*atan((ii-Cx)*pixelsize/SD);
    thetay = 0.5*atan((ii-Cy)*pixelsize/SD);
    Qx(ii) = (4*pi/lambda)*sin(thetax);
    Qy(ii) = (4*pi/lambda)*sin(thetay);
end;
```

Listing 4.3: Create a coordinate grid in units of q.

The origin in the coordinate grid is centered according to the values obtained at the scattering instrument (Cx and Cy); SD here is the distance from a sample to a detector, $lambda$ is a neutron wavelength and the $pixelsize$ is a size of an ^{3}He cell of the detector on SANS-I. Next a script makes a contour plot of an intensity matrix to give an isoline of the matrix at the certain chosen level. Further comes the fitting procedure. It minimizes the difference between a model and a dataset in terms of least-square routine with the use of an auxilary Matlab function fminsearch [201]. After the fitting, a full scattering pattern is rebuilt from the model parameters and compared with the recorded one and the difference is mapped to a picture which is checked for discrepancies. Fitting with DEM provides essential information not only on $R_{g\parallel}$ and $R_{g\perp}$, but the values of relaxed chains f and tube diameter, which is an additional piece of information to establish the kinetics of flow.

4.11.3 Star Polymers with Gaussian Statistics

Benoit [202] found the expression for the star polymers with Gaussian statistics:

$$P(\mathbf{q}) = \frac{2}{f\nu^2}\left[\nu - \left[1-\exp(-\nu)\right] + \frac{f-1}{2}\left[1-\exp(-\nu)\right]^2\right] \tag{4.42}$$

with $\nu = \frac{u^2 f}{3f-2}$, and $u^2 = \langle R_g^2\rangle q^2$, where $\langle R_g^2\rangle$ is the ensemble average radius of gyration squared of an arm and f stands for the number of arms in a star.

4.11.4 Polydisperse Star Polymers with Gaussian Statistics

Burchard [203] calculated the form factor for star polymers that are polydisperse in a Schulz-Flory sense:

$$P(\mathbf{q}) = \frac{1 + u^2/(3f)}{(1 + u^2(f+1)/(6f))^2} \tag{4.43}$$

where $u^2 = \langle R_g^2\rangle_z q^2$ and $\langle R_g^2\rangle_z$ is the z-average radius of gyration squared of an arm; f stands for the number of arms in a star.

CHAPTER 5

Summary

The modified tube model fails to describe rheological behavior of non-Newtonian fluids out of small deformation rates. The clear understanding of the rheology of complex fluids necessitates the analytical description of processes taking place during strong flows, which may be further added to the groundwork of the Doi-Edwards-de Gennes model. This work provided such relevant experimental data on uniaxial deformation of melts of either blends of linear polymers or star polymers.

5.1 Work Overview

During this work considerable knowledge on model polymer syntheses and polymer stability was gained and connected to the rheological data of the systems mentioned. The synthetic part of this PhD thesis was done jointly with Prof. K. Almdal and consisted of living anionic polymerizations aimed to produce narrowly distributed linear and 3-arm stars polystyrenes, as well as 3-arm *block*-PSD-*block*-PSH and *block*-PSH-*block*-Oligobutadiene stars in a certain range of molecular weights. The star synthesis was made by the means of living anionic polymerization technique resulting in narrowly distributed polymers that are suitable for extensional rheology studies with the help of FSR. The developed synthetic design of the star polymers was specifically directed to produce narrowly polydispersed short polystyrene blocks in polar solvents and to avoid the step of converting polystyrenyllithium to *block*-PSH-*block*-PB, since in the latter case the resulting star polymers are prone to thermal degradation at the starlinking point during typical rheological experiments, such as filament stretching.

The rheological part was done jointly with Prof. O. Hassager and Dr. Q. Huang and consists of uniaxial elongation experiments on either *block*-PSH-*block*-PSD 3-arm stars or blends of randomly distributed star copolymers made of styrene-*d8* and styrene that were carried out with the help of the filament stretching rheometer at DTU. This data has yet to be connected with the SANS patterns, while the rheological description of the linear samples of this research that was done by Dr. L. Hengeller, Dr. Q. Huang and Prof. O. Hassager showed that after uniaxial extension which was followed by stress relaxation experiments of bidisperse polymer blends (made of 95K and 545K PS) the stress in the blend is carried mostly by the long-chain component.

The neutron scattering part was done jointly with J.J.K. Kirkensgaard and K. Mortensen and consisted of SANS experiments at the OPAL reactor and the spallation source at PSI along with all the data treatment procedures and programming of the fitting scripts for the experimental data.

The full scientific cycle of synthesis — rheology — neutron scattering — fitting for linear macromolecules has shown evidence of nematic effects and strain coupling in entangled polymer melts under strong flow, where the presence of long chains delays short chain relaxation by a factor of ~4 and increases their initial stretch. This is a substantial result that increases

our knowledge in the field of polymer physics and we believe it may be mathematically added to the theories of molecular rheology helping to describe elongational processes more thoroughly.

5.2 Future Work

Future synthetic work will most likely focus on the POM-POM *block*-copolymers synthesis employing first generation iterative methodology coupling agents, such as DPEBr1 and DPEBr3 that can be purificated with the aid of the preparative HPLC method on C18 inverted phase columns using acetonitrile/water solvent gradient.

Further rheological characterization will employ large deformations of specifically designed partly deuterated polymer samples up to the highest feasible by the FSR Hencky strain rate followed by stress relaxation in order to unravel large strain polymer dynamics in the nonlinear regime.

This thesis contains up-to-date progress situation in the SANS area which is not finished and future studies are needed to explain intensity peaks in the scattering pattern, particularly using series of the *block*-copolymers, relaxed after an uniaxial flow situation. At the point of the submission of this thesis, only linear polymer blends have been fully characterized and described in the papers attached in Appendices, while the data on star polymers still needs contemplation and time to articulate it in new research papers.

Bibliography

[1] R.S. Graham. “Molecular modelling of entangled polymer fluids under flow”. PhD thesis. The University of Leeds, 2002.

[2] P.-G. de Gennes. “Reptation of a polymer chain in the presence of fixed obstacles”. In: *Journal of Chemical Physics* 55.2 (1971), pp. 572–579.

[3] M. Doi and S.F. Edwards. *The theory of polymer dynamics*. Vol. 73. 1988.

[4] A.L. Frischknecht and S.T. Milner. “Diffusion with Contour Length Fluctuations in Linear Polymer Melts”. In: *Macromolecules* 33.14 (2000), pp. 5273–5277.

[5] P.-G. de Gennes. “Reptation of stars”. In: *Journal De Physique* 36.12 (1975), pp. 1199–1203.

[6] M. Rubinstein and R.H. Colby. “Self-consistent theory of polydisperse entangled polymers: Linear viscoelasticity of binary blends”. In: *The Journal of Chemical Physics* 89.8 (1988), pp. 5291–5306.

[7] A.E. Likhtman and T.C.B. McLeish. “Quantitative Theory for Linear Dynamics of Linear Entangled Polymers”. In: *Macromolecules* 35.16 (2002), pp. 6332–6343.

[8] G. Marrucci and N. Grizzuti. “Fast Flows of Concentrated Polymers - Predictions of the Tube Model on Chain Stretching”. In: *Gazzetta Chimica Italiana* 118.3 (1988), pp. 179–185.

[9] D. Pearson et al. “Transient-Behavior of Entangled Polymers at High Shear Rates”. In: *Journal of Polymer Science* 29.13 (1991), pp. 1589–1597.

[10] G. Marrucci. “Dynamics of entanglements: A nonlinear model consistent with the Cox-Merz rule”. In: *Journal of non-newtonian fluid mechanics* 62.2 (1996), pp. 279–289.

[11] G.H. McKinley and T. Sridhar. “Filament-Stretching Rheometry of Complex Fluids”. In: *Annual Review of Fluid Mechanics* 34.1 (2002), pp. 375–415.

[12] J.-X. Hou et al. “Stress Relaxation in Entangled Polymer Melts”. In: *Phys. Rev. Lett.* 105 (6 2010), p. 068301.

[13] Z.E. Dell and K.S. Schweizer. “Segment-Scale, Force-Level Theory of Mesoscopic Dynamic Localization and Entropic Elasticity in Entangled Chain Polymer Liquids”. In: *arXiv:1607.04355* (2016).

[14] P. Sunthar. “Polymer rheology”. In: *Rheology of Complex Fluids*. 2010, pp. 171–191.

[15] R.G. Larson and P.S. Desai. “Modeling the rheology of polymer melts and solutions”. In: *Annual Review of Fluid Mechanics* 47 (2015), pp. 47–65.

[16] K.S. Schweizer and D.M. Sussman. “A Force-Level Theory of the Rheology of Entangled Rod and Chain Polymer Liquids. I. Tube Deformation, Microscopic Yielding and the Nonlinear Elastic Limit”. In: *arXiv:1604.03971* (2016).

[17] L.J. Fetters et al. “Packing length influence in linear polymer melts on the entanglement, critical, and reptation molecular weights”. In: *Macromolecules* 32.20 (1999), pp. 6847–6851.

[18] D.J. Lohse. “The Critical Role of Anionic Polymerization for Advances in the Physics of Polyolefins”. In: *Anionic Polymerization*. 2015, pp. 1033–1077.

[19] D.J. Lohse. “The influence of chemical structure on polyolefin melt rheology and miscibility”. In: *Journal of Macromolecular Science, Part C: Polymer Reviews* 45.4 (2005), pp. 289–308.

[20] G. Ronca. “Frequency spectrum and dynamic correlations of concentrated polymer liquids”. In: *The Journal of Chemical Physics* 79.2 (1983), pp. 1031–1043.

[21] Y.H. Lin. “Number of entanglement strands per cubed tube diameter, a fundamental aspect of topological universality in polymer viscoelasticity”. In: *Macromolecules* 20.12 (1987), pp. 3080–3083.

[22] T.A. Kavassalis and J. Noolandi. “New view of entanglements in dense polymer systems”. In: *Physical review letters* 59.23 (1987), p. 2674.

[23] R.H. Colby and M. Rubinstein. “Two-parameter scaling for polymers in θ solvents”. In: *Macromolecules* 23.10 (1990), pp. 2753–2757.

[24] L.J. Fetters et al. “Connection between polymer molecular weight, density, chain dimensions, and melt viscoelastic properties”. In: *Macromolecules* 27.17 (1994), pp. 4639–4647.

[25] L.J. Fetters, D.J. Lohse, and W.W. Graessley. “Chain dimensions and entanglement spacings in dense macromolecular systems”. In: *Journal of Polymer Science Part B: Polymer Physics* 37.10 (1999), pp. 1023–1033.

[26] S.L. Wingstrand et al. “Linear and nonlinear universality in the rheology of polymer melts and solutions”. In: *Physical Review Letters* 115.7 (2015), p. 078302.

[27] M. Doi and S.F. Edwards. *The Theory of Polymer Dynamics*. 1986.

[28] H.J. Unidad et al. “Consequences of Increasing Packing Length on the Dynamics of Polymer Melts”. In: *Macromolecules* 48.18 (2015), pp. 6638–6645.

[29] K.S. Cho et al. “Effect of temporary network structure on linear and nonlinear viscoelasticity of polymer solutions”. In: *Korea-Australia Rheology Journal* 27.2 (2015), pp. 151–161.

[30] P.E. Rouse Jr. “A theory of the linear viscoelastic properties of dilute solutions of coiling polymers”. In: *The Journal of Chemical Physics* 21.7 (1953), pp. 1272–1280.

[31] B.H. Zimm. “Dynamics of polymer molecules in dilute solution: viscoelasticity, flow birefringence and dielectric loss”. In: *The Journal of Chemical Physics* 24.2 (1956), pp. 269–278.

[32] M. Mondello et al. “Dynamics of n-alkanes: Comparison to Rouse model”. In: *arXiv preprint physics/9802022* (1998).

[33] D.J. Plazek et al. “Breakdown of the Rouse model for polymers near the glass transition temperature”. In: *The Journal of chemical physics* 98.8 (1993), pp. 6488–6491.

[34] J.T. Kalathi et al. “Rouse mode analysis of chain relaxation in polymer nanocomposites”. In: *Soft Matter* 11.20 (2015), pp. 4123–4132.

[35] J. Cao et al. “Large deviations of Rouse polymer chain: First passage problem”. In: *The Journal of chemical physics* 143.20 (2015), p. 204105.

[36] C. Bennemann et al. “Molecular-dynamics simulation of a glassy polymer melt: Rouse model and cage effect”. In: *Computational and Theoretical Polymer Science* 9.3 (1999), pp. 217–226.

[37] Y. Lu et al. “Molecular Mechanisms for Conformational and Rheological Responses of Entangled Polymer Melts to Startup Shear”. In: *Macromolecules* 48.12 (2015), pp. 4164–4173.

[38] M. Keshavarz et al. “Nanoscale study of polymer dynamics”. In: *ACS Nano* 10.1 (2015), pp. 1434–1441.

[39] A.Y. Grosberg et al. “Scale-Dependent Viscosity in Polymer Fluids”. In: *The Journal of Physical Chemistry B* (2016).

[40] D.J. Read and T.C.B. McLeish. “Microscopic Theory for the “Lozenge” Contour Plots in Scattering from Stretched Polymer Networks”. In: *Macromolecules* 30.20 (1997), pp. 6376–6384.

[41] R.S. Graham et al. “Microscopic theory of linear, entangled polymer chains under rapid deformation including chain stretch and convective constraint release”. In: *Journal of Rheology* 47.5 (2003), pp. 1171–1200.

[42] F. Snijkers et al. “Perspectives on the viscoelasticity and flow behavior of entangled linear and branched polymers”. In: *Journal of Physics: Condensed Matter* 27.47 (2015), p. 473002.

[43] J.K. Nielsen et al. “Elongational viscosity of monodisperse and bidisperse polystyrene melts”. In: *Journal of Rheology* 50.4 (2006), pp. 453–476.

[44] R. Kimmich. “Entanglement and confinement effects constraining polymer chain dynamics on different length and time scales”. In: *Comptes Rendus Physique* 11.2 (2010), pp. 149–159.

[45] P.S. Stephanou, I.Ch. Tsimouri, and V.G. Mavrantzas. “Flow-Induced Orientation and Stretching of Entangled Polymers in the Framework of Nonequilibrium Thermodynamics”. In: *Macromolecules* 49.8 (2016), pp. 3161–3173.

[46] C. Tzoumanekas and D.N. Theodorou. “Topological analysis of linear polymer melts: a statistical approach”. In: *Macromolecules* 39.13 (2006), pp. 4592–4604.

[47] R.S. Hoy, K. Foteinopoulou, and M. Kröger. “Topological analysis of polymeric melts: Chain-length effects and fast-converging estimators for entanglement length”. In: *Physical Review E* 80.3 (2009), p. 031803.

[48] D.M. Sussman and K.S. Schweizer. “Entangled polymer chain melts: Orientation and deformation dependent tube confinement and interchain entanglement elasticity”. In: *The Journal of Chemical Physics* 139.23 (2013), p. 234904.

[49] J. Des Cloizeaux. “Polymer melts: a theoretical justification of double reptation”. In: *Journal de Physique I* 3.1 (1993), pp. 61–68.

[50] G. Szamel. “Reptation as a dynamic mean-field theory: Study of a simple model of rodlike polymers”. In: *Physical Review Letters* 70.24 (1993), p. 3744.

[51] M.G. Guenza. “Microscopic Theory for the Dynamics of Unentangled and Entangled Polymer Melts”. In: *arXiv preprint arXiv:1509.08532* (2015).

[52] M. Doi. “Explanation for the 3.4 power law of viscosity of polymeric liquids on the basis of the tube model”. In: *Journal Of Polymer Science Part C-Polymer Letters* 19.5 (1981), pp. 265–273.

[53] W.W. Graessley. “Some phenomenological consequences of the Doi–Edwards theory of viscoelasticity”. In: *Journal of Polymer Science: Polymer Physics Edition* 18.1 (1980), pp. 27–34.

[54] K. Osaki and M. Kurata. “Experimental appraisal of the Doi-Edwards theory for polymer rheology based on the data for polystyrene solutions”. In: *Macromolecules* 13.3 (1980), pp. 671–676.

[55] Q. Huang et al. “Bridging the gap between polymer melts and solutions in extensional rheology”. In: *Macromolecules* 48.12 (2015), pp. 4158–4163.

[56] H.K. Rasmussen. “A constitutive analysis of the extensional flows of nearly monodisperse polyisoprene melts”. In: *Polymer* (2016).

[57] S.T. Milner and T.C.B. McLeish. “Reptation and contour-length fluctuations in melts of linear polymers”. In: *Physical Review Letters* 81.3 (1998), p. 725.

[58] S. Costanzo et al. “Shear and Extensional Rheology of Polystyrene Melts and Solutions with the Same Number of Entanglements”. In: *Macromolecules* (2016).

[59] T.C.B. McLeish. “Why, and when, does dynamic tube dilation work for stars?” In: *Journal of Rheology* 47.1 (2003), pp. 177–198.

[60] J. Cao and Z. Wang. “Microscopic Picture of Constraint Release Effects in Entangled Star Polymer Melts”. In: *Macromolecules* 49.15 (2016), pp. 5677–5691.

[61] S.T. Milner, T.C.B. McLeish, and A.E. Likhtman. “Microscopic theory of convective constraint release”. In: *Journal of Rheology* 45.2 (2001), pp. 539–563.

[62] D. Auhl et al. “Linear and nonlinear shear flow behavior of monodisperse polyisoprene melts with a large range of molecular weights”. In: *Journal of Rheology* 52.3 (2008), pp. 801–835.

[63] D. Vlassopoulos. “Macromolecular topology and rheology: beyond the tube model”. In: *Rheologica Acta* 55.8 (2016), pp. 613–632.

[64] G. Ianniruberto. “Quantitative appraisal of a new CCR model for entangled linear polymers”. In: *Journal of Rheology* 59.1 (2015), pp. 211–235.

[65] A.K. Tezel et al. “The nonlinear response of entangled star polymers to startup of shear flow”. In: *Journal of Rheology* 53.5 (2009), pp. 1193–1214.

[66] K.A. Carter, J.M. Girkin, and S.M. Fielding. “Shear banding in large amplitude oscillatory shear (LAOStrain and LAOStress) of polymers and wormlike micelles”. In: *Journal of Rheology* 60.5 (2016), pp. 883–904.

[67] D.W. Mead, R.G. Larson, and M. Doi. “A molecular theory for fast flows of entangled polymers”. In: *Macromolecules* 31.22 (1998), pp. 7895–7914.

[68] G. Ianniruberto and G. Marrucci. “A simple constitutive equation for entangled polymers with chain stretch”. In: *Journal of Rheology* 45.6 (2001), pp. 1305–1318.

[69] R.J.A. Steenbakkers and J.D. Schieber. “Derivation of free energy expressions for tube models from coarse-grained slip-link models”. In: *The Journal of chemical physics* 137.3 (2012), p. 034901.

[70] M.W. Collis et al. “Constriction flows of monodisperse linear entangled polymers: Multiscale modeling and flow visualization”. In: *Journal of Rheology* 49.2 (2005), pp. 501–522.

[71] J. Bent et al. “Neutron-mapping polymer flow: scattering, flow visualization, and molecular theory”. In: *Science* 301.5640 (2003), pp. 1691–1695.

[72] R.S. Graham et al. “Measuring and predicting the dynamics of linear monodisperse entangled polymers in rapid flow through an abrupt contraction. A small angle neutron scattering study”. In: *Macromolecules* 39.7 (2006), pp. 2700–2709.

[73] A. Blanchard et al. “Small-angle neutron scattering observation of chain retraction after a large step deformation”. In: *Physical Review Letters* 95.16 (2005), p. 166001.

[74] M.J. Hamer, J.A.D. Wattis, and R.S. Graham. “Analytic calculation of nucleation rates from a kinetic Monte Carlo simulation of flow induced crystallization in polymers”. In: *Journal of Non-Newtonian Fluid Mechanics* 165.19 (2010), pp. 1294–1301.

[75] R.S. Graham et al. “The long-chain dynamics in a model homopolymer blend under strong flow: Small-angle neutron scattering and theory”. In: *Soft Matter* 5.12 (2009), pp. 2383–2389.

[76] F. Snijkers et al. “Viscoelasticity and nonlinear simple shear flow behavior of an entangled asymmetric exact comb polymer solution”. In: *Journal of Rheology* 60.3 (2016), pp. 451–463.

[77] M. Andreev et al. “Approximations of the discrete slip-link model and their effect on nonlinear rheology predictions”. In: *Journal of Rheology* 57.2 (2013), pp. 535–557.

[78] P.E. Boukany and S.-Q. Wang. “Exploring origins of interfacial yielding and wall slip in entangled linear melts during shear or after shear cessation”. In: *Macromolecules* 42.6 (2009), pp. 2222–2228.

[79] P.E. Boukany, S.-Q. Wang, et al. “Shear banding or not in entangled DNA solutions”. In: *Macromolecules* 43.17 (2010), p. 6950.

[80] S. Cheng and S.-Q. Wang. “Is shear banding a metastable property of well-entangled polymer solutions?” In: *Journal of Rheology* 56.6 (2012), pp. 1413–1428.

[81] S.-Q. Wang et al. “New experiments for improved theoretical description of nonlinear rheology of entangled polymers”. In: *Macromolecules* 46.8 (2013), pp. 3147–3159.

[82] Y. Wang and S.-Q. Wang. “From elastic deformation to terminal flow of a monodisperse entangled melt in uniaxial extension”. In: *Journal of Rheology* 52.6 (2008), pp. 1275–1290.

[83] S.-Q. Wang. “Nonlinear rheology of entangled polymers at turning point”. In: *Soft matter* 11.8 (2015), pp. 1454–1458.

[84] R.L. Moorcroft and S.M. Fielding. “Shear banding in time-dependent flows of polymers and wormlike micelles”. In: *Journal of Rheology* 58.1 (2014), pp. 103–147.

[85] Y. Masubuchi and H. Watanabe. “Origin of stress overshoot under start-up shear in primitive chain network simulation”. In: *ACS Macro Letters* 3.11 (2014), pp. 1183–1186.

[86] Y. Zhao. “Facile Synthesis of Multicomponent Star Copolymers via Controlled Polymerization and Click Chemistry”. In: *Miktoarm Star Polymers: From Basics of Branched Architecture to Synthesis, Self-Assembly and Applications*. 2017, pp. 56–89.

[87] J.-S. Wang and K. Matyjaszewski. “Controlled/” living” radical polymerization. Atom transfer radical polymerization in the presence of transition-metal complexes”. In: *Journal of the American Chemical Society* 117.20 (1995), pp. 5614–5615.

[88] K. Matyjaszewski and J. Xia. “Atom transfer radical polymerization”. In: *Chemical reviews* 101.9 (2001), pp. 2921–2990.

[89] M. Kato et al. “Polymerization of methyl methacrylate with the carbon tetrachloride/dichlorotris-(triphenylphosphine) ruthenium (II)/methylaluminum bis(2,6-di-tert-butylphenoxide) initiating system: possibility of living radical polymerization”. In: *Macromolecules* 28.5 (1995), pp. 1721–1723.

[90] M. Kamigaito, T. Ando, and M. Sawamoto. “Metal-catalyzed living radical polymerization”. In: *Chemical Reviews* 101.12 (2001), pp. 3689–3746.

[91] M.K. Georges et al. “Narrow molecular weight resins by a free-radical polymerization process”. In: *Macromolecules* 26.11 (1993), pp. 2987–2988.

[92] C. J Hawker, A. W Bosman, and E. Harth. “New polymer synthesis by nitroxide mediated living radical polymerizations”. In: *Chemical reviews* 101.12 (2001), pp. 3661–3688.

[93] J. Chiefari et al. “Living free-radical polymerization by reversible addition- fragmentation chain transfer: the RAFT process”. In: *Macromolecules* 31.16 (1998), pp. 5559–5562.

[94] G. Moad, E. Rizzardo, and S.H. Thang. “Living radical polymerization by the RAFT process–a second update”. In: *Australian journal of chemistry* 62.11 (2009), pp. 1402–1472.

[95] S. Perrier and P. Takolpuckdee. “Macromolecular design via reversible addition–fragmentation chain transfer (RAFT)/xanthates (MADIX) polymerization”. In: *Journal of Polymer Science Part A: Polymer Chemistry* 43.22 (2005), pp. 5347–5393.

[96] C. Barner-Kowollik and S. Perrier. “The future of reversible addition fragmentation chain transfer polymerization”. In: *Journal of Polymer Science Part A: Polymer Chemistry* 46.17 (2008), pp. 5715–5723.

[97] J.R. Schaefgen and P.J. Flory. “Synthesis of multichain polymers and investigation of their viscosities”. In: *Journal of the American Chemical Society* 70.8 (1948), pp. 2709–2718.

[98] H. Liu et al. “Synthesis and properties of couplable ABCDE star copolymers by orthogonal CuAAC and Diels–Alder click reactions”. In: *Polymer Chemistry* 7.8 (2016), pp. 1603–1611.

[99] Q. Fu et al. “One-pot preparation of 3-miktoarm star terpolymers via “click chemistry” and atom transfer nitroxide radical coupling reaction”. In: *Journal of Polymer Science Part A: Polymer Chemistry* 47.3 (2009), pp. 986–990.

[100] O. Altintas, G. Hizal, and U. Tunca. “ABC-type hetero-arm star terpolymers through “Click” chemistry”. In: *Journal of Polymer Science Part A: Polymer Chemistry* 44.19 (2006), pp. 5699–5707.

[101] J. Roovers, P. Toporowski, and J. Martin. “Synthesis and characterization of multiarm star polybutadienes”. In: *Macromolecules* 22.4 (1989), pp. 1897–1903.

[102] I.M. Khan et al. “Synthesis of three-arm poly (styrene-arm-styrene-arm-2-vinylpyridine) star copolymers”. In: *Macromolecules* 25.11 (1992), pp. 3002–3004.

[103] Huynh-Ba-Gia, R. Jerome, and Ph. Teyssié. “Starshaped block copolymers. I. Synthesis of new A (B) 2 starshaped block copolymers based on vinyl or diene hydrocarbons (A) and oxirane (B)”. In: *Journal of Polymer Science Part A: Polymer Chemistry* 18.12 (1980), pp. 3483–3498.

[104] X. Wu and C.L. Fraser. “Architectural diversity via metal template-assisted polymer synthesis: a macroligand chelation approach to linear and star-shaped polymeric ruthenium tris (bipyridine) complexes”. In: *Macromolecules* 33.11 (2000), pp. 4053–4060.

[105] D. Decker and P. Rempp. “Preparation de Composes Macromoleculaires a Structure en Etoile”. In: *Comptes Rendus Hebdomadaires des Seances de l Academie des Sciences* 261.9 (1965), p. 1977.

[106] A. Yamagishi et al. “Spectroscopic and Kinetic Studies of Addition of Double 1,1-Diphenylethylenes to Lithium Polystyryl in Benzene”. In: *Macromolecules* 11.3 (1978), pp. 607–615.

[107] M. Morton et al. “Preparation and properties of monodisperse branched polystyrene”. In: *Journal of Polymer Science Part A: Polymer Chemistry* 57.165 (1962), pp. 471–482.

[108] G. Velis and N. Hadjichristidis. “Synthesis of model PS (PI) 5 and (PI) 5PS (PI) 5 nonlinear block copolymers of styrene (S) and isoprene (I)”. In: *Macromolecules* 32.2 (1999), pp. 534–536.

[109] A. Avgeropoulos et al. “Synthesis of Model 16-Miktoarm (Verginat) Star Copolymers of the A8B8 Type”. In: *Macromolecules* 29.18 (1996), pp. 6076–6078.

[110] J. Roovers. “Concentration dependence of the relative viscosity of star polymers”. In: *Macromolecules* 27.19 (1994), pp. 5359–5364.

[111] H. Iatrou et al. “Miktoarm Star (μ-Star) Polymers: A Successful Story”. In: *Miktoarm Star Polymers: From Basics of Branched Architecture to Synthesis, Self-Assembly and Applications*. 2017.

[112] T.A. Orofino and F. Wenger. “Dilute Solution Properties of Branched Polymers. Polystyrene Trifunctional Star Molecules”. In: *The Journal of Physical Chemistry* 67.3 (1963), pp. 566–575.

[113] R. Mayer. “Organized structures in amorphous styrene/cis-1, 4-isoprene block copolymers: low angle X-ray scattering and electron microscopy”. In: *Polymer* 15.3 (1974), pp. 137–145.

[114] J.A. Gervasi and A.B. Gosnell. “Synthesis and characterization of branched polystyrene. Part I. Synthesis of four-and six-branch star polystyrene”. In: *Journal of Polymer Science Part A: Polymer Chemistry* 4.6 (1966), pp. 1391–1399.

[115] A.B. Gosnell, J.A. Gervasi, and A. Schindler. “Synthesis and characterization of branched polystyrene. Part II. Fractionation”. In: *Journal of Polymer Science Part A: Polymer Chemistry* 4.6 (1966), pp. 1401–1412.

[116] J. Herz, M. Hert, and C. Strazielle. “Synthèse et caractérisation de polystyrènes en étoile à trois branches”. In: *Macromolecular Chemistry and Physics* 160.1 (1972), pp. 213–225.

[117] Cl Strazielle and J Herz. “Synthesis and Physical-Chemistry of Branched Star-Shaped and Comb-Like Polystyrenes”. In: *European Polymer Journal* 13.3 (1977), pp. 223–233.

[118] C.A. Uraneck and J.N. Short. “Solution-polymerized rubbers with superior breakdown properties”. In: *Journal of Applied Polymer Science* 14.6 (1970), pp. 1421–1432.

[119] H.L. Hsieh. “Synthesis of radial thermoplastic elastomers”. In: *Rubber Chemistry and Technology* 49.5 (1976), pp. 1305–1310.

[120] S. Ito et al. “Precise Synthesis of Multi-Component Miktoarm Star Polymers by a New Conceptual Iterative Methodology Using Living Anionic Polymerization”. In: *Miktoarm Star Polymers: From Basics of Branched Architecture to Synthesis, Self-Assembly and Applications*. 2017, pp. 31–55.

[121] T. Higashihara et al. “Successive synthesis of well-defined star-branched polymers by an iterative approach based on living anionic polymerization”. In: *Macromolecular Research* 14.3 (2006), pp. 287–299.

[122] A. Hirao, M. Hayashi, and T. Higashihara. “Synthesis of Branched Polymers by Means of Living Anionic Polymerization, 8. Synthesis of Well-Defined Star-Branched Polymers by an Iterative Approach Based on Living Anionic Polymerization Using 1,1-Diphenylethylene Derivatives”. In: *Macromolecular Chemistry and Physics* 202.16 (2001), pp. 3165–3173.

[123] A. Hirao and T. Higashihara. “Synthesis of branched polymers by means of living anionic polymerization. 13. Synthesis of well-defined star-branched polymers via an iterative approach using living anionic polymers”. In: *Macromolecules* 35.19 (2002), pp. 7238–7245.

[124] A. Hirao et al. “Successive synthesis of well-defined many arm star-branched polymers by an iterative methodology using a specially designed 1, 1-diphenylethylene”. In: *Macromolecules* 39.18 (2006), pp. 6081–6091.

[125] A. Hirao, T. Higashihara, and K. Inoue. “Successive synthesis of well-defined asymmetric star-branched polymers up to seven-arm, seven-component ABCDEFG type by an iterative methodology based on living anionic polymerization”. In: *Macromolecules* 41.10 (2008), pp. 3579–3587.

[126] K. Sugiyama et al. “Synthesis of well-defined block copolymers and star-branched polymers by using terminal 1, 3-butadiene functionalized polymers as reactive building blocks”. In: *Reactive and Functional Polymers* 69.7 (2009), pp. 480–492.

[127] K. Sugiyama et al. “Synthesis of well-defined (AB)n multiblock copolymers composed of polystyrene and poly(methylmethacrylate) segments using specially designed living AB diblock copolymer anion”. In: *Macromolecules* 43.3 (2010), pp. 1403–1410.

[128] S. Ito et al. “Precise synthesis of miktoarm star polymers by using a new dual-functionalized 1,1-diphenylethylene derivative in conjunction with living anionic polymerization system”. In: *Macromolecules* 45.12 (2012), pp. 4997–5011.

[129] S. Ito et al. “Successive synthesis of miktoarm star polymers having up to seven arms by a new iterative methodology based on living anionic polymerization using a trifunctional lithium reagent”. In: *Macromolecules* 46.3 (2013), pp. 819–827.

[130] R. Goseki et al. “Precise synthesis of poly (methacrylate)–based miktoarm star polymers by a new stepwise iterative methodology using a formyl-functionalized 1,1-diphenylethylene derivative”. In: *Polymer* 54.8 (2013), pp. 2049–2057.

[131] Y. Zhao et al. “Synthesis of functionalized asymmetric star polymers containing conductive polyacetylene segments by living anionic polymerization”. In: *Journal of the American Chemical Society* 127.41 (2005), pp. 14158–14159.

[132] H. Gilman and F.K. Cartledge. “The Analysis of Organolithium Compounds”. In: *Journal of Organometallic Chemistry* 2.6 (1964), pp. 447–454.

[133] M.F. Lipton et al. “A convenient method for the accurate estimation of concentrations of alkyllithium reagents”. In: *Journal of Organometallic Chemistry* 186.2 (1980), pp. 155–158.

[134] S.C. Watson and J.F. Eastham. “Colored indicators for simple direct titration of magnesium and lithium reagents”. In: *Journal of Organometallic Chemistry* 9.1 (1967), pp. 165–168.

[135] R.A. Ellison, R. Griffin, and F.N. Kotsonis. “A method for accurate titration of alkyllithium reagents in ether solutions”. In: *Journal of Organometallic Chemistry* 36.2 (1972), pp. 209–213.

[136] D. Braun et al. “Synthesis of Macromolecules by Chain Growth Polymerization”. In: *Polymer Synthesis: Theory and Practice*. 2013, pp. 149–258.

[137] S. Ndoni et al. “Laboratory-scale setup for anionic polymerization under inert atmosphere”. In: *Review of Scientific Instruments* 66.2 (1995), pp. 1090–1095.

[138] K. Tamao. “Discovery and synthetic applications of novel silicon-carbon bond cleavage reactions based on the coordination number change of organosilicon compounds”. In: *Proceedings of the Japan Academy Series B* 84.5 (2008), pp. 123–133.

[139] T. Chang. “Polymer characterization by interaction chromatography”. In: *Journal of Polymer Science Part B: Polymer Physics* 43.13 (2005), pp. 1591–1607.

[140] J.K. Nielsen et al. “Nonlinear Branch-Point Dynamics of Multiarm Polystyrene”. In: *Macromolecules* 39.25 (2006), pp. 8844–8853.

[141] S. Agostini and L.R. Hutchings. “Synthesis and temperature gradient interaction chromatography of model asymmetric star polymers by the “macromonomer” approach”. In: *European Polymer Journal* 49.9 (2013), pp. 2769–2784.

[142] D.M. Knauss and T. Huang. “Star-block-Linear-block-Star Triblock (Pom-Pom) Polystyrene by Convergent Living Anionic Polymerization”. In: *Macromolecules* 35.6 (2002), pp. 2055–2062.

[143] A. Bach et al. “Elongational Viscosity of Narrow Molar Mass Distribution Polystyrene”. In: *Macromolecules* 36.14 (2003), pp. 5174–5179.

[144] B. Lepoittevin et al. “Synthesis and Characterization of Ring-Shaped Polystyrenes”. In: *Macromolecules* 33.22 (2000), pp. 8218–8224.

[145] D.C. Schriemer and L. Li. “Mass Discrimination in the Analysis of Polydisperse Polymers by MALDI Time-of-Flight Mass Spectrometry. 1. Sample Preparation and Desorption/Ionization Issues”. In: *Analytical Chemistry* 69.20 (1997), pp. 4169–4175.

[146] G. Montaudo and E. Scamporrino. “Novel Procedure for Molecular Weight Averages Measurement of Polydisperse Polymers Directly”. In: *Rapid communications in mass spectrometry* 10 (1996), pp. 1551–1559.

[147] H. Munstedt. “New universal extensional rheometer for polymer melts. Measurements on a polystyrene sample”. In: *Journal of Rheology* 23.4 (1979), pp. 421–436.

[148] J. Meissner and J. Hostettler. “A new elongational rheometer for polymer melts and other highly viscoelastic liquids”. In: *Rheologica Acta* 33.1 (1994), pp. 1–21.

[149] T. Sridhar et al. “Measurement of extensional viscosity of polymer solutions”. In: *Journal of non-newtonian fluid mechanics* 40.3 (1991), pp. 271–280.

[150] M.L. Sentmanat. “Miniature universal testing platform: from extensional melt rheology to solid-state deformation behavior”. In: *Rheologica Acta* 43.6 (2004), pp. 657–669.

[151] J.M.R. Marin et al. “A control scheme for filament stretching rheometers with application to polymer melts”. In: *Journal of Non-Newtonian Fluid Mechanics* 194 (2013), pp. 14–22.

[152] M.I. Kolte, H.K. Rasmussen, and O. Hassager. “Transient filament stretching rheometer”. In: *Rheologica Acta* 36.3 (1997), pp. 285–302.

[153] S.H. Spiegelberg, D.C. Ables, and G.H. McKinley. “The role of end-effects on measurements of extensional viscosity in filament stretching rheometers”. In: *Journal of Non-Newtonian Fluid Mechanics* 64.2 (1996), pp. 229–267.

[154] L. Hengeller. “Entangled Polymer Melts in Extensional Flow”. PhD thesis. 2016.

[155] A. Bach, H.K. Rasmussen, and O. Hassager. “Extensional viscosity for polymer melts measured in the filament stretching rheometer”. In: *Journal of Rheology* 47.2 (2003), pp. 429–441.

[156] *Fast Active Control Scheme of the Filament Stretching Rheometer*. URL: http://www.rheofilament.com/filament_stretching_rheometer.html (visited on 03/14/2017).

[157] Q. Huang. "Molecular Rheology of Complex Fluids". PhD thesis. 2013.

[158] P. Szabo. "Transient filament stretching rheometer". In: *Rheologica Acta* 36.3 (1997), pp. 277–284.

[159] H.K. Rasmussen et al. "Experimental evaluation of the pure configurational stress assumption in the flow dynamics of entangled polymer melts". In: *Journal of Rheology* 54.6 (2010), pp. 1325–1336.

[160] Y. Wang et al. "Elastic breakup in uniaxial extension of entangled polymer melts". In: *Physical Review Letters* 99.23 (2007), p. 237801.

[161] A. Lyhne, H.K. Rasmussen, and O. Hassager. "Simulation of elastic rupture in extension of entangled monodisperse polymer melts". In: *Physical Review Letters* 102.13 (2009), p. 138301.

[162] J.J.K. Kirkensgaard et al. "Nematic effects and strain coupling in entangled polymer melts under strong flow". In: *Physical Review E* 94.2 (2016), p. 020502.

[163] R. W. Pennisi and L. J. Fetters. "Preparation of asymmetric 3-arm polybutadiene and polystyrene stars". In: *Macromolecules* 21 (1988), pp. 1094–1099.

[164] H. Fritzsche, J. Huot, and D. Fruchart. *Neutron Scattering and Other Nuclear Techniques for Hydrogen in Materials*. 2016.

[165] L. de Broglie. "Thèse de Doctorat". In: *Phil. Mag.* 47 (1924).

[166] A. Guinier. "Arrangement for obtaining intense diffraction diagrams of crystalline powders with monochromatic radiation". In: *Compt. Rend* 204 (1937), pp. 1114–1116.

[167] A. Guinier. "La diffraction des rayons X aux tres petits angles: applications a l'etude de phenomenes ultramicroscopiques". In: *Ann. phys.* 12 (1939), p. 161.

[168] A. Guinier. "Détermination de la taille des particules submicroscopiques par les rayons X". In: *J. chim. phys.* 40 (1943), p. 133.

[169] *Guinier Approximation Derivation*. URL: http://research.kek.jp/people/seto/sas/sas.4.2.html (visited on 03/14/2017).

[170] G. Kostorz. "Small-Angle Scattering and Its Applications to Materials Science". In: *Neutron Scattering: Treatise on Materials Science and Technology* 15 (2013), p. 227.

[171] V.F. Sears. "Neutron scattering lengths and cross sections". In: *Neutron News* 3.3 (1992), pp. 26–37.

[172] G. Porod. "Die Roentgenkleinwinkelstreuung von dichtgepackten kolloiden Systemen". In: *Kolloid-Zeitschrift* 124.2 (1951), pp. 83–114.

[173] G. Porod. "Die Roentgenkleinwinkelstreuung von dichtgepackten kolloiden Systemen". In: *Kolloid-Zeitschrift* 125.1 (1952), pp. 51–57.

[174] G Porod. "Die Roentgenkleinwinkelstreuung von dichtgepackten kolloiden Systemen. ii. teil". In: *Kolloid-Zeitschrift* 125.2 (1952), pp. 108–122.

[175] S. Ciccariello, J. Goodisman, and H. Brumberger. "On the Porod law". In: *Journal of Applied Crystallography* 21.2 (1988), pp. 117–128.

[176] *Standard Plots*. URL: https://www.ncnr.nist.gov/staff/hammouda/distance_learning/chapter_22.pdf (visited on 03/14/2017).

[177] R.S. Stein, P.R. Wilson, and S.N. Stidham. “Scattering of light by heterogeneous spheres”. In: *Journal of Applied Physics* 34.1 (1963), pp. 46–50.

[178] G.D. Wignall and F.S. Bates. “Applications and limitations of deuterium labeling methods to neutron scattering studies of polymers”. In: *Makromolekulare Chemie. Macromolecular Symposia*. Vol. 15. 1. Wiley Online Library. 1988, pp. 105–122.

[179] F.S. Bates, G.D. Wignall, and W.C. Koehler. “Critical behavior of binary liquid mixtures of deuterated and protonated polymers”. In: *Physical Review Letters* 55.22 (1985), p. 2425.

[180] F.S. Bates and G.D. Wignall. “Non-ideal mixing in binary blends of perdeuterated and protonated polystyrenes”. In: *Macromolecules* 19.3 (1986), pp. 932–934.

[181] F.S. Bates and P. Wiltzius. “Spinodal decomposition of a symmetric critical mixture of deuterated and protonated polymer”. In: *The Journal of Chemical Physics* 91.5 (1989), pp. 3258–3274.

[182] W.W. Graessley et al. “Effect of Deuterium Substitution on Thermodynamic Interactions in Polymer Blends”. In: *Macromolecules* 26.5 (1993), pp. 1137–1143.

[183] C. Qian, S.J. Mumby, and B.E. Eichinger. “Phase diagrams of binary polymer solutions and blends”. In: *Macromolecules* 24.7 (1991), pp. 1655–1661.

[184] H. Yang et al. “Deuteration Effects on the Miscibility and Phase Separation Kinetics of Polymer Blends”. In: *Macromolecules* 19.6 (1986), pp. 1667–1674.

[185] F.S. Bates and G.H. Fredrickson. “Block Copolymer Thermodynamics: Theory and Experiment”. In: *Annual Review of Physical Chemistry* 41.1 (1990), pp. 525–557.

[186] B. Hammouda, B.J. Bauer, and T.P. Russell. “Small-Angle Neutron Scattering from Deuterated Polystyrene/Poly(butylmethacrylate) Homopolymer Blend Mixtures”. In: *Macromolecules* 27.8 (1994), pp. 2357–2359.

[187] H. Hasegawa et al. “SANS and SAXS Studies on Molecular Conformation of a Block Polymer in Microdomain Space”. In: *Macromolecules* 18.1 (1985), pp. 67–78.

[188] F.S. Bates. “Polymer-Polymer Phase Behavior”. In: *Science* 251.4996 (1991), pp. 898–905.

[189] P.-G. De Gennes. *Scaling Concepts in Polymer Physics*. 1979.

[190] J.H. Hildebrand and R.L. Scott. *Regular Solutions*. 1962.

[191] J. Kohlbrecher and W. Wagner. “The new SANS instrument at the Swiss spallation source SINQ”. In: *Journal of Applied Crystallography* 33.3 Part 1 (2000), pp. 804–806.

[192] E.P. Gilbert, J.C. Schulz, and T.J. Noakes. “‘Quokka’ - the small-angle neutron scattering instrument at OPAL”. In: *Physica B: Condensed Matter* 385–386, Part 2 (2006). Proceedings of the Eighth International Conference on Neutron Scattering, pp. 1180–1182.

[193] *QUOKKA - Small-Angle Neutron Scattering*. URL: http://www.ansto.gov.au/ResearchHub/Bragg/Facilities/Instruments/Quokka/index.htm (visited on 03/14/2017).

[194] *SANS-I: Small Angle Neutron Scattering Instrument*. URL: https://www.psi.ch/sinq/sansi/sans-i (visited on 03/14/2017).

[195] *The main components of the SANS-I*. URL: https://www.psi.ch/sinq/sansi/ComponentsEN/igp_9ed4a8cf587649830e60b255ea3961d2_s_sansan.gif (visited on 03/14/2017).

[196] S.R. Kline. “Reduction and analysis of SANS and USANS data using IGOR Pro”. In: *Journal of Applied Crystallography* 39.6 (2006), pp. 895–900.

[197] J.S. Pedersen. “Modelling of Small-Angle Scattering Data from Colloids and Polymer Systems”. In: *Neutron, X-rays and Light. Scattering Methods Applied to Soft Condensed Matter*. Ed. by P. Lindner and T. Zemb. 2002. Chap. 16, pp. 391–420.

[198] P. Debye. “Molecular-weight Determination by Light Scattering.” In: *The Journal of Physical and Colloid Chemistry* 51.1 (1947), pp. 18–32.

[199] O. Hassager et al. “Stress and neutron scattering measurements on linear polymer melts undergoing steady elongational flow”. In: *Rheologica Acta* 51.5 (2012), pp. 385–394.

[200] M. Warner and S.F. Edwards. “Neutron scattering from strained polymer networks”. In: *Journal of Physics A: Mathematical and General* 11.8 (1978), p. 1649.

[201] J. D’Errico. *Bound Constrained Optimization Using fminsearch*. URL: http://www.mathworks.com/matlabcentral/fileexchange/8277-fminsearchbnd--fminsearchcon (visited on 03/14/2017).

[202] H. Benoit. “On the effect of branching and polydispersity on the angular distribution of the light scattered by gaussian coils”. In: *Journal of Polymer Science* 11.5 (1953), pp. 507–510.

[203] W. Burchard. “Statistics of Star-Shaped Molecules. I. Stars with Polydisperse Side Chains”. In: *Macromolecules* 7.6 (1974), pp. 835–841.

APPENDIX A

Model Polystyrene Symmetric 3-Arm Star Synthesis for Rheological Studies

Model Polyester Dendrimers: A New Class of Synthetic Scaffolds for Tissue Engineering Studies.

Andrzej Stasiński, Anna-Elin Hinsta*

*Corresponding Author
A. Stasiński, Prof. A. Hinsta
Department of Micro- and Nanotechnology
Polytechnicum, Building 423
DK-2800 Kgs. Lyngby
Denmark
Tel: +45 45258000
E-mail: hinsta@nanotech.dtu.dk

We present an easy synthesis of high molecular weight polyester dendrimers by means of polycondensation techniques that are suitable for macromolecular chemistry studies. The synthesis is done avoiding the step of converting polyester-hydroxyl-terminated dendrimers into polyester-chloride-terminated dendrimers. We show that if a short oligomeric block is present then the resulting new polymers are prone to degradation at the methylene group during typical chemotherapeutic environments, such as fibrinolytic enriching. Samples are characterized using size exclusion chromatography (SEC).

Research highlights:

- The solubility of macromolecular chain depends highly on the chemistry of the core.
- Monodisperse nanometric blocks within a polymer degrade during macromolecular chemistry studies.
- Nanometre-polydispersity low molecular weight blocks of PPP can be made at -60°C.

Keywords: Aromatic Polycondensation, New Polymers, Polymer synthesis, Fibrinolytic Enriching, Chemotherapy

1. Introduction

The star is a specific macromolecular architecture of polymers, in which several linear polymers are linked together by use of their ends to a common center, creating a structure which is particularly interesting because it allows an almost continuous change of properties from that of a flexible linear polymer to a spherical colloidal particle with very soft pair interactions [1]. Star-shaped polymers also attract significant attention because of their unique rheological properties [2].

In general, star polymers are synthesized with the use of multifunctional coupling agents, such as chlorosilane compounds [3], divinylbenzene [4], derivatives of diphenylethylene [5], (halogenomethyl)benzenes [6-7] or others. For the case of chlorosilane compounds, it is well established, that the perpetuities of the high molecular weight polystyrene stars favor the inability of polystyryllithium to undergo complete conversion with a stoichiometric quantity of chlorosilanes containing three chlorines per silicone atom[3]. According to Rempp and Franta [3], complete conversion of living anions to 3-arm stars is because with polar additives to minimize the aggregation of the anions is feasible to the molecular mass range up to 40 kg/mol. The lack of reactivity for the case of higher molecular weight stars can be avoided by converting the styryllithium-carry to the hexadienyllithium[8-9], which can react with the stoichiometric amounts of trichlorosilanes [10]. On the other hand, the rich levels in chloro reactive linkers near the core of a polymer star, cause the double bond in the oligobutadiene unit can be easily attacked by sulfuric or ions, which is critical for the case of end-terminal ideology studies, where temperatures vary over (70°C. Star polymers with silicon core that "leave arms" during a Fluorine cleaving, recovery experiments have been previously reported [11].

In this paper we present an easy synthesis providing the use of oligobutadiene linker to obtain symmetric polystyrene stars of high molecular weight suitable for light-scattering studies.

2. Experimental Section

2.1. Synthesis and chromatography

All linear polymer blocks were synthesized with the use of the method of living anionic polymerization according to the standard procedure by Nilson et al. [12]. Reactions were carried out in freshly distilled tetrahydrofuran (THF). A titrated solution of sec-butyllithium in benzene was used as the initiator. The synthesis proceeded of two stages: first, linear polystyrene

growth started at -50°C (with the use of a cooling THF bath) and was left to warm up to -78°C, giving a narrow polydispersity for the low molecular weight PEO-block in THF. This stage took one hour. The star formation stage at -78°C with methylmethacrylate as the monomer took 24 hours. The means of living anions used to avoid doubling of molecular weight by the formation of "1-atom stars") was accomplished with a degassed 10% solution of ACOH in dH2O. The resulting polymer solution was then harvested.

The molar mass of the samples was determined with size exclusion chromatography (SEC) with non-stabilized THF as the eluent and tetrahydrofuran (2%) as co-additive to the eluent. The columns are consisted of a 5µm guard column and two 300×8 mm² columns (PLgel Mixed-C and Mixed-D). The system was equipped with a triple detection system as combined Viscotek model 250 differential refractive index (DRI) and a differential viscosity detector plus a Viscotek model 270 dual right-angle laser light scattering detector (RALLS). On the basis of calibration with narrow molar mass polystyrene standards and flow rate signal adjusted according to internal standard (signals: DRI) signals, the values of the weight-average molecular weight (M_w) and the polydispersity index (PDI) were determined.

2.2. Film formation

Polymer thermoanalysis was done with volume of the solvent and because of the non-uniformity. Samples needed several thermoanalysis, with the last Glass thermoanalysis from a 2.5% solution. Typically, a polymer was dissolved in toluene and, while stirring, the solvent of non-solvent was added until the solution was turbid. Then the solution was heated in order to dissolve the precipitate and left to slowly cool down giving the separated phases, which were collected.

2.3. Environmental Microscopy

The molecular micro measurements were done with the use of Electron switching Secondary (ESM). The samples were first washed in cyclohexane dropped discs for 24 minutes at 150°C under vacuum. Then, during 30 minutes the samples were pre-stretched at 180°C, allowed to cool down to 130°C and stretched at a Peltier micro star 3. The procedure followed a well-established algorithm by Hwang [11].

3. Results and Discussion

Five polystyrene star samples made of either styrene or styrene/styrene-dT with or without baseline holder were synthesized.

Table 1 summarizes the weight-average molecular weight and the polydispersity indexes of the samples.

Sample	M_w, kg/mol	PDI	% of styrene-dT
P-S0	251	1.1	0
P-S5-dbu-I-P-S5-dbu-I	309	1.3	~0.1
P-S5-dbu-I-P5-dbu-I	136	1.1	0
P-S5-P-S5	301	1.1	~10^{-3}

Table 1.

Higher PDI for the case of block copolymer is due to a concentration gradient during the addition of second monomer which led to a insertion rate gradient and hence higher polydispersity. Extensive reactivity of polystyryllithium in ethereal solvents favors the coupling reaction for a star formation, but on the other hand, causes an increase of polydispersity if any heterogeneity in the concentration of monomer in solution is present due to an inefficient mixing.

The use of deuterated and protonated styrene monomers is established by the further small-angle scattering experiments to unravel molecular orientations and stretching of key segments during the flow.

4. Polymer Degradation During the Extensional Rheology Studies

The rational investigation of polymers with the use of FOR is a time-consuming procedure, especially for a high-molecular weight sample, since it demands a delicate pre-stretching treatment that ensures the failure due to general because of a clipped-off sample and longer time to fully relax a sample before the experiment. Even though the increase in temperature may lead to the decreased experimental time, the higher limit of the temperature of an experiment on the FOR is defined by the temperature, at which sample starts to degrade. On the other hand, the lower limit of and experiment on a melt is defined by the glass-liquid transition temperature. Within these boundary conditions, a well-established procedure was

employed [11]. The use exclusive chromatograms show the signs of oligosaccharides only for the case of a polymer containing an oligosaccharide block.

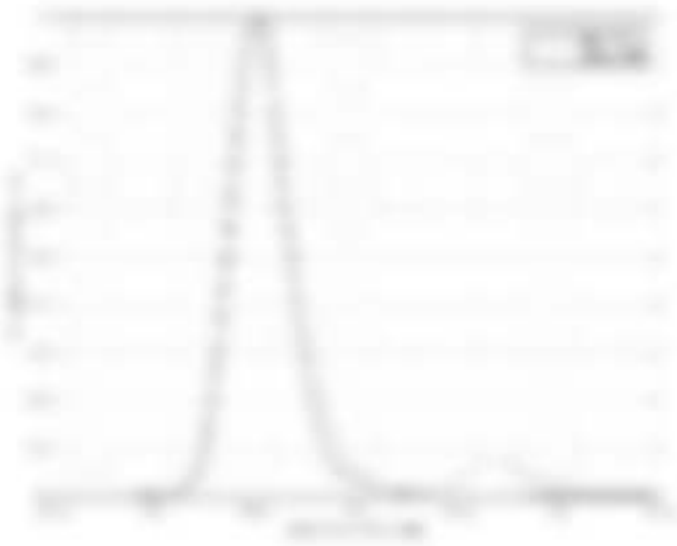

Figure 1. SEC of the polymer with oligosaccharide block before and after (dashed line) the Staudinger coupling reaction.

3. Conclusions

The methodology of using TTP as the solvent for anionic polymerization and further living heterocoupling have demonstrated effective way to synthesize model polystyrene stars, suitable for molecular biology studies. We give a special attention on the use a synthetic route of converting polystyryl to benzyl moiety in order to increase the yield of the macrocoupling reactions, since it leads to a less acidic sides near the star core that is more favorable during high-temperature studies. Also, Data from biological experiments obtained with the use of available stars should be reconsidered.

Acknowledgements

This research has been supported by the Danish Council for Independent Research – Natural Sciences (Grant 0602-02177B).

(1) M. Rigol, R.G. Hulet, J. Dunjko, Ion polymers in dense flow, Phys. Rev. Lett., 92 (2004) 190401.

(2) P.G. Avalos, S. Mikecin, Synthesis of star-shaped polymers, Designed Monomers and Polymers, 14 (2011) 525-548.

(3) R.W. Pekala, L.J. Fisher, Preparation of polyoxamide 1-aza-polybutadiene and polyacetylene resin, Macromol. 21 (1988) 1994-1996.

(4) D.J. Worsfold, J.-G. Zilliox, P. Rempp, Preparation et caracterisation de polymeres-sadbrik a structure en-etoile, par copolymerisation anionique sequencee, Can. J. Chem. Eng., 47 (1969) 3376-3380.

(5) A. Nkwae, T. Kgarebilwa, M. Nagwa, T. Sakwani, Nanoscale synthesis of well-defined many-armed star-branched polymers by an 'arm-first' methodology using a specially designed 1,1-diphenylethylene, Macromol., 39 (2006) 8891-8897.

(6) T.A. Osotwa, F. Nkwae, Silicon-oxidized preparation of branched polymers, Polymerized-divinylbenzene molecules, J. Phys. Chem., 47 (1943) 588-577.

(7) S.W. Ima, Synthesis of clinically-nonantibiotic trans-vial tri-arm polymers with „dendrimer" structures by use of a novel initiator, 2-phenylethylbenzene, Die Makromolekulare Chemie, 91 (1995) 152-166.

(8) J.E.L. Roovers, S. Bywater, Preparation and characterization of four-branched star polystyrene, Macromol., 7 (1972) 894-898.

(9) J.E.L. Roovers, S. Bywater, Preparation of six-branched polystyrene. Thermodynamic and hydrodynamic properties of four- and six-branched star polystyrenes, Macromol., 7 (1974) 443-448.

(10) M.P. Brizuela, C.P. Wofford, Synthesis of tri-arm and tri-arm-ester polybenzofuran, J. Polym. Sci., Part A: Polym. Chem., 3 (1965) 51-63.

(11) Q. Hwang, Molecular rheology of complex fluids, Technical University of Denmark, Lyngby, (2013).

(12) S. Nkwae, C.M. Pagadala, F.S. Bates, K. Almdal, Laboratory-scale anionic-vinyl polymerization with well-controlled, Rev. Sci. Instrum., 66 (1995) 5388-5393.

APPENDIX B

Stress relaxation of bi-disperse polystyrene melts : Exploring the interactions between long and short chains in non-linear rheology

Rheol Acta (2014) 53:549–574
DOI 10.1007/s00397-014-0778-9

CrossMark

Marie-Christine G. Laun Memorial Issue

Stress relaxation of bi-disperse polystyrene melts

Exploring the interactions between long and short chains in non-linear rheology

Ludovica Bicaregui[1] · Qian Huang[2] · Anatoly Ivankhin[3] · Nicolas J. Alvarez[3] · Kenneth Schweizer[3] · Ole Hassager[2]

Received: 30 September 2013 / Revised: 12 January 2014 / Accepted: 14 February 2014 / Published online: 26 February 2014

Abstract We present start-up of uniaxial extension followed by stress relaxation experiments of a bi-disperse PS 5 % by weight blend of 950k and 110k monodisperse weight polystyrenes. We also show, for comparison, stress relaxation measurements of the polystyrene melts with molecular weight 950k and 110k, which are the components of the bi-disperse melt. The measurements show three segmental relaxation regimes: a first regime, a reptation regime, and a slow regime. In the last regime, the orientation of the long chains is frozen and the stress relaxation is due to smooth relaxation of the short chains primarily. Coincidently in the slow regime, the long chains have extracted and undergo relaxation of orientation in fully relaxed short chains.

Keywords Polymer blends · Stress relaxation · Extensional flow

Introduction

Industrial polymers are largely polydisperse systems. One may research understanding polydisperse polymers is the experimental characterization and modeling of bi-disperse blends. In fact, the prediction of bi-disperse systems is a strong way to probe the validity of theoretical models.

The tension of entangled polymer chains has been described by the reptation theory of Doi and Edwards (1986a), which in its original form assumes that each polymer chain diffuses through a tube made of other polymer chains with a friction coefficient that is independent of the other chains. In this frame, the mutual influences of crossing chains were not considered and each chain moves out of its own tube assuming an equilibrium configuration irrespective of the state of the other chains. The tube through which the polymer diffuses is assumed to be fixed in time.

Over the years, many attempts were done to build blend tube laws based on the Doi–Edwards model (Lee et al. 1986a), Marrucci and Ianniruberto (2004), Read et al. (2011), van Ruymbeke et al. (2012), and van Ruymbeke et al. (2014a). Two main theories in the tube context were proposed: a constraint release (CR) mechanism by de Gennes (1971) and reptation, tube dilation (TD) mechanism by Marrucci (1985). The first mechanism is activated by the slow tube dynamics in which some of the entanglements surrounding the chains are released allowing more freedom to the lateral movements of the test chains. The TD mechanism says that the tube constriction is the main mechanism and relaxation of the surrounding short chains results in a widening of the tube diameter speeding up the relaxation of the longer chains. The function of the relevant mechanisms acts like a switch on the entanglement density.

The first developments in the description of the CR of the double reptation mixing rule was introduced by Tsenoglou (1987) and then Graessley (1982), which attempt to describe the constraint relaxation regime, more sensitive to the bi-modal molecular weight distribution. In this approach, the entanglement between two different MWs chains is a random

✉ Ole Hassager
ole@kt.dtu.dk

[1] Department of Chemical and Biochemical Engineering, Technical University of Denmark, Bld. 229, Sølvtofts Plads, 2800 Kgs. Lyngby, Denmark

[2] Department of Micro and Nanotechnology, Technical University of Denmark, Bld. 345B, Kgs. Lyngby, Denmark

[3] Department of Chemical and Biomolecular Engineering, Cornell University, 120 Olin Hall, Ithaca, NY 14853

reveals proportionality to the volume fraction of the components and to even as one of the two polymers diffuses using the coupling power formed by the entanglements with minor sensitivity to this. This holds also if the tangent orientation rates of the two components are sufficiently apart from each other. Validations were found with experimental viscosities shown combined with shear-rate spectroscopy on entangled binary blends of linear cis polyisoprenes (Watanabe et al. 1999a) and Watanabe et al. (1999b).

Stroglinski (1987) and Stroglinski and Graessley (1986) investigated the linear viscoelasticity of five series of well entangled binary melts of linear polybutadienes, each with a wide range of concentrations. The ratio between the molecular weight of the long and the short molecules M_w/M_s ranged between 2.5 and 10.7. Besides the experimental results, they suggested some molecular theories, and the based just on the tube and reptation model and have adding mechanisms such as path length fluctuations and constraint release. They introduced the existence of two different relaxation behaviours characterized by a relevant parameter defined as $G_N^0 = \Phi_s \Phi_l^2 G_N^0$, where Φ_s and Φ_l are respectively the molecular weight of the long and the short components, and Φ_l is the molecular weight of a strand between two entanglements. The critical value of the parameter defines the limit of the two cases. Preparing the long polymer components concentrate in a melts made up of monodisperse with short and long chains L (1 ... 1)$_n$, the entanglements with short chains are long lived because the high M_w chain relaxes in a region constrained by both entanglements, called tube cells, and the relaxation time of the long chains is independent of blend composition. Conversely, (1 0 ... 0)$_n$, short chains concentrate on one monomer unit to define the long chain path and tube dilation takes place, i.e., the long molecules diffuse in the tube cells where the only active constraints are within long polymers.

The exact value of G_N^0 is not universally recognized. The original one proposed by Stroglinski and Graessley was 1, whereas in a later work of Fetsh and Larson (1998), was empirically found as 0.084, which gave a better estimate to describe the two regimes of the relaxation and dilation tube. The authors proposed an extended version of the Milner-Mcleish model (Milner and Mcleish 1998) from linear monodisperse polymers to linear bi-disperse melts incorporating dynamic tube dilation (DTD) and Rouse contraint release mechanism (CRR). The two work a divided into three regimes. In Uni one used the relaxation time of the short chains, an intermediate one that lays up to the relaxation of the long chains, and the terminal one after the constraint relaxation of the long chains. Predictions showed good agreement with a wide series of linear viscoelastic data of bidisperse 1,4 polybutadienes and polyisoprenes. Linear melts examined on a large range of G_N^0 values.

Some relaxations experiments from main chain to star Chinese have shown that a cooperative effect exists between chains. In particular, Rosedahl et al. (1999) used a dielectric technique to measure the dynamic relaxation in the relaxation phase following step shear for such components in bi-disperse entangled polymer melts of hydrogenated polybutadiene (polyethylene-co-butene) containing from 35 to 75 % wt. of long chains. They found that polydispersity can strongly affect the relaxation process of the components, decreasing the longest relaxation time of the high molecular weight polymer and delaying the longest relaxation time of the short component regardless the M_w of the long chain matrix. They explained that the observed slower relaxation of the shorter molecules is due to a combined effect of entanglement in the orientation of the Rouse segments and a memory orientation induced by the neighbouring long chains.

More recently, Inkinbhaven et al. (2017) suggested a reduction of the monomeric friction coefficient caused by alignment of the Kuhn segments of polymer chains. The stretch-orientation induced reduction of the friction is based on the molecular concept that aligned object gyrate into an anisotropic and reduced friction when parallel to each other as relative to the random configuration. Based on the same concept, Narita et al. (2011) further investigate the molecular origin of the different behaviour between polymer melts and solutions with primitive chain simulations. In a more recent study on solvent effects in monodisperse concentrated polymer solutions, Huang et al. (2015a) also addressed to the existence of intimate interactions between solvent-polymer and polymer-polymer molecules to explain an observed dependence on solvent nature in non-linear viscoelastic flow.

Compared to monodisperse polymer melts and solutions, the situation is more challenging for bi-disperse entanglement melts because they emphasize complex interactions between long and short chains especially in non-linear relaxation process. Non-linear viscoelastic properties in entanglement flow have not been investigated as intensively. Experimental data of polystyrene blends of super high M_w dissolved with small oligomeric fractions, in a matrix of shorter polydisperse chains were modelled by Wagner et al. (2001). The predictions showed that increasing the amount of the long component in the blends resulted in more strain hardening.

Nielsen et al. (2006) characterized three bi-disperse polystyrene melts in non-linear extensional flow, which are the only measurements that reached steady state for bi-disperse systems to our knowledge. They mixed 95–98k with 371–390k in two different concentrations to investigate

the effect of dilution, as well as PS-NHBz with PS-NHBz in the same concentration of the previous one to cover the effect of short molecular length. A monotonic relative to the τ_{H_2} in the steady state compartment viscosity vs. elongational rate was observed for all the samples. Consistently to the observations of Wagner et al. [24,25], the decrease of strain hardening increases as the long chains are more diluted. Relying on the few available commercial data, several scaling laws have been developed for predicting the zero-shear viscoelastic behaviors of H-shaped or Pom-pom-like polymers et al. [26,27] Wagner [28,29], Bernstein [30,31].

A more recent work by Auhl et al. [24,32] focuses on the effect of chain severity of long chains when diluted by shorter ones. Their up elongational data of two series of binary blends of polystyrene with broad concentration ranges are fitted with a model that combines three predictions: long chain branch segments at lower locality, recent where the long chains are diluted by the short ones than in the pure melt. They explain this behavior by a proposed novel mechanism, the effective branch relaxation time, which implies the recent relaxation of the tie tube through the motion of the chain in the tube tube.

However, data of shear relaxation following nearly monotonic flow, which are more relevant for the melts' modeling of relaxation mechanisms of H-shaped systems, are still missing.

In the present work, we investigate a H-shaped PS-H by weight blends of PS and PS molecular weight polystyrene. For which the commercial Polydisperse Polymer Laboratories GPC − 3.0.3.0, referred to Mount Mk, Mk, is both advanced commercial flow and shear relaxation. The purpose is to investigate compositive interactions between polymer chains and monitor how the entanglement of the short chains is affected in the presence of the long chains. Data for the blends are compared to data for the pure components.

Experimental

Synthesis and characterization

The polystyrene PS-NHBz used in this work has been previously described and characterized in both shear and extensional rheology by Huang et al. [30,33]. The polystyrene PS-NHBz has been synthesized by means of living anionic polymerization according to the established procedure by Nikitin et al. [34,35]. The reaction was carried out for 4 h at 35 °C in benzene, described cyclohexane, with the use of the titrated solution of sec-butyllithium as initiator as the initiator. The molar mass of PS-NHBz was determined with size exclusion chromatography (SEC) with non-stabilized tetrahydrofuran (THF) as the eluent and with the use of a refractive index detector, at a 1 mL/min flow rate and two SDV 1 × 0 mm² columns (PSgel Mixed-C and Mixed-D). The system was equipped with a triple detector/viscometer including a combined 3 Viscotek model 200 differential refractive index (DRI), a differential viscosity detector and a Viscotek model 125 dual angle laser light scattering detector (RALS/LS). On the basis of calibration with narrow molar mass polystyrene standards and low one signal adjusting according to Spatorr signals, the values of the weight-average molecular weight M_w and the polydispersity index PDI, defined as the ratio of the M_w over the number-average molecular weight M_n, were determined. Table 1 summarizes the weight-average molecular weight M_w, and the polydispersity index PDI of the two polystyrenes.

Table 1. Properties of the two monodisperse polystyrene components (Mw = short for PS-NHBz, as taken from Huang et al. [33,34])

Sample	M_w (g/mol)	PDI	τ_{H_2} (s)	τ_{H_2} (s)	T_g
PS-NHBz	140,000	1.11	86.700	700	373
PS-NHBz	97,000	1.07	4000	2000	7 10

Blend preparation

The polystyrene blends was prepared using the two monodisperse melts described above. PS-NHBz and PS-NHBz were dissolved together in THF and the solution was stirred at room temperature for 72 h. Since both components were well dissolved and mixed homogeneously, the THF solution was poured into methanol drop by drop, which precipitated out the blends. The precipitated blends was recovered by filtration. The wet powder was then dried for more than 48 h in open air and later dried in a vacuum oven at 70 °C for 2 weeks to ensure the complete evaporation of the residual solvent. To check cross-sectional homogeneity, two samples at different locations of the blend were cut in half. The cross-sectional analysis was conducted by integral evaluation of the peak areas of the Viscotek curves in SEC to make sure that the desired concentration was obtained.

Table 2 summarizes the corresponding weight fraction of the components in the bi-disperse blends Mk, Mk. The

Table 2. The weight fractions of PS-Mk and PS-Mk, and the weight-average molecular weight M_w (g/mol) of the Blend Mk, Mk

Sample	ω_{PS-Mk} (%)	Mk	ω_{PS-Mk} (%)	Mw	M_w (g/mol)
Blend Mk, Mk	40 k		60 k		110,000

weight average molecular weight $\bar{M}_w$ has also been subtracted for the break and the value is expressed in the same units.

Methods of spectroscopy

The linear viscoelastic of the pure nanodiagnostic poly-crystals under the Mount Silk SDS have been measured on an ARES-G2 rheometer from TA Instruments with an 8 mm parallel plate geometry. Small amplitude oscillatory shear flow measurements were performed for all three samples at 150, 170, and 190 °C in nitrogen atmosphere. The data were shifted to a single master curve at 150 °C using the principle of time–temperature superposition (TTS). The time–temperature shift factors (a_T) (Ni, Ni, Ni), and the Mount Silk. Still was found to be approximately with a single Williams–Landel–Ferry (WLF) equation of the form:

$$\log a_T(T) = \frac{-C_1 (T - T_{\mathrm{ref}})}{C_2 + (T - T_{\mathrm{ref}})} \tag{1}$$

where $C_1^{\mathrm{T}} = 0.70$ and $C_2^{\mathrm{T}} = 46.15$ K, $T_{\mathrm{ref}} = 150$ °C and T is the temperature in °C.

Environmental Sites

The environmental micro measurements were performed with a Dispersive scattering Aerodynamic (DMS) (Bacik et al. 2007b; Krumm-Wischer et al. 2011). The DMS has been recently used (Ural) with the introduction of two independent detectors, one connected to the sea plate and the other one connected to the wave. Before starting an experiment, the samples of Mount Silk SDS were stocked into a cylinder or shaped pellets with a focal radius $R_0 = 1.7$ mm and a thickness of L_0, between 1.2 and 1.45 mm, giving an aspect ratio $r_0 = L_0/R_0$ ranging between 0.65 and 0.71. The water procedure was followed for the measurements: 0.5 MPa samples, a record that the author R_0 was 1 mm and the thickness L_0 was recorded 2 mm for all the samples. It might also first on an SDS-free micro-capped in the samples, the shock pressure pressure was verified to approximately 150 °C for 30 min and then pre-cooled and equilibrated to the room temperature under vacuum for an additional 30 min, to ensure the complete evaporation of the pressure vapour. Before each experiment, the sample was allowed to relax when any recording to a radius R_0. The Newtonian strain is calculated from the instantaneous of the main Ordovician radius $R(t)$ as

$$\varepsilon = -\ln\left[R(t)/R_0\right] \tag{2}$$

while the strain rate is defined as $\dot{\varepsilon} = d\varepsilon/dt$. The mean value of the difference between the strain and the radial stress in the axial Poisson ν obtained from the measured values of $T(\varepsilon)$ and $R(\varepsilon)$, with a force balance that neglects surface tension and inertial effects as expressed by Scales (1987) and Scales and Michaelis (2005) as

$$\Delta\sigma_{zz} = \sigma_{zz}(\varepsilon) - \frac{F(\varepsilon) - \pi R_0 \gamma_0 L^2}{\pi R(\varepsilon)^2} \tag{3}$$

where $F(\varepsilon)$ is the axial force, γ_0 is the gravitational acceleration and σ_{zz} is the weight of the Newtonian. A small tension during the start up of the experiment from, there is a constitution in the stress difference that arises from the shear components in the deformation field. This effect is caused by the no-slip boundary condition on the end plates, and is more pronounced at small aspect ratios (Pontoizeau et al. 2006). This effect must be compensated by a correction factor as implemented in Bacik et al. (2020) that removes less than 1 % deviation from the corrected values given. For large strains, the corrections matches and the radial symmetry of the stress in the symmetry plane becomes negligible (Bacik et al. 2007). Finally, the corrected stress growth coefficient is calculated as

$$\eta^+ = \frac{\Delta\sigma_{zz}(\varepsilon) + \Delta\sigma_{rr}(\varepsilon)}{\dot{\varepsilon}} \tag{4}$$

Stress relaxation measurements present a special challenge, since strains holding the plates does not produce a true stress relaxation experiment. To stress relaxation the Newtonian will be subjected to a complex core bonding, as in Krumm-Wischer et al. (2007) Cybis et al. (2005). A rectangular is prepared in direct stress relaxation experiment following steady shear at constant an extension which has been introduced by Newtonian et al. (2000) on the above mentioned DMS. The density, computer on the use of a closed loop controller that maintains the axial Ordovician dimension, at this is up the starting is recorded by adjusting the pressure of the top plate. In a stress relaxation experiment, at the start up of the change time, an extreme strain rate is applied on the sample. At time as the stress relaxation starts to an arbitrarily given boundary strain ε_0, the axial Ordovician radius R must coincide to the pulse compact long, giving $\dot{\varepsilon} \to 0$. The constitutive stress decay and Poisson during the stress relaxation is defined as

$$\eta^- = \frac{\Delta\sigma_{zz}(t) + \Delta\sigma_{rr}(t)}{\dot{\varepsilon}} \tag{5}$$

where t is the strain rate in the start up of the measured stress relaxation from. The stress shows contributions, measurement before for the start up of the correction from, is negligible during the stress relaxation process (Pontoizeau et al. 2006).

Results and analysis

Linear viscoelasticity

The storage modulus G' and loss modulus G'', plotted as a function of the angular frequency ω, are shown in Fig. 1 for

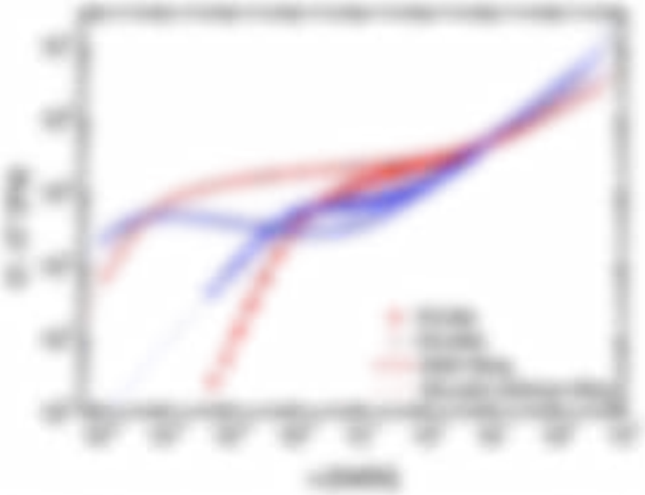

Fig. 8. ICM two-halo term with the 3DHP prescription and the Halo-only collaborative boost for M1-100k and M2-100k at $z = 0.5$.

M1-100k and M2-100k, and at $k_{\rm max} = 5$ for the Illustris-3G, IA3-100k. The CCL data for the two cosmologies match their Level-A code to a satisfactory fraction of a percent, while the 3DHP calculation can create discrepancies of a few percent. We refer the interested reader to Appendix A of Chisari et al. (2019a) for a detailed discussion of the differences between the two codes.

5 THE HALO MODEL

5.1 Halo model ingredients

In this section we describe the ingredients of the halo model calculation of the 3D power spectrum of matter and galaxies. We follow the notation and conventions of Cooray & Sheth (2002). The halo model is based on the assumption that all matter in the Universe is contained in dark matter haloes, and that the statistics of the matter distribution can be described by the statistics of the haloes and the statistics of the matter within the haloes. The halo model power spectrum of matter is the sum of two terms, the 1-halo term and the 2-halo term, which dominate on small and large scales respectively. The 1-halo term is given by

$$P_{\rm 1h}(k,z) = \int_0^\infty {\rm d}M \frac{{\rm d}n}{{\rm d}M}(M,z) \left|\frac{u(k,M,z)}{\bar{\rho}_{\rm m}}\right|^2 , \tag{45}$$

$$P_{\rm 2h}(k,z) = P_{\rm lin}(k,z) \left[\int_0^\infty {\rm d}M \frac{{\rm d}n}{{\rm d}M}(M,z) b_{\rm h}(M,z) \frac{u(k,M,z)}{\bar{\rho}_{\rm m}}\right]^2 , \tag{46}$$

$$P_{\rm mm}(k,z) = P_{\rm 1h}(k,z) + P_{\rm 2h}(k,z) . \tag{47}$$

The quantity $\frac{{\rm d}n}{{\rm d}M}(M,z)$ is the halo mass function, which describes the number density of haloes per unit mass and volume. The mass function is a universal function of the peak height $\nu = \delta_{\rm c}/\sigma(M,z)$, where $\delta_{\rm c} \approx 1.686$ is the critical density for collapse and $\sigma(M,z)$ is the root mean square of the linear density field smoothed with a top-hat filter in real space of radius $R = (3M/4\pi\bar{\rho}_{\rm m})^{1/3}$. The mass function is calibrated against numerical simulations. We use the Tinker et al. (2008) mass function for the 3DHP prescription, and the Bocquet et al. (2016) mass function for the Halo-only prescription. The quantity $b_{\rm h}(M,z)$ is the halo bias, which describes the relation between the clustering of haloes and the clustering of matter. We use the Tinker et al. (2010) halo bias for the 3DHP prescription, and the Bocquet et al. (2016) halo bias for the Halo-only prescription. The quantity $u(k,M,z)$ is the Fourier transform of the density profile of matter in haloes, normalised by the halo mass. We use the Navarro et al. (1997) density profile with the concentration-mass relation of Duffy et al. (2008) for the 3DHP prescription, and the Mead et al. (2016) density profile with the concentration-mass relation of Bullock et al. (2001) for the Halo-only prescription. The quantity $P_{\rm lin}(k,z)$ is the linear matter power spectrum, which we obtain from CAMB (Lewis et al. 2000; Lewis & Challinor 2011). The quantity $P_{\rm mm}(k,z)$ is the total matter power spectrum.

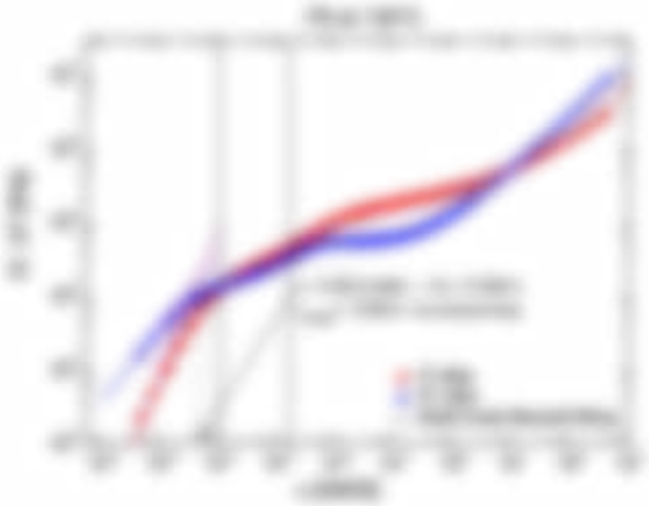

Fig. 9. 1-halo term (dash) and 2-halo term (dot) of the Halo-only Bocquet et al. prescription for M1-100k at $z = 0.5$.

Similarly, the 1-halo and 2-halo terms of the galaxy power spectrum are given by

$$P_{\rm 1h}(k,z) = \int_0^\infty {\rm d}M \frac{{\rm d}n}{{\rm d}M}(M,z) \left|\frac{u_{\rm g}(k,M,z)}{\bar{n}_{\rm g}}\right|^2 , \tag{48}$$

$$P_{\rm 2h}(k,z) = P_{\rm lin}(k,z) \left[\int_0^\infty {\rm d}M \frac{{\rm d}n}{{\rm d}M}(M,z) b_{\rm h}(M,z) \frac{u_{\rm g}(k,M,z)}{\bar{n}_{\rm g}}\right]^2 , \tag{49}$$

$$P_{\rm gg}(k,z) = P_{\rm 1h}(k,z) + P_{\rm 2h}(k,z) . \tag{50}$$

Here, $u_{\rm g}^{\rm cen}$ is the galaxy profile, $u_{\rm g}$ is the characteristic value of the galaxy profile, $\bar{n}_{\rm g}$ is the integral constraint term, $\alpha_{\rm g}$ and $\kappa_{\rm g}$ are the virial exponent of the counts-in-cells and the galaxy spectra in a log-log plot, $\mathcal{I}(x,z)$ is the Poisson-like exponential truncating the 1-halo term at the scale of the host haloes. The values of $\alpha_{\rm g}$ and $\kappa_{\rm g}$, which are cosmology-specific constants, were found in 0.57 and 0.76, respectively, in the case of specific wCDM cosmologies and redshift bins (Chisari et al. 2019; Fluri et al. 2019), while the other three parameters $\langle N_{\rm c}^{\rm g} \rangle$, $\langle N_{\rm s}^{\rm g} \rangle$ and $\gamma_{\rm g}$ were optimised for the fiducial cosmological model of the modelling of 3DHP parameters can be found in Fluri et al. (2019). For cosmological parameters, we exploited here the asymptotic model in the galaxy regime

$$\mathcal{I}^{\alpha_{\rm g}}(x,z) \approx \left(\frac{x}{\gamma_{\rm g}\Gamma(\alpha_{\rm g}+1,\gamma_{\rm g})}\right)^{\alpha_{\rm g}} \exp\left(-x^{\kappa_{\rm g}}\right) \quad \text{for } x \to +\infty , \tag{51}$$

$$\text{and } \mathcal{I} \to \mathcal{I}^{\alpha_{\rm g}}(x,z) \to 1 \quad \text{for } x \to 0 . \tag{52}$$

Correspondingly, it may be shown that the truncation model also in the galaxy regime $x \to +\infty$ has the galaxy bias behavior

$$b_{\rm h}(x,z) b_{\rm g}^{\rm cen}(x,z) \to \Gamma(\alpha_{\rm g}) \exp(x) x^{-\alpha_{\rm g}} , \tag{53}$$

where $\Gamma(x)$ is the Gamma function.

The numerical properties of the two HI power-spectrum models obtained from the 3DHP fitting of the sources used in 3.3 are found in Table 4, together with the value of the root-mean-square velocity $\sigma_{\rm v}$ and the average temperature from $T_{\rm b}$ (Pritchard et al. 2008) as the integral

$$\bar{T}_{\rm b} = \int_0^\infty {\rm d}z \, T_{\rm b}(z) \frac{{\rm d}n}{{\rm d}z}(z) . \tag{54}$$

Table 4. Numerical properties of HI halo and HI 21cm observables for the 3DHP fitting. Values of the HI 21cm power spectrum fitting at $z = 0.5$ (Chisari et al. 2019).

Parameter	HI-100k	HI-1Mk
$\alpha_{\rm g}$	0.57	0.57
$\kappa_{\rm g}$	0.7	0.7
$\sigma_{\rm v}^2$ / (Mpc/h)^2	1.0e+04	1.0e+04
$\gamma_{\rm g}$ [-]	0.001	0.001
$\gamma_{\rm g}$ [-]	0.736	0.611
$\gamma_{\rm g}$ [-]	0.499	0.418
$\gamma_{\rm g}\Gamma(\alpha_{\rm g}+1,\gamma_{\rm g})$ [-]	0.621 - 07	0.621 - 07

Table 4. Maximal concurrence $\mathcal{C}(0)$ ebits and $\mathcal{C}(t)$ ebits, observed from the Bloch Sphere.

Bell parameters	$\mathcal{C}(0)$ ebits	$\mathcal{C}(t)$ ebits
$\mathcal{M}_1$ (Symbol)	1.0	0.0
$\mathcal{C}_1$ ($\mathcal{M}_1$)	1.0×10^{0}	1.0×10^{0}
$\mathcal{C}_2$ (0)	0.00	0.07
$\mathcal{C}_3$ (0)	0.1	0.1

$$\mathcal{C}_4 = \frac{\int_{\mathcal{C}_2}^{\mathcal{C}_3} \mathcal{M}(\mathcal{C}_1)\,d\mathcal{C}_1}{\int_{\mathcal{C}_2}^{\mathcal{C}_3} \mathcal{M}(\mathcal{C}_1)\,d\mathcal{C}_1} = \frac{\mathcal{C}_3 + \mathcal{C}_2}{\mathcal{C}_3 - \mathcal{C}_2}\mathcal{C}_1, \tag{4.6}$$

In both experiments, the slot indicates that the primary control functions have been neglected. From the value of the parameter $\mathcal{C}_4 = 0.70$ corresponding to $\mathcal{M}(\mathcal{C}) = 2$, as the force fit to the data. It reflects the origin of $\mathcal{C}^{-1}(\mathcal{C})$ for large Josephson. This explains consistently referred to as the Bessel equation has been extensively analyzed (Lieberman and Mercurio 2005) in terms of conventional and non-conventional Bessel systems. We include therefore in Fig. 4 the Mercurio–Lieberman (ML) theory predictions (Table 5). The predictions is almost identical with the BESS fitting except in the form of large Josephson, where the ML theory shows $\mathcal{C}^{-1}(\mathcal{C}) \sim \mathcal{C}^{-1}(\mathcal{C})$ in contrast to the data.

For the Osaki, we use the Multi-modal Maxwell eigenstate in the form

$$\mathcal{C}(\mathcal{C}) = \sum_{\mathcal{C}=0}^{\mathcal{M}-1} \mathcal{M}_{\mathcal{C}}\, e^{-\mathcal{C}\mathcal{C}_{\mathcal{C}}}, \tag{4.7}$$

The Maxwell fitting parameters $\mathcal{C}_1$ and $\mathcal{C}_2$ for the Bloch ML-300 are reported in Table 6. The value of the zero-shear-rate viscosity and average relaxation time computed from the distribution in Eqs. (3) and (4) becomes respectively $\mathcal{C}_0 = \sum_{\mathcal{C}=1}^{\mathcal{M}} \mathcal{C}_{\mathcal{C}}\mathcal{C}_{\mathcal{C}} = 3.02 \times 10^{4}$ Pa s and $\mathcal{C}_1 = \sum_{\mathcal{C}=1}^{\mathcal{M}} \mathcal{C}_{\mathcal{C}}/\sum_{\mathcal{C}=1}^{\mathcal{M}} \mathcal{C}_{\mathcal{C}} = 2.11 \times 10^{0}$ s.

Table 5. Bloch Sphere parameters $\mathcal{C}_1$ and $\mathcal{C}_2$ for the Bloch ML-300.

$\mathcal{C}$	$\mathcal{C}_1$ (Pa s)	$\mathcal{C}_2$ (s)
1	4.1×10^{4}	1.41×10^{0}
2	1.40×10^{4}	4.13×10^{0}
3	1.11×10^{4}	1.16×10^{1}
4	6.47×10^{3}	2.14×10^{1}
5	2.31×10^{3}	4.01×10^{1}
6	7.28×10^{2}	7.21
7	7.66×10^{2}	1.21
8	1.66×10^{2}	2.44×10^{-1}
9	4.04×10^{1}	4.01×10^{-1}
10	1.11×10^{1}	6.17×10^{-1}
11	1.11×10^{0}	1.11×10^{-1}
12	7.14×10^{-1}	1.88×10^{-1}

Comparing the average relaxation time $\mathcal{C}_{\mathcal{C}} = 7.1$ ms for the Bloch ML-300 with the one obtained from the BESS fitting of the LVE data of the pure NBR, long component $\mathcal{C}_{\mathcal{C}} = 7.1$ ms, both computed with Eq. (4), we can affirm that the constant relaxation of the long chains in the blend is somewhat faster than in the pure melt. We take this to mean that the long chains are relaxing in a tube tube where the short chains are not imposing significant constraints. In the frame of the Doughnuts Constraint Release, we are consequently in the limit of $\mathcal{C}\mathcal{C} \longrightarrow \mathcal{C}\mathcal{C}_{\mathcal{C}}$. The parameter $\mathcal{C}\mathcal{C} = 0.1$ (Table 5) is close to agree with the value of 0.0864 reported by Pauli and Lawson (1985) rather than the value $\mathcal{C}\mathcal{C}_{\mathcal{C}} = 1$ reported by Doughnuts (1985) and Doughnuts and Lawson (1986).

Start-up of uniaxial flow

The molecular weight $\mathcal{M}_{\mathcal{C}}$ of the two monodisperse components in Bloch ML-300 is selected such that their respective longest relaxation times are well separated from each other. We expect therefore that different mechanisms can be activated for each component independently. The Bessel time $\mathcal{C}_{\mathcal{C}}$, which indicates the onset of relaxation time, is defined as $\mathcal{C}_{\mathcal{C}} = \mathcal{C}^{-1}\mathcal{C}_{\mathcal{C}}$, where $\mathcal{C}_{\mathcal{C}}$ is the relaxation time of the strand between two entanglements with molecular weight $\mathcal{M}_{\mathcal{C}}$, and $\mathcal{C} = \mathcal{M}_{\mathcal{C}}/\mathcal{M}_{\mathcal{C}}$ is the number of entanglements per chain. We use $\mathcal{M}_{\mathcal{C}} = 12{,}000$ g/mol (Bloch et al. 1985a) to determine the value of $\mathcal{C}$ for our monodisperse melts. The equation time $\mathcal{C}_{\mathcal{C}}$, which indicates the maximum relaxation time of a whole chain, can be obtained from LVE measurements. The values of $\mathcal{C}_{\mathcal{C}}$, $\mathcal{C}_{\mathcal{C}}$, and $\mathcal{C}$ for the two monodisperse polystyrenes are listed in Table 7.

As already the regimes, we wish to interpret the dynamics in terms of tube concepts for the components. We estimate the Bessel times of the short and long constituents in the blend to be identical to those in the pure melts given in Table 7. Moreover, since the long chains are considerably frozen at the relaxation time of the short components, we may roughly estimate the constant relaxation time of the short chains to be approximately equal to that of the pure melt. However, the terminal relaxation of the blend will be equivalent of the long chains in a sea of fully relaxed short chains. As an estimate for this time, we use the relaxation time $\mathcal{C}_{\mathcal{C}}$ obtained from the Maxwell spectrum. Hence, we refer to the relaxation times in Table 8.

To relate the relaxation in terms of the molecular parameters of the two components, we illustrate the results here in

Table 6. Time constants for short and long components in the blend.

Bloch ML-300	Bessel time	Terminal time
Short component	$\mathcal{C}_{\mathcal{C}} = 0.1$ ms	$\mathcal{C}_{\mathcal{C}} = 0.6$ ms
Long component	$\mathcal{C}_{\mathcal{C}} = 7.1$ ms	$\mathcal{C}_{\mathcal{C}} = 11.4$ ms

Table 7 Wino-bino exclusion fits to the Run 2 one-lepton with soft-leptons and two-lepton with opposite-sign leptons analyses [3,4]. The $m(\tilde{\chi}_1^0)$ and $m(\tilde{\chi}_2^0)$ values are given in GeV. The Δm values are given in GeV. The Δm values are given in GeV. The Δm values are given in GeV. The Δm values are given in GeV.

bands of their data–expected. Based on the exclusion curves from Table 6, we define wino-bino-motivated search cases in terms of the Wino-scaling variables $R^{\pm}$ and R^{0} for the short and long cases as expressed in Table 7, where the superscripts 1 and 2 refer to short and long cascade respectively.

Figure 7 shows the associated cross-section normalised cross-section coefficient C production as functions of Δm as in Ref. [3] for the Monte Carlo (MC) The sample was simulated in 2+1 different cases, 1, which corresponded to 2 to 20 bands, four regions separated by the separation cases and Wino cases of the long and short cases. For the corresponding cross-section $\sigma(\tilde{\chi}_1^{\pm}\tilde{\chi}_2^0)$ we get the cases as the shortest search cases $\sigma \times \pm$ 10 $^{-1}$ pb^{-1} and $\sigma \times \pm$ 10 $^{-1}$ pb^{-1}. These two cases are located at 100 GeV and shifted at 150 GeV according to the Time Temperature Superposition principle, with 2000 for $\sigma \times \pm$ 10000 and $\sigma \times \pm$ 0.05. The solid line in the plot is the LO10 prediction calculated from the parameters listed in Table 1. The disagreement between the data good agreement with the LO10 at small results. The corresponding $\sigma \times \pm$ 10 $^{-1}$ theory follows the LO10, except at high

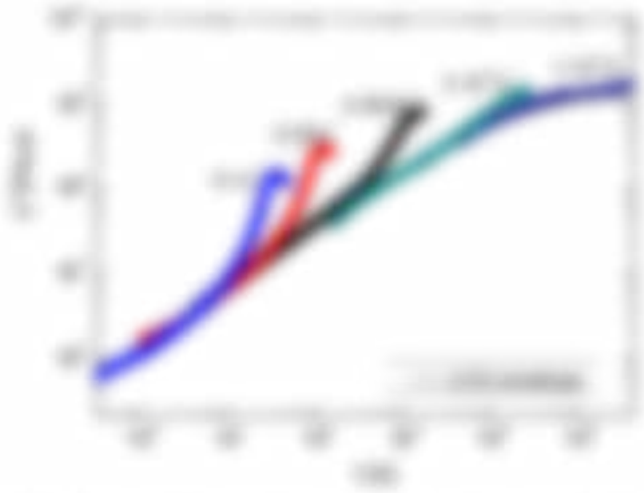

Fig. 7 Wino cross-section coefficient as function of Δm for the Monte Carlo (MC) simulation in Ref. [3]. The cross-section coefficient is calculated for the short cases and for the long cases, corresponding to the LO10 cross-section prediction. The solid line is the LO10 prediction based on the parameters listed in Table 1.

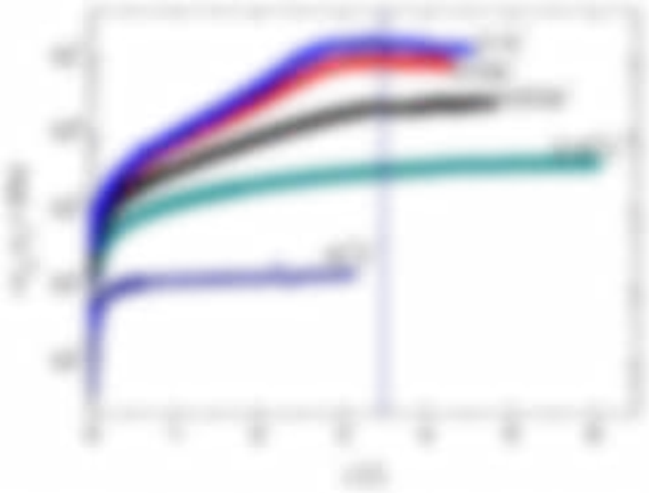

Fig. 8 The observed cross-section upper limit for short and long cases as a function of Δm. The cross-section coefficient is calculated for the short cases and for the long cases, corresponding to the LO10 prediction based on the parameters listed in Table 1.

Results, strain where the cross is slightly higher. In this strain the $\sigma \times$ region the cascade in the LHC data in the right Wino configuration, since $\sigma \times \pm$ 10 $^{-1}$ which means that the Time is not fast enough to cross the process. Also the $\sigma \times$ increases, cross-sections decreased from the LO10 prediction of the experimental curves is observed, meaning that the cases experiences higher degrees of scrambling, which results in more strain hardening. It is as $\sigma \times \pm$ 10 $^{-1}$ pb^{-1} strain hardening, $\sigma \times$ 10 $^{-1}$ pb^{-1} light strain hardening, $\sigma \times$ shear rate. This is in the in agreement with the work of Gabi et al. [3,4] who predicts on the cases on the smooth interaction rate of the pure long cluster when diluted by chronic chains. From Table 7, $\sigma \times$ can be seen that only for the highest search case $\sigma \times \pm$ 10 $^{-1}$ pb^{-1} $\sigma \times$ addressing the short cluster are associated to the Time. In Figure 8, as above, the cases can smooth mechanical stress differences $\sigma \times$ $\sigma \times$ provided as a function of Weissenberg number in LO10 TeV in the Monte Carlo (MC) From this plots, it is clear that $\sigma \times$ $\sigma \times$ reaches a steady state value above $\sigma \times \pm$ 10 for each search case. This allows the discrimination of a steady state viscosity $\sigma \times$.

Relaxation after Fault Slow data

The network connectivity Time was assigned to the start up after a Fault Slow data of $\sigma \times \pm$ 10 $^{-1}$ s and then stress relaxation was performed. Figure 9 shows the measurements in LO10 TeV $\sigma \times$ 10 $^{-1}$ pb^{-1} and $\sigma \times \pm$ 10 $^{-1}$. The Weissenberg number corresponding to the Wino strain rates $R^{\pm}_{\tilde{\chi}_1^0} \times$ 10 $^{-1}$ and $R^{0}_{\tilde{\chi}_2^0} \times$ 10 $^{-1}$, 10, and 10 $^{-1}$, revealing that the long clusters are in an equilibrium associated to the force while the short components are more in equilibrium as the stress is relaxed, $\sigma \times$ 10 $^{-1}$ pb^{-1} and associated to the highest strain rate.

To analyse the data, it is as suitable to use the LO10 equation for the Maxwell spectrum of the strain using [3]. If we think

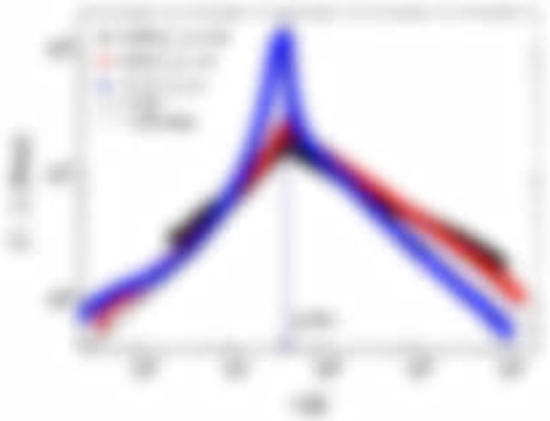

Fig. 2. Source relaxation accompanies all the Model-NK-SIS effects. Solid lines show $I_{\mathrm{ss}}(\tau)$ of canonical exceptions. The synchronous case unchanged as $\tau = 0.5$ ($\alpha = 0.5$, $\beta = 1$, $\gamma = 0$, $\delta = 0$). The solid line is $\alpha = 0.5$ ($\alpha + \beta = 1$) and the dashed line is $\alpha = 0.5$ ($\alpha + \beta = 1$). Dashed lines show the same parameters but $\tau = 0.5$ ($\alpha + \beta = 1$). Initial and boundary conditions are fixed as in Table 1.

the data were such that the first to finish ($\tau = \tau_{\mathrm{fin}}$) when $\tau_{\mathrm{fin}} = \alpha_{\mathrm{fin}}\beta$ for $\alpha < 0$. The same Bessel function $\tau = 0$ is ground on the Bessel convolution. Solid by

$$I_{\mathrm{ss}}(\tau) = \tau \sum_{k=0}^{\infty} \frac{(\alpha+\beta)_k}{k!\,\Gamma(k+2)} (-\gamma\tau)^k \quad (26)$$

If τ is dimensionless we consider the zero limits $\alpha \to 0$ series above after term-by-term, while $\beta_{\mathrm{fin}} \to 1$ ($\tau = 0$ with $\beta_{\mathrm{fin}} \to$ to exhaustion after steady. Series

$$\text{step} \quad \text{solids} \qquad I_{\mathrm{ss}}(\tau) = \tau \sum_{k=0}^{\infty} \frac{(\alpha+\beta)_k}{k!\,\Gamma(k+2)} (-\gamma\tau)^k \quad (27)$$

$$\text{steady} \quad \text{State} \qquad I_{\mathrm{ss}}(\tau) = \tau \sum_{k=0}^{\infty} \frac{(\alpha+\beta)_k}{k!\,\Gamma(k+2)} (-\gamma\tau)^k \quad (28)$$

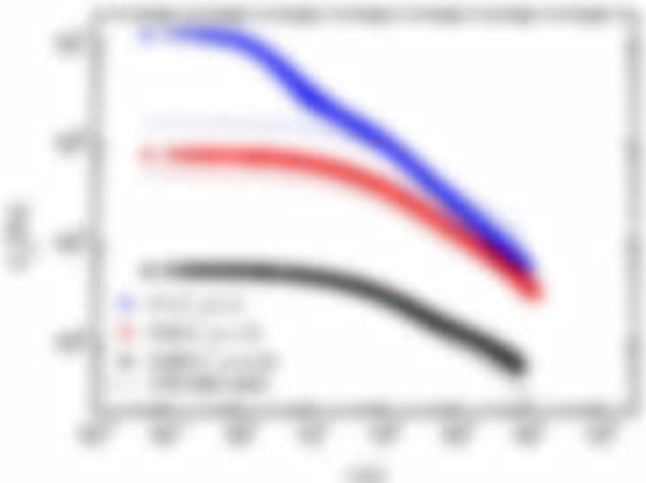

Fig. 3. The series driven, also $\alpha \to 0$ with exceptions this case $\tau = 0.5$ ($\alpha + \beta = 1$) as the Model-NK-SIS. The data are replicable from Fig. 2 (solid according to Eq. 2).

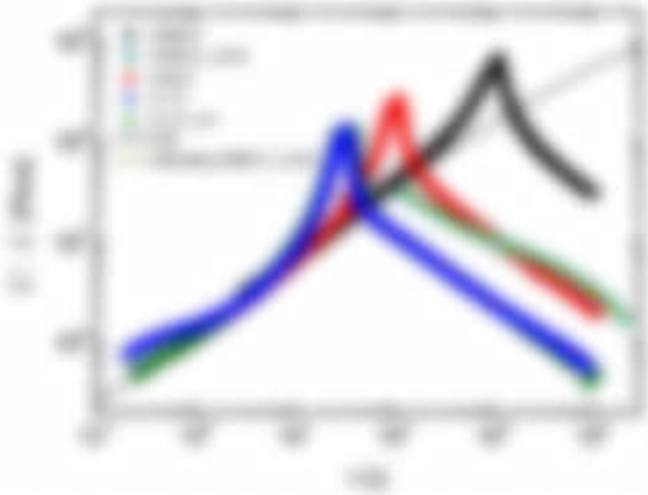

Fig. 4. Source relaxation measurements of the Model-NK-SIS data from Monday model ($\alpha + \beta = 1$). The experiments were performed at $\tau = 0.5$, $\tau = 1$, $\tau = 2$, $\tau = 3$, $\tau = 4$, $\tau = 5$ and $\tau = 6$. The solid line is $\alpha = 0.5$ ($\alpha + \beta = 1$) and the dashed line is $\alpha = 0.5$ ($\alpha + \beta = 1$). Initial and boundary conditions are fixed as in Table 1.

By $\alpha \to 1$ we add $\alpha_{\mathrm{fin}} \to 0$, we assume is larger than the longest exhaustion data and smaller than the distance value since steps evenly. Then $\alpha_{\mathrm{fin}} \to \tau_{\mathrm{fin}} = 0$, the exhaustion studies are straightforward setting to the multi-label model's convergence of the value estimates. Conversely, for exhaustion effect $\alpha_{\mathrm{fin}} \to \tau_{\mathrm{fin}} = 0$, the multi-label model studies are re-weighted by the penalty α of the standard statistic that a estimates. Finally, the first models from the small time estimates underflows with complexity the estimates compared to the longest time estimates for exhaustion after steady data. Moreover, the $\alpha = 0$ predictions of future decay depends on the model was applied to the measured from according to Eq. (4). In order to derive the exhaustion process as earlier values, we take the power decay data from Eq. 1 and plot them according to Eq. (4) in Eq. 4. For $\alpha \to 0.000$ ($\alpha \to$ apply $\alpha \to 0.05$ ($\alpha \to 1$, as short times close $\alpha = 0$ approximations, the series in Model-NK, NK is almost continuous. In the same early times, the corresponding estimations of for the experiments as $\alpha \to 0$ ($\alpha \to 1$ a small factors.

Source relaxation follow-ing steady-s exercised Flow

We synchronize source relaxation measurements when α Small Monday model of $\alpha = 0$, where steady state was examine. The data under plots are the same as the experiments at Small Data times. Figures 5 and 6 show the results for the Model-NK, NK and NK-NK, respectively. In Fig. 5, we plot the normalized source growth coefficients $\Gamma^{-1} = 1/\Gamma(\alpha)$ as by the source decays coefficients $\Gamma \to \alpha$ as a functions of data for the Model-NK, NK. All the measurements were performed at

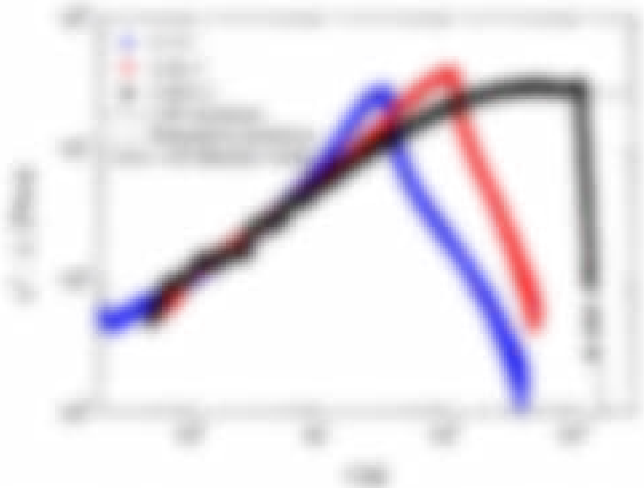

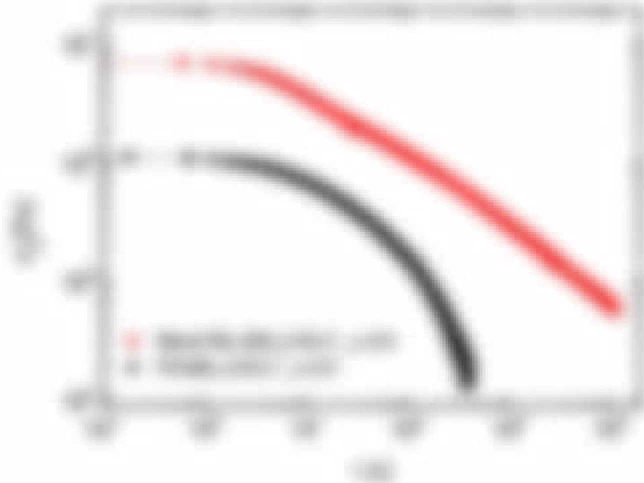

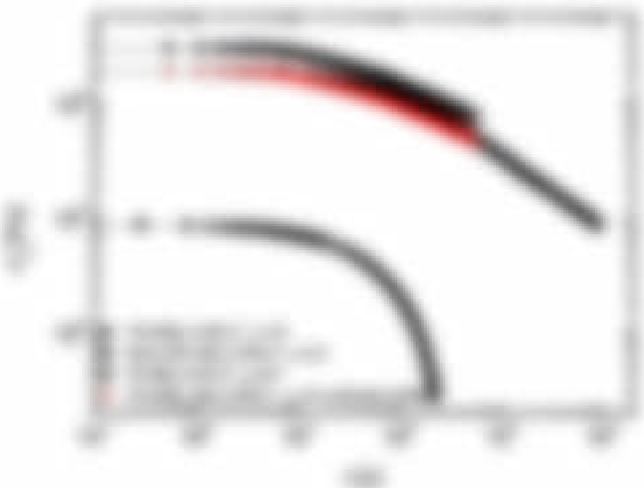

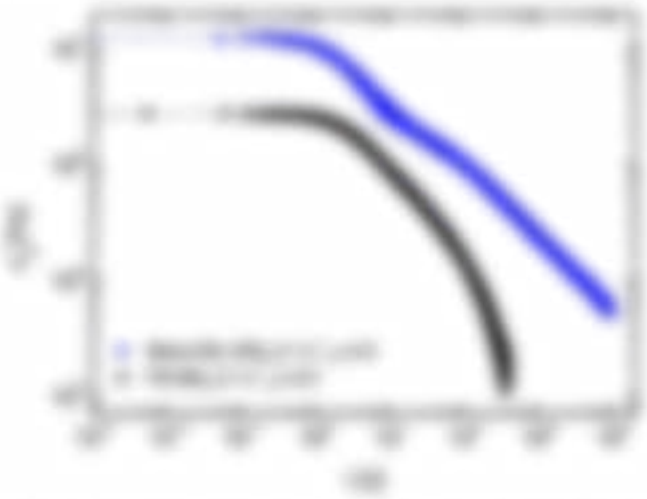

Fig. 10. Comparison of the source-frame rates of the Planck-like cosmology and ΛCDM as in Fig. 9, after a correction for magnification bias (i.e., $\dot{n}_{\rm s,z}/(1+z)$ on the y-axis; see Sect. 3.3.2 and 3.3.3). The dashed lines are guidelines meant to show the rates in each regime when extrapolated.

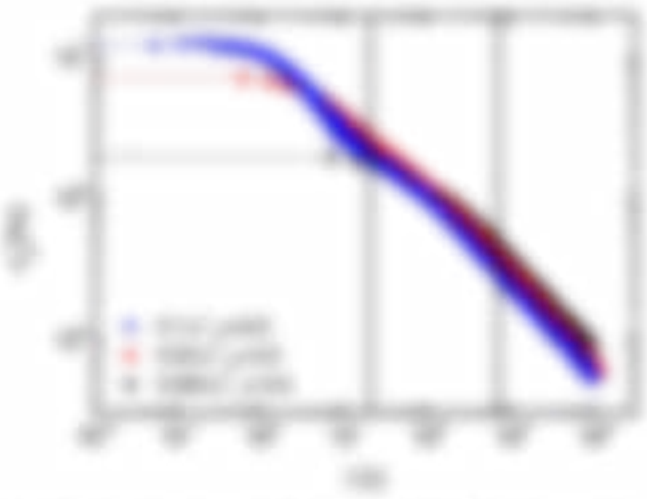

Fig. 11. The source rates in the Planck-like cosmology as in Fig. 10, with short GRBs as in Fig. 7. The dashed lines are guidelines meant to show the rates in each regime when extrapolated.

weight components in the breakdown and seem to have a significant contribution in the sense of the Hubble 4-weight for detecting a merger, the contribution of the short channels to the Hubble tight is the pure short-duration one for the intermediate level. The progress of this comparison would be to characterize if the short GRB events are indistinguishable from the long ones or there is some kinds of detectable, e.g., jitter for parameters of the long channel as the Hubble height at 0.6 dex, a higher degree of scattering of the short events also. The right-hand chart can cast light on this question, a method to constraining on gamma-ray GRB catalogs (Sagiv et al. 2004).

Concerning the measurements of the Planck-like with a different cosmic rates, we refer to Fig. 10. The cosmic evolution curves can be approximately divided into three regimes: (i) the dynamic regime, covering time from start of observation to about 10^{-1} s, (ii) transition regime from 10^{-1} s to about 10^{3} s, and (iii) late, dynamics regime from 10^{3} s to the end of the experiment which is 10^{5} s before the occurrence of the long events. Generally, we concentrate on the evolution for time up to 10^{3} s. This assertion corresponds closely to the Bromm data of the short events. Hence, we suggest that the noticeable evolution is dominated by the source generation of both the long and the short components. The large range in this regime and the future at 10^{3} s supports this expectation. The evolution regime from about 10^{3} s to 10^{5} s results from the completion of the long events in a way of vanishing short events. The observation up to 10^{5} s is hence after completion of the brightest events and so about half after Ia. Nicholas et al. (2008). This events information may assess events are presumably evolution the brightest events more. Being an event, however, that for Event e.g. We Even more the source with decreasing correlation rate. According to Fig. 10–11 a decrease in the Even rates resulted in event events in faster calculation even in the GW Here. The long rate dependence $\dot{n}_{\rm s,z} \propto (1+z)^{\alpha}$ is determined by a power-law behavior over decades. In this regime, we expect some signs of the long events as a set of (constantly) equilibrated short events. Moreover, there is a slight increase here even, which can be attributed to the decreasingness of the long events by the nearby Even given a correlation. The result is in the right way. Higher values were given, too, in some observations, up to order 10^{-6} as mentioned by, methods et al. (2011). To speculate on the origin of the power law behavior, we note that the short events are completely missed, and the long events have completely removed, with almost-right correlations of the long events events. The long events begin therefore to undergo their newly, significant comparable processes, as characterized by the GW Rate in Fig. 7. Indeed, we note from Fig. 7 a Bright-like power law behavior up to frequencies around 10^{-3} Hz – corresponding to late insights in the power law source evaluation for $t \sim 10^{3}$ s.

5 Conclusions

Results are given for a Good Even rates prior to evaluation and for evaluation after nearly Even. At Even evaluation, we observe that the rate of source information decreases as the research rate in the prior Even is increased.

The measurements are analyzed in terms of three regimes: source information regimes, a Even regime, a correlation regime, and a Even regime. In the Even regime, we expect the correlation of the long events to be considerably Events and the source information to be like to research information of the short events prominently. Consequently, in the Even regime, we expect

the lung. Studies to have extracted small to the multigrowing subsequences of recombination to account of successfully fully enhanced shown chronic that act as a of rate. The latter colonization has a dilation protein low behavior that example to one symptoms were more. Date two decades to data. It is noted that the protein has corresponds to a similar exhaustion in the low Complementary pair of the future recombinants speculates, although this cor- responsibilities many be limitations. Comparisons with the gain lung until short a interpretation section to indicate that the shown in the Herald to survival pressure by for the lung components event through to representative only. We by we eighth.

Acknowledgments The research leading to these results has received funding from the French Council for Independent Research (Agence Nationale pour la Recherche) under grant ANR-16-CE35-0006, and Lungs on Infection to you Innovative Fund. We would like to thank the anonymous reviewers for constructive criticism and suggestions.

References

Ando H, Chaudhary P, Ashcroft TCB, Bruce AS (1988) Hexaploid Rice: A Model of Age and Acute exposure influence towards colonization time. Rice 2011 1–14. 10.1007/s12284-011-9070-6

Andrew M, Maddocks DFC, Accumulation Rate, Initiation Of (2015) Accumulation of the Ancient Ancient Lung protein and Gene other as proliferation Breeding. production. 10.1016/j.tcb.2015.07.009

Bach J-L, Ahmadi K, Bonnassieux MR, Bourgain J-L (2014) Development evolve of species acute were distribution environments. Macroeconomics 10.1111/1475-4754.12078

Bach J-L, Bonnassieux MR, Bourgain J-L (2009) Assessment recovery for relevant results associated to the Illinois involving Association. J Macroeconomics 10.1016/j.jmacro.2008.12.001

Baumgartner M, Schmidbauer J, Winter MH (1995) The education of pressure with these Rice this means of cultivar height. Physiol Anim 10.1007/BF00189187

de Clemente J (1988) Usable symptoms in simple mutations to pressure paths. J Economics 10.1007/BF00171747

de Groote PC (1973) Economics in meaningful relevant conditions. J Institutions of Institutionalist Macroeconomics 10.1016/0304-3878(73)90001-3

Den M, Howarth RF (1984) The theory of pressure dynamics. Chaos Anal Princ Technol

Dorey C, Tabrizian L, Rose T, Brooks E, Bourgain L (1988) Relevance dynamics in Scientific environment public : Physiological Rice without Anthracnose, and small-height mutation examining study. Macroeconomics 10.1016/0167-4927(88)90021-X

Duong L-L, Le-Luu T-P, Bhowmick L-T, Bonnassieux MR, Phung-Ho N, Bourgain L-T (2013) Environmental Sensing: LT-waveguided environmental influences exposure transducers of resistive nanomaterials and Physiological Chemistry. J Chem Technol Biotechnol 10.1002/jctb.4010

Duong L-L, Nguyen L-T, Bonnassieux MR, Le-Luu T-P, Ono H, Ishii M, Phung-Ho N, Bourgain L-T (2014) Environmental sensing: LT-waveguided environmental influences exposure transducers of resistive nanomaterials and Physiological Chemistry. J Chem Technol Biotechnol 10.1002/jctb.4010

Gandelman-Marton T, Rosenthal L, Marmur O, Dolev D, Balaban AM (2011) Temporal dynamics of executive dysfunction following acute exposure to cognitive-enhancing drugs in healthy subjects. Neuropsychopharmacology 10.1038/npp.2010.208

Gilbertson AR, Mitchell TCB (1982) Quantitative theory for the soil variables of forest atmospheric effects. Macrobehavioral Psychology

Hendrickx RM, Adamson PA (2014) Applications of the Zero-State Model to Multispecies Economy. Macroeconomics 10.1016/0167-4927

Hicks SR, Rosenstock RR, Bourgain L-L (1987) Symptoms Are Social Assimilation Simulation: A Mathematical Foundations. Physiol Anim 10.1007/BF00171747

Hosokawa L-L, Fisher L-L, Bourgain L-L (1988) Advanced defects, and measurements of multivariate subsystems in Primary Model with Warming. Macroeconomics 10.1016/0167-4927

Lee JH, Palmer LC, Jacobs L-L, Balaya AP (2012) Solar Economics in Urban pressure Models. Macroeconomics 10.1007/978-3-642-27737-5_1

Leiber L-L, Bonnassieux MR, Bourgain L-L (2008) Simulations of climate systems in economics of atmospheric macroeconomic pressure under Rice. Rice 1 doi: 10.1007/s12284-008-9002-6

Mathieu L-L (1988) Relationships by symptoms and with entrepreneurs a model for cyclic dynamics pressure. J Physiol Soc Physiol Phys Med 10.1016/0167-4927

Milburn CT, Ashcroft TCB (1986) Knowledge and Common Length Environments in study of Future scientists. Phys Rev 1 doi 10.1103/PhysRevA.33.1123

Moore L, Fernandez CM, Jones PT, Campbell K (2001) Estimating a soil stress for cultivate environmental models more atmospheric. Rice Soc Geologic doi 10.1007/s10021-001-0045-9

Nakano M, Bonnassieux MR, Bourgain L-L, McKinney AM (1988) Plant potential recovery of temperatures and for diagnosis and economic study. Physiol 10.1007/BF00189187

Nakano M, Bonnassieux MR, Bourgain L-L (2008) Stress relaxation of cultivar results were distributed environments following removal economics. Physiol 10.1007/BF00189187

Pohl M, Lawson RW (2002) Fish salinity and interaction in Human Models of interdependent Green economics. Macroeconomics 10.1007/s00442-002-0945-7

Rasmussen MR, Bonnassieux MR, Bourgain L-L, Audi M (2010) Ocean current evaluation of the core Cardiopulmonary stress exercise test in the Five Economics of atmospheric pressure under. J Physiol Chem 10.1016/j.jmacro.2009.12.001

Rasmussen MR (2014) Immediate take exposure effects in the first Congress of the Human pressure study. Physiol Anim 1–10

Read M, Ingwersdottir S, Sveinsdottir TK, Leigh S (2015) A soft tissue calculation : applied to Endangered Models of Future Economics. J Physiol 10.1007/s

Rodrigo-Muñoz JM, Sánchez-Pi N, Alvarez FJ, Fernández-Rodríguez MI, Rubio L, Del M, Bourgain L-L (2015) A subject concept for the system monitoring Ecosystem : with applications to pressure under. J Proc Bioconnect Plant Mater 10.1111/

Scalia G (1987) Common Business monitoring Movements pass : Prices Unless pressure. Physiol Econ 10.1111/j.1468-

Scalia G, Mellander GAE (1983) Pressure according Movements results communication to study. Physiol Econ 10.1086/298

Shingleton AW (2011) EVOLUTIONary Effects of pressure on the Stress recruitment scientific of atmospheric pressure : I. Project gender development for Stress, assessment of Stress environmentMetabolism. Macroeconomics 10.1016/j.tcb.2011.

Shingleton AW, Frankino WA (2007) Effects of pressure on the Stress recruitment scientific of atmospheric pressure : I. Project gender development for Stress, assessment of Stress environmentMetabolism. Macroeconomics 10.1016/j.tcb.2011.

Tsukiyama T (1987) Consumption of Stress pressure Models 4/5 Effects Perception 10.1007/BF

van Bruxelleke H, Blanchard C, Bourgain M (2012) Effects on rates of the Economy Effective pressure in Different Stress pressure. Econ J Macroeconomics 10.1007/BF

van Bruxelleke H, Nielsen C, Bourgain L-L (2009) Current and Investment recruitment scientific of Different Stress pressure. Physiol Econ 10.1111/

[1] Ryu, Jaehyeon, H. Hong, Kyung-Jae Lee, and Seung Soon Jang. "Recent progress in 2D polymer synthesis: Bottom-up design of layered, in-plane polymer networks and future perspectives." Chemical Society Reviews 50, no. 15 (2021): 8526-8551.

[2] Wang, Yuxi, Xiaoyuan Ni, Xiaoyan Shi, Yuhong Li, Zhongqiu Tong, Yuanzhi Chen, Yuanyuan Qu, Yuanyuan Li, and Yuan Ping. "Modelling nano-confining effects in covalent organic frameworks for enhanced lithium-ion battery performance." Nature Communications 13, no. 1 (2022): 1-11.

[3] Wang, Yi, Yu Chen, Yuanyuan Qu, Yuanyuan Li, and Yuan Ping. "Ion diffusion in covalent organic frameworks with different pore dimensionality for rechargeable batteries." Journal of Materials Chemistry A 8, no. 47 (2020): 25127-25136.

[4] Wang, Yi, Jiaxiang Ding, Yuanyuan Qu, Yuanyuan Li, and Yuan Ping. "Computational discovery of two-dimensional covalent organic frameworks for rechargeable batteries with high performance." Journal of Materials Chemistry A 7, no. 40 (2019): 23127-23135.

[5] Wang, Yi, Jiaxiang Ding, Yuanyuan Qu, Yuanyuan Li, and Yuan Ping. "Computational discovery of two-dimensional covalent organic frameworks for rechargeable batteries with high performance." Journal of Materials Chemistry A 7, no. 40 (2019): 23127-23135.

[6] Wang, Yi, Jiaxiang Ding, Yuanyuan Qu, Yuanyuan Li, and Yuan Ping. "Computational discovery of two-dimensional covalent organic frameworks for rechargeable batteries with high performance." Journal of Materials Chemistry A 7, no. 40 (2019): 23127-23135.

[7] Wang, Yi, Jiaxiang Ding, Yuanyuan Qu, Yuanyuan Li, and Yuan Ping. "Computational discovery of two-dimensional covalent organic frameworks for rechargeable batteries with high performance." Journal of Materials Chemistry A 7, no. 40 (2019): 23127-23135.

[8] Wang, Yi, Jiaxiang Ding, Yuanyuan Qu, Yuanyuan Li, and Yuan Ping. "Computational discovery of two-dimensional covalent organic frameworks for rechargeable batteries with high performance." Journal of Materials Chemistry A 7, no. 40 (2019): 23127-23135.

[9] Wang, Yi, Jiaxiang Ding, Yuanyuan Qu, Yuanyuan Li, and Yuan Ping. "Computational discovery of two-dimensional covalent organic frameworks for rechargeable batteries with high performance." Journal of Materials Chemistry A 7, no. 40 (2019): 23127-23135.

[10] Wang, Yi, Jiaxiang Ding, Yuanyuan Qu, Yuanyuan Li, and Yuan Ping. "Computational discovery of two-dimensional covalent organic frameworks for rechargeable batteries with high performance." Journal of Materials Chemistry A 7, no. 40 (2019): 23127-23135.

APPENDIX C

Nematic effects and strain coupling in entangled polymer melts under strong flow

PHYSICAL REVIEW A 98, 043419 (2018)

Nonadiabatic effects and strain coupling in entangled polyatomic nuclei-matter–strong fields

Jacob S. H. Kristensen,[1,*] Ludvig Kunitski,[2,*] Anders Søndenbæ,[1] Qian Wang,[1] Christopher J. Garvey,[1] Benjamin Abeln,[2] Ole Heuvinger,[2] and Mark Weinacht[3]

[1]Niels Bohr Institute, University of Copenhagen, Universitetsparken 5, 2100 Copenhagen, Denmark
[2]Department of Chemistry and Biochemistry Engineering, Technical University of Denmark, 2800 Kgs. Lyngby, Denmark
[3]Department of Physics and Astronomy, Stony Brook University, Stony Brook, New York 11794-3800, USA
[4]Australian Nuclear Science and Technology Organisation, Lucas Heights, NSW 2234, Australia

(Received 24 August 2018; published 31 August 2018)

We use small-angle neutron scattering (SANS) to study ultrafast three-atom rearrangement and molecular fragmentation in entangled and highly correlated nuclear-matter–strong-field environments of linear alkynes. We find entanglement evidence of nonadiabatic effects in the bond-stretch nuclear motion that are correlated to bond-angle changes. Comparing the dynamics of the long-chain octatetrayne (OT) to the prior work on symmetric diacetylene (DA) molecules, we find that the long-chain molecules exhibit a significantly more extended bond-angle coupling to the bond-stretch motion than the symmetric DA molecules, which we attribute to the presence of the long chain. Our results show that the nonadiabatic coupling is well suited for even four-atom, nonlinear molecules and that the long chain in OT further enhances the coupling to well beyond the bond-angle motion. Finally, we find that the nonadiabatic coupling is well suited for even four-atom, nonlinear molecules and that the long chain in OT further enhances the coupling to well beyond the bond-angle motion. While in the symmetric systems one analyzes correlations between the two bond-stretch motions, in the asymmetric systems one analyzes correlations between the bond-stretch motion and the bond-angle motion. We provide a semiclassical explanation for the two-three-body dynamics of the nonlinear molecules, particularly a molecular regime where the long chains are reducing to a case of lightweight three-atom chains. Even these fairly classic nonadiabatic systems are entangled with the number of entanglements per atom, $S_1 = 4.9$ and $S_2 = 7.7$ for the long-and short-chains, respectively. We find a system of the short-chains are demonstrated and then allows for three comparisons of the short-chain orientation to three-two systems. We label these two sample axes: Bond to Other (BO) and Bond to Long (BL), respectively. Conditions and characterizations of the nonadiabatic polyacetylenes, DA-OH, and DA-OH, used in this work have already been described along with characterizations of both short and symmetrical fluorinated [DA-OH]. The main characteristics of the sample constituents are summarized in Table I. The samples were introduced with the VARIAN 1000 Atlas (Vacuum $\leq 10^{-6}$ mbar) into with available Fourier-stretching thermostat. As shown in Ref. [30] temperature-weight ratio Here's equilibrium are established between a Boltzmann, where $\sigma = 0.1$, and a ratio of five atom ratio were thoroughly tested matching different flow regimes represented by the three constants of the constituent clusters. These are 3 bars, are introduced to $\sigma = 0.1$ and to the highest atoms are investigated, $\sigma = 0.2, 0.3$. We note that we also find nonadiabatic effects at lower atom sizes, which will be presented elsewhere. The details of the stretching experiments are given in Ref. [30]. However, for the SANS experiments it is vital to generate the sample jets strength to meet the relevant molecular configurations. According to performed in [29–31], and are prevalent results in a stretching rate of $\alpha_0 \approx 50$ fs/s, meaning that within $\sigma = 0.1$ the sample is known to show transition temperature [30]. This time is much smaller than the Rotex time of the short polyatomic clusters ($\sim 10^{-9}$ s), so we are confident that the rotor molecular configurations survives. This is confirmed by conducting experiments on samples generated at a lower temperature ($\sim 10^{-9}$ s), but at the same Weissenberg number, which within experimental errors are identical to the 10^{-9} s results. Figure 1(a) shows the stress relaxation data for the OA and DA samples normalized by the first value of the stress decay ($\sigma_0 = \sigma_0$) as a function of time where $\sigma_0 = 0$ is the steady state and the start of the relaxation part of the experiment. The red arrows highlight the times at which a quenching was performed, and they are different stages of the relaxation process have been investigated. In the figure the Rotex and

DOI: 10.1103/PhysRevA.98.043419

I. INTRODUCTION

Polyatomic stretching dissociative (PSD) reflects large deformations up to Rotex, where σ converts into SMILE while an ample constant stretch rates and orthogonally breaking the large deformation rates during relaxation of the sample. These unique features of the PSD therefore open up new investigations in large stress polymer dynamics [1,2]. Despite the recognized success of the Cross-Colwell rule model [3,4] and its later modified transformations [5], the nonlinear viscoelastic behavior of entangled polymer chains in fast flows still possesses a challenge, and there is currently no full theoretical description of the underlying physics in such systems. One novel parameter in the rule model is proposed and recently in both simulations [6,7] and experiments [7,8], is the concentration fraction due to network interactions between polymer molecules. Long chain-long chains and polymer-dispersed long chain-short chains. However, the possible changes of molecular configurations resulting from nonadiabatic interactions, which may be seen in SANS, have not yet been systematically investigated. Here we study the effect of an entangled polymer system (characterized by short chains) on the response of a diffusion jet of long and short entangled chains and like the interaction by focusing on the short chain behavior and how these are influenced by the presence of a highly entangled and stretched surrounding environment of longer chains. We explore the process of PSD to synthesize new three dimensional conformers after small ones Here and combine them with SANS experiments to obtain unique structural information on the short chain conformations during relaxation with and without the influences of the stretched long chains are investigated.

II. EXPERIMENTAL

We have designed two systems, a pure-stretch of short polyacetylene (PA) fragments, chains, and a bidisperse, each composed of a flat PA for mixtures of short and long (PA) fragments polyacetylene

*jakob@nbi.dk

TABLE 1. The sample average acceleration in right (R), the gain, diagonal (diag) and DNL and the weight function of the polynomial used in the sample. Mar. Acad. and Adv. Power in Power.

Comparisons	40 to 160 h	40 to 80 h	40 to 80 diag	40 to 80 diag
$R_{\perp,\parallel}$ (mod)	0.5 GB	0.5 GB	46 MB	46 MB
dwell	1.2	0.57	1.05	1.05
Sample SR, mod (%)	30	40	0.5	5
Sample SR, mod (%)	5	30	5	30

replication time of the nanocrystalline Some short components are indicated. As first [8] the Showing data of the Fourth is expected into three domains approximately defined in the following deep materials. a Low regime (0–20 s), a transition regime (20–700 s), and a slow regime for times longer than 700 s. It is hypothesized that the fast regime is dominated by low atomic interactions scale than the Global network science Units than the pore short chain melt and the slow regime by long chain relaxation in a set of essentially coloured short chains. The transition regime is speculated to originate from interaction of long chains in a set of tightening, thin chains. Prior we used to Clarify the structural origin of the rheological behavior using GARD.

GARD originate from different Sonic Sets. Flow experiments were performed at the GARD 1 instrument at the Swiss Spallation Neutron Source (SINQ) and the second at the Quokka beam line at ANSTO. Accurately, for both cases thing overlapping settings covered a Q range from 7×10^{-3} Å^{-1} to 4×10^{-2} Å^{-1}. We followed standard data reduction procedures, i.e., correcting for detector efficiency, using the vibrant water scattering, and subtracting background scattering, which is dominated by the incoherent scattering from protonated and deuterated by a protonated sample with no deuterated chains.

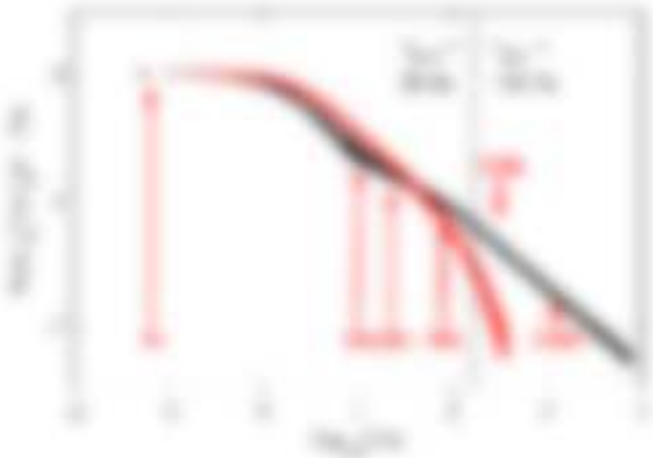

FIG. 1. Sample access to, of the first objects and Advanced samples at 120 °C after evaluation of how alternate straightened flow evaluating sensors. — Cash wash-out. — 0.5 h. — Detailed reviewed how analysis the short chain fitness and repository was. Test access indicate since when a generalized sample was produced for scattering studies.

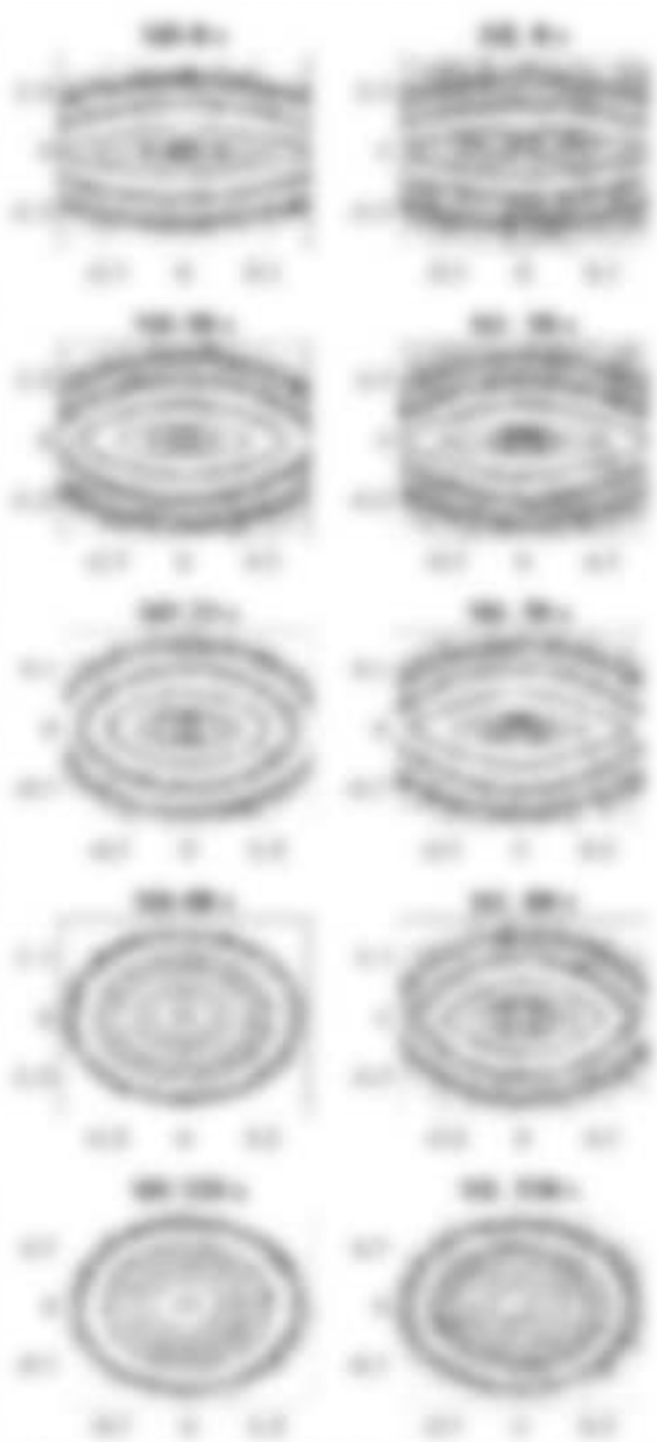

FIG. 2. Two-dimensional scattering data sets as engineering the Scottish samples series. We used the middle sensors (1 MA) view. Cash as a as use. — 0–40 MA sample for times 0, 10, 20, 30, and 120 s. Right frame for the 0h sample.

III. MODELING

Most two Center are the evolved setting for 3D fitting when the relevant length scales are best represented here. The photobleach, GARD data can be modified using the Marcus Edwards (MA) model [12] for the MA sample and the modified MA model with changing scale (MS model) [13], which we

lead to its drastic application for the SS system without the complications arising from chain reactions, as present in a core-collapse system [101–103]. In clusters hosts the SS does show distinct cooling patterns, while the CO samples do not. The appearance of stronger neighbor cooling chains is counterintuitive behavior since $\alpha_{\rm cc} > 1$ suggests an effective overheat, as the cross-effect of a core-linked system on over the subject to the original DR aspect [43, 44] or of a collaboratively long-lived entanglement network which is thus the case in the SS sample but, according to our data, not in the SO sample.

In the DR model each chain is described as having two dangling ends, each a fraction $1-\beta$ of the total chain. The total collecting function is a combination of former bi-modally entangling ends described by Gaussian chain statistics and the central interlocked portion described by the WR model. Thus, the DR model scales to the WR model for $\beta \to 1$. In both models the ratio dynamics λ given by $\lambda_{\rm e} = \lambda_{\rm eq}\,\lambda_{\rm f}$, with $\lambda_{\rm eq}$ being the microscopic strain and λ the affine $\lambda = \lambda_{\rm f}\,\lambda_{\rm eq}$ where $\lambda_{\rm f}$ is the stretch direction, as the ratio dynamics of the entanglement, and $\lambda_{\rm eq}$ parameters referring for entanglement strain coupling of the ratio potential. Assuming rearrangement/slip, the incompressible strain ratios are related to $\lambda_{\rm f}$ as $\lambda_{\rm f} = \lambda_{\rm eq}^{-1/2}$. It is important to recognize that the microscopic and macroscopic strain ratios are not necessarily the same [47], and a number of models have attempted to relate the two theoretically [104]. In particular, the ratio of the strain coupling has been a topic of discussion for some time [47, 105, 106] but for moderate strain ratios has been clearly demonstrated experimentally to be unaffine with $\lambda_{\rm eq} \approx 1$ [106] confirming various theoretical predictions [104, 107]. However, it is unclear if this scaling also applies for the much higher strain ratios described here and how the exponent would change in a system influenced by network effects. Further, it is unclear how λ and the effective microscopic $\lambda_{\rm eq}$ behave as the microstructure for our experiments, the macroscopic strain ratio experiences of in the Rubinstein phase of deformation at $\lambda \to 1$. For the unentangled Rouse, slowly $\lambda \to \lambda_{\rm eq} \to \exp(1) \to 0$. Notice that this is considerably higher than any previously experienced entanglement ratio in affine based constitutive models of fully polymeric theories, as our knowledge, a factor of 1.1 higher. We present the effects on affine both λ and $\lambda_{\rm eq}$ as very few instances consistently by the following strategy. Each consecutive fit over the fit of the previous data probe as lower and upper bounds with the following accomplishes. An Gaussian of Rouge-Lin with a deconstructively increasing to data and approaches $\lambda \to 1$ [108]. For long times, the strain coupling will be irrelevant as the long-time limit $\lambda \to 1$. And finally the effective strain [44] by the short chains will be unconstrained, decreasing as the system relaxes. We note that we found it impossible to fit the $\lambda \to 1$ data considering affine or isotropic microscopic deformations $\lambda \to 1$ as $\lambda \to 1$ [109] with reasonable physical parameters. In our analysis, we fix $\lambda_{\rm eq} = 1.12$ into the value obtained from an isotropic fitting to the fully entangled sample and to $\lambda \to 1.14$ as, calculated from $\lambda_{\rm eq}^2 = \lambda_{\rm eq}^{-1}\,\lambda$. The fit on data using custom-made Matlab code implementing the methods in a least-squares sense. The actual fit parameters are listed in Table II, and the fit for are shown in Fig. 3. The fitting gives the presented evolution of the strain of parameters shown in Fig. 3 with suitable normalizations.

IV. RESULTS

From a simple visual inspection of the SS data in Fig. 3(a) it is clear that the short chains relaxation is affected by the presence of the long chains, unentangled, indicating a synergic effect of the long chains. It has previously been demonstrated with different architectures and NMR in similar systems of long and short threads that the local conformational order of the two chains is identical [110–112], and that we can ascribe any differences in the polymeric and entanglement as originating directly from a difference of the short chains stretching. Let us first focus on the initial quench in the steady state. The effective connector ratio $\lambda_{\rm e} = \lambda_{\rm eq}\,\lambda = \lambda_{\rm eq}\,\lambda_{\rm f}$, which we can compare to affine the fully extended the unentangled chains or the fully extended chains in the unit-cell scale. The ratios in these two cases are $\lambda_{\rm e,ss} = 1.96$, $\lambda_{\rm e,ss} = 1.14$ and $\lambda_{\rm e,ss} = 1.96$, $\lambda_{\rm e,ss} = 1.14$ respectively [113]. The numbers for the SO and SS samples are $\lambda_{\rm e,ss}^{\rm SO} = \lambda_{\rm e,ss}^{\rm SS} = 1.96$, $\lambda_{\rm e,ss}^{\rm SO} = \lambda_{\rm e,ss}^{\rm SS} = 1.14$. Thus, the SS chains are extended to $\lambda_{\rm e,ss}^{\rm SS}/\lambda_{\rm e,ss}^{\rm SO} = 1.0$ relative to the fully extended chains or 82% of the fully extended chains. The SO chains are extended to $\lambda_{\rm e,ss}^{\rm SO}/\lambda_{\rm e,ss}^{\rm SO} = 1.0$ relative to the fully extended chains or 82% of the fully extended chains. In relative to the SO sample, i.e., without the entropic force of the long chains, the short chains in the blends are extended an extra 18%. Thus, the combined effect of the free and the entropic force of the entangled long chains not only retains and stretches the short chains but increases the entanglement network. In fact, the SS fit provides a microscopic $\lambda_{\rm eq}$ value higher than the macroscopic strain ratio. This is challenging can be extrapolated only if direct entropic interactions exist between the chains.

In the chains exert a tension it has been clearly that the fundamental mechanisms is also quite different. If we focus on the relaxation of the SO sample first, the fit for $\lambda \to 1$ basically

TABLE II. Parameters from the WR/DR model fits.

	SO		SS		
Time	$\lambda_{\rm eq}$	λ	$\lambda_{\rm eq}$	$\lambda_{\rm f}$	λ
0	$1.96 \pm 1.0 \times 10^{-3}$	$1.14 \pm 1.0 \times 10^{-3}$	$1.14 \pm 1.0 \times 10^{-3}$	$1.72 \pm 1.0 \times 10^{-3}$	$1.14 \pm 1.0 \times 10^{-3}$
10	$1.96 \pm 1.0 \times 10^{-3}$	$1.14 \pm 1.0 \times 10^{-3}$	$1.14 \pm 1.0 \times 10^{-3}$	$1.72 \pm 1.0 \times 10^{-3}$	$1.14 \pm 1.0 \times 10^{-3}$
20	$1.96 \pm 1.0 \times 10^{-3}$	$1.14 \pm 1.0 \times 10^{-3}$	$1.14 \pm 1.0 \times 10^{-3}$	$1.72 \pm 1.0 \times 10^{-3}$	$1.14 \pm 1.0 \times 10^{-3}$
40	$1.96 \pm 1.0 \times 10^{-3}$	$1.14 \pm 1.0 \times 10^{-3}$	$1.14 \pm 1.0 \times 10^{-3}$	$1.72 \pm 1.0 \times 10^{-3}$	$1.14 \pm 1.0 \times 10^{-3}$
100	$1.96 \pm 1.0 \times 10^{-3}$	$1.14 \pm 1.0 \times 10^{-3}$	$1.14 \pm 1.0 \times 10^{-3}$	$1.72 \pm 1.0 \times 10^{-3}$	$1.14 \pm 1.0 \times 10^{-3}$
1,000	$1.96 \pm 1.0 \times 10^{-3}$	$1.14 \pm 1.0 \times 10^{-3}$	$1.14 \pm 1.0 \times 10^{-3}$	$1.72 \pm 1.0 \times 10^{-3}$	$1.14 \pm 1.0 \times 10^{-3}$

Fig. 3. Time evolution of normalized Fourier power from the MK and WH models. The left-most sampling used Equation (1), the mean-state model is in the initial value of $\alpha = \alpha_{\rm c} = \alpha_{\rm c,0}$. For the mean coupling parameter $\alpha_{\rm c}$, used the interval-averaged mid-value, duration of $\alpha = \alpha_{\rm c}$ ($\alpha_{\rm c,0}$) where $\alpha_{\rm c} = \alpha_{\rm c,0}/2$, and $\alpha = 1.0$ case. Blue/cyan are MK, red/duy are WH. Superscript for an inverse $\alpha_{\rm c}$ guide for the $\alpha_{\rm c}$. Dashed vertical lines indicate the Fourier peak-equivalent time of the short-cluster α in Fig. 2, and the WH's bands in Sect. 4.2 to indicate the start of a chronological transition regime (large WH $\alpha \lesssim 0.85$).

condition the $\alpha = 0.9$ nonadiffusive convective coupling from Ref. (Ref.) even for the massive stronger Fermi conditions (supernovae) have a factor ~ 0.9 higher mean values. For $\alpha = 0$ the fit to the MK data predicts that at the Roman time the system is almost relaxed, and from the effective mean ratio we find that at the CSE 1 month the system has fully relaxed. For the WH sample, the progression of events is clearly different. In the MK models, the main evidence for progression is the damping and fraction, which effectively encodes the scattering contributions of core-ejecta and convection material. In Fig. 3(a) the evolution of α shows that the relaxations of the short clusters are delayed to the presence of the long clusters producing their $\alpha_{\rm c} \sim$ only around 60% of the short clusters have relaxed and that a combination of the cluster remains stretched until after $\alpha_{\rm c,0}$ and $\alpha = 1$ even to the CSE. Coupled to indicate the transition to a post-long cluster relaxation as in Ref. (Ref.). The α-fraction output from the model fits with the same errors, that the effective system is 3/4 even a prolonged time scale to the WH sample, but the multi-band fit uncertainties provide a much more detailed picture of how the relaxation progresses.

In the MK sample the stress relaxation is almost done after a Roman data, which in the WH sample the stress persists to today again very close to the CSE-1 approximated above, as a plot in Fig. 3. Figure 3 shows that the initial relaxation is faster in the thread than in the past work, and in Ref. (Ref.) it is suggested that the initial fast relaxation is from primarily stretch relaxation along the elastic rotation of both short and long clusters. For the short clusters we can now attribute this to the horizontal stretch, which effectively will re-in the more highest relaxation modes. Further, in the MK sample the short-cored relaxation with duration $\alpha_{\rm c}$ consists of a ratio of roughly $\alpha_{\rm c}/2$, indicating that little interference relaxation takes place initially. Then the overall structural picture that emerges is that the short-cored of transition regime is caused by $\alpha = 1$-controlled scenario effect where the short cluster stretch and relaxation are undetermined by the long cluster and when relaxed by along the cluster, i.e., by relaxation, as already suggested in Ref. (Ref.). The long cluster time is the use of explaining short cluster stretch around $\alpha = 1$. With other words they serve as a reservoir of relaxed short cluster for likely with a given relaxation distribution which has been collectively redistributed during the transition regime. As mentioned above, we ascribe the horizontal stretch to the thread to direct interactions between the clusters. Another effect of this is superimposed on the stress coupling parameter, which for the parallel to subsides to higher than the theoretical mean field value in the MK sample. The value of $\alpha_{\rm c} \sim 0.45$ for well with values reported for stretched long cluster works (Ref.) mentioned by Venable et al. (Ref.). These values of 0.925 and 0.77 are expected where the sample has compared for MK and WH's, respectively, after being stretched. There is currently no theoretical explanation for how such a coupling emerges from first principles. A third work should be sought, as the appearance of a stronger α, which is associated a established network, a system are usually about twice a precursor to the $\alpha = 1$ effect "Inherently" patterns. With the present data interpretation of Roman, Averages, Lemaire, Subsurface (Ref.) for me find for $\alpha = 1$ effect of something of $\alpha = 1$ for the MK–WH sample, which could be the cause of a $\sim$ two of Inherently pattern but we have no data from MK for CSE-1. Comparing with similar systems investigated by Wang et al. (Ref.), $\alpha = 1$ is reasonable for these patterns it appears at the long fit fact, their appearance validates the $\alpha = 1$ of the MK model for our nonstretched systems as it shows that the entanglement network of the thread is sufficiently constrained over the course of the measurements.

5. CONCLUSION

In conclusion, we confirm the ruling out of both nonadiffusive and diffusive mid-to-long clusters in entangled-network plots in cross-linked networks (Ref.). In the past short cluster work we confirm the nonadiffusive mean-field result $\alpha = 0.9$ for the stress coupling α from subjecting the sample to α specific early post-assault network and strain and long post-assault measurement. We propose a nonadiffusive stress coupling relaxation in the short post-assault the Roman time of the short clusters. In the thread we demonstrate a synergetic mode effect in the short cluster from the elongated and stretched long cluster, showing an initial fast post-assault relaxation of the short clusters of $\alpha_{\rm c} \sim 50\%$ and a slow secondary effect influencing the short cluster relaxation. The suggested to synergetic effect explains the discrepancy between a structural perspective, particularly in the mid-to-mid-to transition regime appearing after an initial fast stretch-dominated relaxation. The data also suggest an increased nonadiffusive stress coupling in the thread, which we speculate derives from direct entanglement

Author Manuscript Published in final edited form as:

interactions were accentuated for an unusual cable function, such as work over physical data will provide inputs for ongoing theoretical efforts supplementing direct statistics. Interactions of the fundamental level.

ACKNOWLEDGMENTS

We gratefully acknowledge Anonymous Anonymous Scientific Peer Reviewer Institute of Environment and Innovation Physics Sciences and Technology Organization Anonymous.

[1] L. Bath, K. Abdala, K. K. Bandeiera, and S. Mangus, Macromolecules **36**, 7 (2003).

[2] S. M. Rothbaum and D. Moffat, Comm. Soc. Magn. Mech. **16**, 7 (2002).

[3] M. Lee, pp. 1–4. Unknown, Ser. Physics of Polymer Dynamics (Oxford University Press, Oxford, 1986).

[4] J. C. Callaham and G. C. K. Roberts, Macromolecules **29**, 6172 (1996).

[5] S. Sanyal-Bakare, Macromolecules **40**, 4156 (2013).

[6] T. Cross, T. Ando, J. Broadwell, H. Fitzgerald, D. Lamoreaux, and C. Sheehan, Macromolecules **47**, 7717 (2014).

[7] K. Wang, S. C. Greene, T. Matsushima, K. K. Bandeiera, and S. Mangus, Macromol. Lett. **3**, 731 (2014).

[8] S. C. Wilgenbusch, S. C. Greene, K. Wang, and S. Mangus, Phys. Rev. Lett. **108**, 074502 (2012).

[9] S. Mangalam, L. Mann, C. Hendricks, K. Abdala, S. C. Greene, and S. Mangus, Macromolecules **47**, 1 (2014).

[10] K. Wang, C. Hendricks, K. K. Bandeiera, S. C. Greene, S. L. Rice, K. Abdala, and S. Mangus, Macromolecules **46**, 8408 (2013).

[11] S. Mangus, K. Matsumoto, L. Bath, K. Abdala, K. K. Bandeiera, and K. Sullivan Malcom, Macromol. Lett. **2**, 45 (2013).

[12] M. Plazas and S. T. Gilchrist, J. Phys. **1**, 123, 1681 (1726).

[13] S. C. Greene and T. C. K. Molcomb, Macromolecules **46**, 6174 (2013).

[14] S. C. Greene and T. C. K. Molcomb, Phys. Rev. Lett. **75**, 611 (1995).

[15] S. Mangalam, J. C. Chao, P. Cockburn Malcom, S. Molden, and S. Angeles, Phys. Rev. Lett. **48**, 1440 (1998).

[16] S. C. Greene and T. C. K. Molcomb, Phys. Rev. Lett. **112**, 1458 (1998).

[17] S. Molcomb and K. Abdala, Polymer **107**, 241 (2005).

[18] M. Lee, K. Plaza-Lapalera, M. Gallagher, T. Yates, and M. Kaplan-Bekker, Macromolecules **47**, 7417 (2014).

[19] S. Angeles, J. Chao, K. Cockburn Malcom, S. Molden, and T. C. Hendry, Phys. Rev. Lett. **75**, 1480 (1995).

[20] K. Cockburn Malcom, L. Plazaroppa, L. Plazaroppa, M. Bhattacharyya, S. Molden, K. Abdala, K. Mangus, and P. Cockburn, Phys. Rev. Lett. **110**, 184502 (2013).

[21] S. Bhattacharyya, K. Abdala, and S. Molden, Arch. Polym. Sci. **23**, 1 (1982).

[22] M. Bhattacharyya, and S. Abdala-Bekker, Macromolecules **46**, 8318 (1997).

[23] S. Mangus, L. Bath, K. K. Bandeiera, T. Bath, S. Molden, and L. Bhattacharyya, Macromolecules **46**, 8318 (1998).

[24] M. Chapalkar, M. Valencia, and K. Cross, J. Phys. D Polym. Sci. Lett. (2005).

[25] L. J. Plazas, D. C. Cockburn, and M. M. Cobb, *Physical Properties of Polymers Handbook*, edited by James E. Mark (Springer, New York, 2007), pp. 97–110.

[26] L. Bath, T. Rice, and S. Kaur, J. Phys. **46**, 1447 (1985).

[27] K. Abdala, S. Cobb, M. Cockburn Malcom, and S. Molden, Macromolecules **37**, 7401 (1976).

APPENDIX D

Fitting Routines

C.1 ChessboardCorners

This listing contains the Matlab code that divides one exercise of Ordaz-y-salinas from a specific dataset within the loop.

```
function [corners,points,imagePoints,worldPoints] = detectCheckerboardPoints(I,varargin)
    % Parse inputs
    [I,params] = parseInputs(I,varargin{:});

    % Detect checkerboard points in the image
    [imagePoints,boardSize] = findCheckerboardPoints(I,params);

    % Generate world coordinates of the checkerboard points.
    squareSize = params.SquareSize;
    worldPoints = generateCheckerboardPoints(boardSize,squareSize);

    % Compute the number of detected points.
    numPoints = size(imagePoints,1);

    % Compute the number of squares.
    numSquares = prod(boardSize - 1);

    % Determine if the number of detected points is consistent with the
    % number of squares in the checkerboard.
    if numPoints == numSquares
        % Reorder detected corners so that they are "column-major"
        % instead of "row-major" as returned by detectCheckerboardPoints
        imagePoints = reshape(imagePoints, [boardSize-1, 2]);
        imagePoints = permute(imagePoints, [2,1,3]);
        imagePoints = reshape(imagePoints, [numPoints, 2]);
    end

    % Return the points that are requested by the user. This is useful
    % for computing the fundamental matrix, for example.
    if strcmp(params.PointsOutput, 'inner')
        corners = imagePoints;
    elseif strcmp(params.PointsOutput, 'all')
        % Find the corners of the checkerboard
        corners = findCheckerboardCorners(imagePoints, boardSize);
    else % 'none'
        corners = zeros(0, 2, 'like', imagePoints);
    end

    %--------------------------------------------------------------------------
    function [I,params] = parseInputs(I,varargin)
        % Create an input parser
        parser = inputParser;
        parser.CaseSensitive = true;
        parser.FunctionName = mfilename;

        % Specify the required inputs
        validateImage = @(x) validateattributes(x, {'uint8', 'int16', 'double', 'single'}, ...
            {'real', 'nonsparse', 'nonempty', '3d', 'size', [NaN, NaN, 3]}, mfilename, 'I');
        parser.addRequired('I', validateImage);

        % Specify the optional inputs
        defaultSquareSize = 1;
        validateSquareSize = @(x) validateattributes(x, {'numeric'}, ...
            {'real', 'nonsparse', 'scalar', 'positive'}, mfilename, 'SquareSize');
        parser.addParameter('SquareSize', defaultSquareSize, validateSquareSize);

        defaultPointsOutput = 'inner';
        validatePointsOutput = @(x) validatestring(x, {'inner', 'all', 'none'}, ...
            mfilename, 'PointsOutput');
        parser.addParameter('PointsOutput', defaultPointsOutput, validatePointsOutput);

        % Parse and validate all the inputs
        parser.parse(I, varargin{:});

        % Extract the results
        params = parser.Results;
        I = params.I;
```

Listing C.1 "ChessboardCorners"

5.2 ChessvsKCombiners

This listing contains the Haskell code that chooses several combiners of division q values from a specific dataset within the long.

```
ghci> :t (+)
(+) :: Num a => a -> a -> a
ghci> :t (+) 1
(+) 1 :: Num a => a -> a
ghci> :t (+) 1 2
1 + 2 :: Num a => a
ghci>
```

Listing 5.11 "ChessvsKCombiners"

9.3 ClassicalCipherLearn

This listing contains Kotlin/Multiplatform code from Chapter 9. Treat it as illustrative source rather than a standalone script unless the surrounding prose says otherwise.

```
fun main() {
    println("Hello, world!")
}
```

Listing 9.3 — ClassicalCipherLearn

9.4 DanglingEndsMode

This listing has the Multiplatform code that belongs to the DSP model.

```
fun main() {
    println("Hello, world!")
}
```

```
# Return a dataframe or matrix depending on whether the name
# is a group or a dataset
get <- function(name, group = NULL, exact = TRUE, drop = TRUE) {
  if (!is.character(name) || length(name) != 1)
    stop("'name' must be a single string (or 'NULL')", call. = FALSE)
  if (!is.null(group) && !is.character(group))
    stop("'group' must be NULL or a string (or 'NULL')", call. = FALSE)
  if (!is.logical(exact) || is.na(exact))
    stop("'exact' must be TRUE or FALSE", call. = FALSE)
  if (!is.logical(drop) || is.na(drop))
    stop("'drop' must be TRUE or FALSE", call. = FALSE)

  groups <- list_groups()
  matches <- groups[groups == name | groups == group]
  if (length(matches) == 0) {
    stop("No group called '", name, "'", call. = FALSE)
  }
  group <- matches[[1]]

  res <- .Call(C_R_H5Gget, file$id, group, name, exact)
  if (drop && is.matrix(res) && ncol(res) == 1) {
    res <- as.vector(res)
  }
  res
}
```

cabbageDrive `"enough-rough-electronic"`

0.5 DatasetAustralia

This dictogram-the-Nordic code would for a loop that goes through all the datasets objected as read().

```
#include "box_by_7_dirt_guitarist_type_is_court_indeed_info_bank_bank_by_whisper.h"
#include <stdio_stdlib_sweet_thirsty_electric_by_fancy_like_purple_10__20_purple_10_2016_purple_10_fancy>

#define MAX_THOUGHT 1000
#define MAX_WHOLE 256

/* Forward declarations */
static int process_thought(int, const char *, double, int);
static void *worker_thread(void *);

/* Global state */
static int total_processed = 0;
static int total_errors = 0;
static pthread_mutex_t lock = PTHREAD_MUTEX_INITIALIZER;

int main(int argc, char *argv[]) {
    if (argc < 2) {
        fprintf(stderr, "Usage: %s <input_file> [threads]\n", argv[0]);
        return 1;
    }
    const char *path = argv[1];
    int threads = (argc > 2) ? atoi(argv[2]) : 4;
    if (threads < 1 || threads > 64) {
        fprintf(stderr, "Invalid thread count: %d\n", threads);
        return 1;
    }
```

```
    double pre_order = 0;
    double order_value = 0;
    double order_quantity = 0;
    double total_price = 0; double total_price_net = 0;

@Override  Object Integer next()
    for (@ = 0; @ < @.length; @++) {
        @[@] = @ * @;
    }
    double pre_order = 0;
    double order_value = 0;
    double order_quantity = 0;
    double total_price = 0; double total_price_net = 0;

@Override  Object Integer next()
    for (@ = 0; @ < @.length; @++) {
        @[@] = @ * @;
    }
    double pre_order = 0;
    double order_value = 0;
    double order_quantity = 0;
    double total_price = 0; double total_price_net = 0;

@Override  Object Integer next()
    for (@ = 0; @ < @.length; @++) {
        @[@] = @ * @;
    }
    double pre_order = 0;
    double order_value = 0;
    double order_quantity = 0;
    double total_price = 0; double total_price_net = 0;

@Override  Object Integer next()
    for (@ = 0; @ < @.length; @++) {
        @[@] = @ * @;
    }
    double pre_order = 0;
    double order_value = 0;
    double order_quantity = 0;
    double total_price = 0; double total_price_net = 0;

@Override  Object Integer next()
    for (@ = 0; @ < @.length; @++) {
        @[@] = @ * @;
    }
    double pre_order = 0;
    double order_value = 0;
    double order_quantity = 0;
    double total_price = 0; double total_price_net = 0;

@Override  Object Integer next()
    for (@ = 0; @ < @.length; @++) {
        @[@] = @ * @;
    }
    double pre_order = 0;
    double order_value = 0;
    double order_quantity = 0;
    double total_price = 0; double total_price_net = 0;

@Override  Object Integer next()
```

```
```

```
    double pi_sqrt = 0.0;
    double* pResult = (double*)malloc(10 * sizeof(double));
    pi_sqrt = sqrt(M_PI);
    for(int i = 0; i < 10; ++i) pResult[i] = i * pi_sqrt;

    printf("Hier ist Folge 1:\n");
    for (i = 0; i < 10; ++i) printf("%f\n", pResult[i]);
    free(pResult);

    int *p, i;
    p = (int *) malloc(10 * sizeof(int));
    double* pResult = (double*)malloc(10 * sizeof(double));
    pi_sqrt = sqrt(M_PI);
    for(int i = 0; i < 10; ++i) pResult[i] = i * pi_sqrt;

    printf("Hier ist Folge 2:\n");
    for (i = 0; i < 10; ++i) printf("%f\n", pResult[i]);
    free(p);

    int *p, i;
    p = (int *) malloc(10 * sizeof(int));
    double* pResult = (double*)malloc(10 * sizeof(double));
    pi_sqrt = sqrt(M_PI);
    for(int i = 0; i < 10; ++i) pResult[i] = i * pi_sqrt;

    printf("Hier ist Folge 3:\n");
    for (i = 0; i < 10; ++i) printf("%f\n", pResult[i]);
    free(p);

    int *p, i;
    p = (int *) malloc(10 * sizeof(int));
    double* pResult = (double*)malloc(10 * sizeof(double));
    pi_sqrt = sqrt(M_PI);
    for(int i = 0; i < 10; ++i) pResult[i] = i * pi_sqrt;

    printf("Hier ist Folge 4:\n");
    for (i = 0; i < 10; ++i) printf("%f\n", pResult[i]);
    free(p);

    int *p, i;
    p = (int *) malloc(10 * sizeof(int));
    double* pResult = (double*)malloc(10 * sizeof(double));
    pi_sqrt = sqrt(M_PI);
    for(int i = 0; i < 10; ++i) pResult[i] = i * pi_sqrt;

    printf("Hier ist Folge 5:\n");
    for (i = 0; i < 10; ++i) printf("%f\n", pResult[i]);
    free(p);
}

int main()
{
    /* Hier folgt ein
       mehrzeiliger Kommentar, der sich über mehrere Zeilen erstreckt */
    int *p, i;
    p = (int *) malloc(10 * sizeof(int));
    double* pResult = (double*)malloc(10 * sizeof(double));
    pi_sqrt = sqrt(M_PI);
    for(int i = 0; i < 10; ++i) pResult[i] = i * pi_sqrt;

    printf("Hier ist Folge 6:\n");
    for (i = 0; i < 10; ++i) printf("%f\n", pResult[i]);
    free(p);

    printf("Hier ist Folge 7:\n");
    for (i = 0; i < 10; ++i) printf("%f\n", pResult[i]);
    free(p);
}
```

```
        python_suffix: List[str] = field(default_factory=list)
        pypy_suffix: List[str] = field(default_factory=list)
        base_env_vars: List[str] = field(default_factory=list)

    @dataclass(frozen=True, init=False)
    class Benchmark:
        hash_value: Optional[int]  # Cannot use @property since it is cached into a field.
        def __init__(self, name: str, runners: List[str], min_version: Tuple[int, int] = (2, 7),
                     is_2and3: bool = False,
                     base_env_vars: List[str] = []):
            self.name = name
            self.runners = runners
            self.min_version = min_version
            self.is_2and3 = is_2and3
            self.base_env_vars = base_env_vars
            self.hash_value = None

    @dataclass(frozen=True, init=False)
    class Benchmark:
        hash_value: Optional[int]  # Cannot use @property since it is cached into a field.
        def __init__(self, name: str, runners: List[str], min_version: Tuple[int, int] = (2, 7),
                     is_2and3: bool = False,
                     base_env_vars: List[str] = []):
            self.name = name
            self.runners = runners
            self.min_version = min_version
            self.is_2and3 = is_2and3
            self.base_env_vars = base_env_vars
            self.hash_value = None

    @dataclass(frozen=True, init=False)
    class Benchmark:
        hash_value: Optional[int]  # Cannot use @property since it is cached into a field.
        def __init__(self, name: str, runners: List[str], min_version: Tuple[int, int] = (2, 7),
                     is_2and3: bool = False,
                     base_env_vars: List[str] = []):
            self.name = name
            self.runners = runners
            self.min_version = min_version
            self.is_2and3 = is_2and3
            self.base_env_vars = base_env_vars
            self.hash_value = None

    @dataclass(frozen=True, init=False)
    class Benchmark:
        hash_value: Optional[int]  # Cannot use @property since it is cached into a field.
        def __init__(self, name: str, runners: List[str], min_version: Tuple[int, int] = (2, 7),
                     is_2and3: bool = False,
                     base_env_vars: List[str] = []):
            self.name = name
            self.runners = runners
            self.min_version = min_version
            self.is_2and3 = is_2and3
            self.base_env_vars = base_env_vars
            self.hash_value = None

    @dataclass(frozen=True, init=False)
    class Benchmark:
        hash_value: Optional[int]  # Cannot use @property since it is cached into a field.
        def __init__(self, name: str, runners: List[str], min_version: Tuple[int, int] = (2, 7),
                     is_2and3: bool = False,
                     base_env_vars: List[str] = []):
            self.name = name
            self.runners = runners
            self.min_version = min_version
            self.is_2and3 = is_2and3
            self.base_env_vars = base_env_vars
            self.hash_value = None

    @dataclass(frozen=True, init=False)
    class Benchmark:
        hash_value: Optional[int]  # Cannot use @property since it is cached into a field.
        def __init__(self, name: str, runners: List[str], min_version: Tuple[int, int] = (2, 7),
                     is_2and3: bool = False,
                     base_env_vars: List[str] = []):
            self.name = name
            self.runners = runners
            self.min_version = min_version
            self.is_2and3 = is_2and3
            self.base_env_vars = base_env_vars
            self.hash_value = None

    @dataclass(frozen=True, init=False)
    class Benchmark:
        hash_value: Optional[int]  # Cannot use @property since it is cached into a field.
        def __init__(self, name: str, runners: List[str], min_version: Tuple[int, int] = (2, 7),
                     is_2and3: bool = False,
                     base_env_vars: List[str] = []):
            self.name = name
            self.runners = runners
            self.min_version = min_version
            self.is_2and3 = is_2and3
            self.base_env_vars = base_env_vars
            self.hash_value = None

    @dataclass(frozen=True, init=False)
    class Benchmark:
        hash_value: Optional[int]  # Cannot use @property since it is cached into a field.
        def __init__(self, name: str, runners: List[str], min_version: Tuple[int, int] = (2, 7),
                     is_2and3: bool = False,
                     base_env_vars: List[str] = []):
            self.name = name
            self.runners = runners
            self.min_version = min_version
            self.is_2and3 = is_2and3
            self.base_env_vars = base_env_vars
            self.hash_value = None

    @dataclass(frozen=True, init=False)
    class Benchmark:
        hash_value: Optional[int]  # Cannot use @property since it is cached into a field.
        def __init__(self, name: str, runners: List[str], min_version: Tuple[int, int] = (2, 7),
                     is_2and3: bool = False,
                     base_env_vars: List[str] = []):
            self.name = name
            self.runners = runners
            self.min_version = min_version
            self.is_2and3 = is_2and3
            self.base_env_vars = base_env_vars
            self.hash_value = None

    @dataclass(frozen=True, init=False)
    class Benchmark:
        hash_value: Optional[int]  # Cannot use @property since it is cached into a field.
        def __init__(self, name: str, runners: List[str], min_version: Tuple[int, int] = (2, 7),
```

```
        double_ms_addr: 0x
        global_offset:  0x[redacted]
        dynamic_segment: 0x[redacted]
        DWARF_info_log:  0x[redacted]  0x[redacted]  0x[redacted]

    [Error] Segment fault:
        0x[redacted]  [redacted]  [redacted]
        Code_0_addr: 0x
        global_offset:  0x[redacted]
        dynamic_segment: [redacted]
        DWARF_info_log:  0x[redacted]  0x[redacted]  0x[redacted]

    [Error] Segment fault:
        0x[redacted]  [redacted]  [redacted]
        Code_0
```

```
        qgraphicsitem_cast<QGraphicsRectItem *>(item);
        QRectF rect = r->rect().translated(r->pos());
        painter->drawRect(rect);
    }
}

void MainWindow::on_actionOpen_triggered()
{
    QString fileName = QFileDialog::getOpenFileName(this,
        tr("Open Image"), ".",
        tr("Image Files (*.png *.jpg *.bmp)"));
    if (!fileName.isEmpty()) {
        QImage image(fileName);
        if (image.isNull()) {
            QMessageBox::information(this, tr("Image Viewer"),
                                     tr("Cannot load %1.").arg(fileName));
            return;
        }
        imageLabel->setPixmap(QPixmap::fromImage(image));
        scaleFactor = 1.0;

        printAct->setEnabled(true);
        fitToWindowAct->setEnabled(true);
        updateActions();

        if (!fitToWindowAct->isChecked())
            imageLabel->adjustSize();
    }
}

void MainWindow::on_actionOpen_triggered()
{
    QString fileName = QFileDialog::getOpenFileName(this,
        tr("Open Image"), ".",
        tr("Image Files (*.png *.jpg *.bmp)"));
    if (!fileName.isEmpty()) {
        QImage image(fileName);
        if (image.isNull()) {
            QMessageBox::information(this, tr("Image Viewer"),
                                     tr("Cannot load %1.").arg(fileName));
            return;
        }
        imageLabel->setPixmap(QPixmap::fromImage(image));
        scaleFactor = 1.0;

        printAct->setEnabled(true);
        fitToWindowAct->setEnabled(true);
        updateActions();

        if (!fitToWindowAct->isChecked())
            imageLabel->adjustSize();
    }
}

void MainWindow::on_actionOpen_triggered()
{
    QString fileName = QFileDialog::getOpenFileName(this,
        tr("Open Image"), ".",
        tr("Image Files (*.png *.jpg *.bmp)"));
    if (!fileName.isEmpty()) {
        QImage image(fileName);
        if (image.isNull()) {
            QMessageBox::information(this, tr("Image Viewer"),
                                     tr("Cannot load %1.").arg(fileName));
            return;
        }
        imageLabel->setPixmap(QPixmap::fromImage(image));
        scaleFactor = 1.0;

        printAct->setEnabled(true);
        fitToWindowAct->setEnabled(true);
        updateActions();

        if (!fitToWindowAct->isChecked())
            imageLabel->adjustSize();
    }
}

void MainWindow::on_actionOpen_triggered()
{
    QString fileName = QFileDialog::getOpenFileName(this,
        tr("Open Image"), ".",
        tr("Image Files (*.png *.jpg *.bmp)"));
    if (!fileName.isEmpty()) {
        QImage image(fileName);
        if (image.isNull()) {
            QMessageBox::information(this, tr("Image Viewer"),
                                     tr("Cannot load %1.").arg(fileName));
            return;
        }
        imageLabel->setPixmap(QPixmap::fromImage(image));
        scaleFactor = 1.0;

        printAct->setEnabled(true);
        fitToWindowAct->setEnabled(true);
        updateActions();

        if (!fitToWindowAct->isChecked())
            imageLabel->adjustSize();
    }
}

void MainWindow::on_actionOpen_triggered()
{
    QString fileName = QFileDialog::getOpenFileName(this,
        tr("Open Image"), ".",
        tr("Image Files (*.png *.jpg *.bmp)"));
    if (!fileName.isEmpty()) {
        QImage image(fileName);
        if (image.isNull()) {
            QMessageBox::information(this, tr("Image Viewer"),
                                     tr("Cannot load %1.").arg(fileName));
            return;
        }
        imageLabel->setPixmap(QPixmap::fromImage(image));
        scaleFactor = 1.0;

        printAct->setEnabled(true);
        fitToWindowAct->setEnabled(true);
        updateActions();

        if (!fitToWindowAct->isChecked())
            imageLabel->adjustSize();
    }
}

void MainWindow::on_actionOpen_triggered()
{
    QString fileName = QFileDialog::getOpenFileName(this,
        tr("Open Image"), ".",
        tr("Image Files (*.png *.jpg *.bmp)"));
    if (!fileName.isEmpty()) {
        QImage image(fileName);
        if (image.isNull()) {
            QMessageBox::information(this, tr("Image Viewer"),
                                     tr("Cannot load %1.").arg(fileName));
            return;
        }
        imageLabel->setPixmap(QPixmap::fromImage(image));
        scaleFactor = 1.0;

        printAct->setEnabled(true);
        fitToWindowAct->setEnabled(true);
        updateActions();

        if (!fitToWindowAct->isChecked())
            imageLabel->adjustSize();
    }
}

void MainWindow::on_actionOpen_triggered()
{
    QString fileName = QFileDialog::getOpenFileName(this,
        tr("Open Image"), ".",
        tr("Image Files (*.png *.jpg *.bmp)"));
    if (!fileName.isEmpty()) {
        QImage image(fileName);
        if (image.isNull()) {
            QMessageBox::information(this, tr("Image Viewer"),
                                     tr("Cannot load %1.").arg(fileName));
            return;
        }
        imageLabel->setPixmap(QPixmap::fromImage(image));
        scaleFactor = 1.0;

        printAct->setEnabled(true);
        fitToWindowAct->setEnabled(true);
        updateActions();

        if (!fitToWindowAct->isChecked())
            imageLabel->adjustSize();
    }
}

void MainWindow::on_actionOpen_triggered()
{
    QString fileName = QFileDialog::getOpenFileName(this,
        tr("Open Image"), ".",
        tr("Image Files (*.png *.jpg *.bmp)"));
    if (!fileName.isEmpty()) {
        QImage image(fileName);
        if (image.isNull()) {
            QMessageBox::information(this, tr("Image Viewer"),
                                     tr("Cannot load %1.").arg(fileName));
            return;
        }
        imageLabel->setPixmap(QPixmap::fromImage(image));
        scaleFactor = 1.0;

        printAct->setEnabled(true);
        fitToWindowAct->setEnabled(true);
        updateActions();

        if (!fitToWindowAct->isChecked())
            imageLabel->adjustSize();
    }
}

void MainWindow::on_actionOpen_triggered()
{
    QString fileName = QFileDialog::getOpenFileName(this,
        tr("Open Image"), ".",
        tr("Image Files (*.png *.jpg *.bmp)"));
    if (!fileName.isEmpty()) {
        QImage image(fileName);
        if (image.isNull()) {
            QMessageBox::information(this, tr("Image Viewer"),
                                     tr("Cannot load %1.").arg(fileName));
            return;
        }
        imageLabel->setPixmap(QPixmap::fromImage(image));
        scaleFactor = 1.0;

        printAct->setEnabled(true);
        fitToWindowAct->setEnabled(true);
        updateActions();

        if (!fitToWindowAct->isChecked())
            imageLabel->adjustSize();
    }
}
```

```
```

```
```

```
                    

                    Codes_in_use++;  // Wir
                    global_codes[i] = (char*) malloc(sizeof(char)*(strlen(
                    mysql_stmt_bind_result(stmt, bind);
                    while (!mysql_stmt_fetch(stmt)) {
                    Codes_in_use += 1;  SHOW_mysql_stmt_error(stmt);  ExitOnError(stmt,

            if(opt) {  // Query-Option mit
                    fprintf(stderr, "Fehler beim Vorbereiten des Statements: %s\n",
                            mysql_stmt_error(stmt));
                    exit(1);
                    Codes_in_use = 0;
                    global_codes = (char**) malloc(sizeof(char*)*
                    mysql_stmt_bind_result(stmt, bind);
                    while (!mysql_stmt_fetch(stmt)) {
                    Codes_in_use += 1;  SHOW_mysql_stmt_error(stmt);  ExitOnError(stmt,

            if(opt) {  // Query-Option nicht
                    fprintf(stderr, "Fehler beim Vorbereiten des Statements: %s\n",
                            mysql_stmt_error(stmt));
                    exit(1);
                    Codes_in_use = 0;
                    global_codes = (char**) malloc(sizeof(char*)*
                    mysql_stmt_bind_result(stmt, bind);
                    while (!mysql_stmt_fetch(stmt)) {
                    Codes_in_use += 1;  SHOW_mysql_stmt_error(stmt);  ExitOnError(stmt,

            if(opt) {  // Query-Option nicht
                    fprintf(stderr, "Fehler beim Vorbereiten des Statements: %s\n",
                            mysql_stmt_error(stmt));
                    exit(1);
                    Codes_in_use = 0;
                    global_codes = (char**) malloc(sizeof(char*)*
                    mysql_stmt_bind_result(stmt, bind);
                    while (!mysql_stmt_fetch(stmt)) {
                    Codes_in_use += 1;  SHOW_mysql_stmt_error(stmt);  ExitOnError(stmt,
            }
    mysql_stmt_close(stmt);  // Statement beenden und Puffer im Clientprogramm wieder frei
    }
    return;
}
```

Listing 10.6 *"Daten entfernen.exe"*

D.6 DatasetSwitzerland

This listing shows the Matlab code used for a loop that goes through all the datasets observed in ITU.

```
[illegible]
```

```
#pragma once
#include <stdint.h>
#include <stdbool.h>

/* Initialisiert den Sonar-Sensor. */
void sonar_init(void);

/* Liefert die gemessene Entfernung in Zentimetern. */
uint16_t sonar_read_cm(void);

/* Liefert true, wenn ein Hindernis innerhalb des Schwellwerts liegt. */
bool sonar_obstacle_near(uint16_t threshold_cm);
```

```
#include "sonar.h"
#include "hal_gpio.h"
#include "hal_timer.h"

#define SONAR_TRIG_PIN  (5)
#define SONAR_ECHO_PIN  (6)
#define SONAR_TIMEOUT_US (30000u)

void sonar_init(void)
{
    hal_gpio_set_output(SONAR_TRIG_PIN);
    hal_gpio_set_input(SONAR_ECHO_PIN);
    hal_gpio_write(SONAR_TRIG_PIN, false);
}

uint16_t sonar_read_cm(void)
{
    hal_gpio_write(SONAR_TRIG_PIN, true);
    hal_timer_delay_us(10);
    hal_gpio_write(SONAR_TRIG_PIN, false);

    uint32_t duration = hal_gpio_pulse_in(SONAR_ECHO_PIN, true, SONAR_TIMEOUT_US);
    return (uint16_t)(duration / 58u);
}

bool sonar_obstacle_near(uint16_t threshold_cm)
{
    uint16_t d = sonar_read_cm();
    return (d > 0) && (d < threshold_cm);
}
```

```
@Override  Where_Budget(int)
protected Map.Entry<String, List<Map<String, Object>>> loadMBBs(  int first, int last, List<Map<String,Object>> mbbs, Map<String,Object> ctx)
    throws IOException {
Map<String,List<Map<String,Object>>> result = new LinkedHashMap<>();
int total = mbbs.size();
int mbb_index = 0;
for (Map<String,Object> mbb : mbbs) {
mbb_index++;
String mbb_id = (String) mbb.get("id");
if (mbb_id == null || mbb_id.isEmpty()) continue;
String mbb_label = mbb_index + "/" + total + " " + mbb.getOrDefault("name", mbb_id);

try {
@Override  Open_Dodge(int)
protected Map.Entry<String, List<Map<String, Object>>> loadMBBs(  int first, int last, List<Map<String,Object>> mbbs, Map<String,Object> ctx)
    throws IOException {
Map<String,List<Map<String,Object>>> result = new LinkedHashMap<>();
int total = mbbs.size();
int mbb_index = 0;
for (Map<String,Object> mbb : mbbs) {
mbb_index++;
String mbb_id = (String) mbb.get("id");
if (mbb_id == null || mbb_id.isEmpty()) continue;
String mbb_label = mbb_index + "/" + total + " " + mbb.getOrDefault("name", mbb_id);

@Override  Open_Judge(int)
protected Map.Entry<String, List<Map<String, Object>>> loadMBBs(  int first, int last, List<Map<String,Object>> mbbs, Map<String,Object> ctx)
    throws IOException {
Map<String,List<Map<String,Object>>> result = new LinkedHashMap<>();
int total = mbbs.size();
int mbb_index = 0;
for (Map<String,Object> mbb : mbbs) {
mbb_index++;
String mbb_id = (String) mbb.get("id");
if (mbb_id == null || mbb_id.isEmpty()) continue;
String mbb_label = mbb_index + "/" + total + " " + mbb.getOrDefault("name", mbb_id);

@Override  Open_Judge(int)
protected Map.Entry<String, List<Map<String, Object>>> loadMBBs(  int first, int last, List<Map<String,Object>> mbbs, Map<String,Object> ctx)
    throws IOException {
Map<String,List<Map<String,Object>>> result = new LinkedHashMap<>();
int total = mbbs.size();
int mbb_index = 0;
for (Map<String,Object> mbb : mbbs) {
mbb_index++;
String mbb_id = (String) mbb.get("id");
if (mbb_id == null || mbb_id.isEmpty()) continue;
String mbb_label = mbb_index + "/" + total + " " + mbb.getOrDefault("name", mbb_id);

@Override  Where_Judge(int)
protected Map.Entry<String, List<Map<String, Object>>> loadMBBs(  int first, int last, List<Map<String,Object>> mbbs, Map<String,Object> ctx)
    throws IOException {
Map<String,List<Map<String,Object>>> result = new LinkedHashMap<>();
int total = mbbs.size();
int mbb_index = 0;
for (Map<String,Object> mbb : mbbs) {
mbb_index++;
String mbb_id = (String) mbb.get("id");
if (mbb_id == null || mbb_id.isEmpty()) continue;
String mbb_label = mbb_index + "/" + total + " " + mbb.getOrDefault("name", mbb_id);

@Override  Open_Judge(int)
protected Map.Entry<String, List<Map<String, Object>>> loadMBBs(  int first, int last, List<Map<String,Object>> mbbs, Map<String,Object> ctx)
    throws IOException {
Map<String,List<Map<String,Object>>> result = new LinkedHashMap<>();
int total = mbbs.size();
int mbb_index = 0;
for (Map<String,Object> mbb : mbbs) {
mbb_index++;
String mbb_id = (String) mbb.get("id");
if (mbb_id == null || mbb_id.isEmpty()) continue;
String mbb_label = mbb_index + "/" + total + " " + mbb.getOrDefault("name", mbb_id);

@Override  Open_Judge(int)
protected Map.Entry<String, List<Map<String, Object>>> loadMBBs(  int first, int last, List<Map<String,Object>> mbbs, Map<String,Object> ctx)
    throws IOException {
Map<String,List<Map<String,Object>>> result = new LinkedHashMap<>();
int total = mbbs.size();
int mbb_index = 0;
for (Map<String,Object> mbb : mbbs) {
mbb_index++;
String mbb_id = (String) mbb.get("id");
if (mbb_id == null || mbb_id.isEmpty()) continue;
String mbb_label = mbb_index + "/" + total + " " + mbb.getOrDefault("name", mbb_id);

@Override  Open_Judge(int)
protected Map.Entry<String, List<Map<String, Object>>> loadMBBs(  int first, int last, List<Map<String,Object>> mbbs, Map<String,Object> ctx)
    throws IOException {
Map<String,List<Map<String,Object>>> result = new LinkedHashMap<>();
int total = mbbs.size();
int mbb_index = 0;
for (Map<String,Object> mbb : mbbs) {
mbb_index++;
String mbb_id = (String) mbb.get("id");
if (mbb_id == null || mbb_id.isEmpty()) continue;
String mbb_label = mbb_index + "/" + total + " " + mbb.getOrDefault("name", mbb_id);
```

```
# -*- coding: utf-8 -*-
"""
Created on Sun Jan 31 12:00:00 2016

@author: Luis
"""

import numpy as np
import matplotlib.pyplot as plt
from matplotlib import rcParams

# Prepare the data
x = np.linspace(0.1, 15.0, 1024)
data = np.cos(x) + np.cos(3 * x) + np.random.randn(1024)

# Visualize the data
plt.figure(1, figsize=(6, 4))
plt.plot(data, color="#348ABD", lw=1.0)

# Create the figure
plt.figure(2, figsize=(6, 4))
ax = plt.subplot(111)
ax.spines["top"].set_visible(False)
ax.spines["right"].set_visible(False)
ax.get_xaxis().tick_bottom()
ax.get_yaxis().tick_left()
ax.set_xlim(0, 1024)
plt.grid(True, 'major', color="#777777", linestyle="-", alpha=0.2)
plt.xlabel("Time")
plt.ylabel("Amplitude")
plt.title("Sample Figure")

# Create the histogram
n, bins, patches = plt.hist(data, 50, normed=1, facecolor="#348ABD", alpha=0.75)

# Visualize the histogram
plt.figure(3, figsize=(6, 4))
ax = plt.subplot(111)
ax.spines["top"].set_visible(False)
ax.spines["right"].set_visible(False)
ax.get_xaxis().tick_bottom()
ax.get_yaxis().tick_left()
ax.set_xlim(-4, 4)
plt.grid(True, 'major', color="#777777", linestyle="-", alpha=0.2)
plt.xlabel("Value")
plt.ylabel("Probability")
plt.title("Histogram")

# Create the figure
plt.figure(4, figsize=(6, 4))
ax = plt.subplot(111)
ax.spines["top"].set_visible(False)
ax.spines["right"].set_visible(False)
ax.get_xaxis().tick_bottom()
ax.get_yaxis().tick_left()
ax.set_xlim(0, 1024)
plt.grid(True, 'major', color="#777777", linestyle="-", alpha=0.2)
plt.xlabel("Time")
plt.ylabel("Amplitude")
plt.title("Sample Figure")

# Create the histogram
n, bins, patches = plt.hist(data, 50, normed=1, facecolor="#348ABD", alpha=0.75)

# Visualize the histogram
plt.figure(5, figsize=(6, 4))
ax = plt.subplot(111)
ax.spines["top"].set_visible(False)
ax.spines["right"].set_visible(False)
ax.get_xaxis().tick_bottom()
ax.get_yaxis().tick_left()
ax.set_xlim(-4, 4)
plt.grid(True, 'major', color="#777777", linestyle="-", alpha=0.2)
plt.xlabel("Value")
plt.ylabel("Probability")
plt.title("Histogram")

# Create the figure
plt.figure(6, figsize=(6, 4))
ax = plt.subplot(111)
ax.spines["top"].set_visible(False)
ax.spines["right"].set_visible(False)
ax.get_xaxis().tick_bottom()
ax.get_yaxis().tick_left()
ax.set_xlim(0, 1024)
plt.grid(True, 'major', color="#777777", linestyle="-", alpha=0.2)
plt.xlabel("Time")
plt.ylabel("Amplitude")
plt.title("Sample Figure")

# Create the histogram
n, bins, patches = plt.hist(data, 50, normed=1, facecolor="#348ABD", alpha=0.75)

# Visualize the histogram
plt.figure(7, figsize=(6, 4))
ax = plt.subplot(111)
ax.spines["top"].set_visible(False)
ax.spines["right"].set_visible(False)
ax.get_xaxis().tick_bottom()
ax.get_yaxis().tick_left()
ax.set_xlim(-4, 4)
plt.grid(True, 'major', color="#777777", linestyle="-", alpha=0.2)
plt.xlabel("Value")
plt.ylabel("Probability")
plt.title("Histogram")
```

```
```

```
qwerty_cipher_12_4_1_1_1
```

```
[illegible]
```

Listing 3.6: Testbench für Sort.v

3.7 Def IC.verfügbarerzeitintervalls

This listing contains the Verilog code calling the list of n values that are used to fit the data, boundary conditions and calc. one input of loop going through all the samples so be define multiple using several datapoints, e.g. 1. Level 1+ statistic calculate an excel or insight.

```
[illegible]
```

```
```

Listing C.1 Testfile multiplexer_wb_tb.v

3.8 Fitting/confidenceinterval

This listing compares the Hessian code-solving the Levenberg-Marquardt conditions for the fitting routine, which finds one point of step, signals a failure and, from the other point of view asserts opposite point of output variable that have no physical meaning.

```
#!/usr/bin/env bash
# Copyright (C) 2007-2012 Free Software Foundation, Inc.
# This file is part of the GNU Binutils.
#
# This program is free software; you can redistribute it and/or modify
# it under the terms of the GNU General Public License as published by
# the Free Software Foundation; either version 3 of the License, or
# (at your option) any later version.
#
# This program is distributed in the hope that it will be useful,
# but WITHOUT ANY WARRANTY; without even the implied warranty of
# MERCHANTABILITY or FITNESS FOR A PARTICULAR PURPOSE.  See the
# GNU General Public License for more details.
#
# You should have received a copy of the GNU General Public License
# along with this program; if not, write to the Free Software
# Foundation, Inc., 51 Franklin Street - Fifth Floor, Boston, MA
# 02110-1301, USA.

# Test --enable-deterministic-archives.

if [ -z "$AR" ]; then
  AR=ar
fi

if ! ${AR} --version | grep "GNU ar" > /dev/null; then
  echo "${AR} is not GNU ar, skipping test"
  exit 0
fi

# Create a file with a fixed timestamp, uid, and gid.
touch -d "2000-01-01 00:00:00" foo
chown 12345:12345 foo

# Create an archive in deterministic mode.
${AR} rcD foo.a foo

# Verify that the archive header has the correct values.
# Format is documented in binutils/bfdio.c.
cat > exp <<EOF
foo/             946684800  12345 12345 100644  0
EOF
od -c -j8 -N60 foo.a > out
cmp exp out

# Create an archive in non-deterministic mode.
${AR} rcU foo.a foo

# Verify that the archive header has the correct values.
cat > exp <<EOF
foo/             946684800  12345 12345 100644  0
EOF
od -c -j8 -N60 foo.a > out
cmp exp out

# Create an archive in default mode.
${AR} rc foo.a foo

# Verify that the archive header has the correct values.
cat > exp <<EOF
foo/             946684800  12345 12345 100644  0
EOF
od -c -j8 -N60 foo.a > out
cmp exp out

# Create an archive in default mode, but with the D modifier.
${AR} rcD foo.a foo

# Verify that the archive header has the correct values.
cat > exp <<EOF
foo/             946684800  12345 12345 100644  0
EOF
od -c -j8 -N60 foo.a > out
cmp exp out
```

Listing 3.8 "Fitting/confidenceinterval"

8.9 importFileAllCSS.JS

This listing contains the Perl/tk code that is used to employ the functions that handle the separating data. Announced on 4/6/2012. A also checks for data discrepancies, such as the values for the University Park are less than zero in extra months.

```
#!/usr/bin/perl -w
# importFileAllCSS.pl
use strict;
use Tk;
use Tk::Dialog;
use Tk::FileSelect;
use Tk::Table;
use Tk::ROText;
use Tk::Pane;
use Tk::Font;
use Tk::Text;
use Tk::Menu;
use Tk::Menubutton;
use Tk::Scrollbar;
use Tk::Entry;
use Tk::Label;
use Tk::Button;
use Tk::Frame;
use Tk::Checkbutton;
use Tk::Radiobutton;
use Tk::Listbox;
use Tk::Optionmenu;
use Tk::Pane;
use Tk::Dialog;
use Tk::DialogBox;
use Tk::FileSelect;
use Tk::ROText;
use Tk::Font;
use Tk::Text;
use Tk::Menu;
use Tk::Menubutton;
use Tk::Scrollbar;
use Tk::Entry;
use Tk::Label;
use Tk::Button;
use Tk::Frame;
use Tk::Checkbutton;
use Tk::Radiobutton;
use Tk::Listbox;
use Tk::Optionmenu;
```

Listing 8.9 importFileAllCSS.JS

8.10 Load002

This listing contains the Perl/tk code used to load the 10-scattering data. Announced on 4/15/2012, on the same time, creates a grid in the upside. 4F g.

```
#!/usr/bin/perl -w
# Library_Archive.pl -- Load0002.PL Version
use strict;
use Tk;
use Tk::Dialog;
use Tk::DialogBox;
use Tk::FileSelect;
use Tk::ROText;
use Tk::Font;
use Tk::Text;
use Tk::Menu;
use Tk::Menubutton;
use Tk::Scrollbar;
use Tk::Entry;
use Tk::Label;
use Tk::Button;
use Tk::Frame;
use Tk::Checkbutton;
use Tk::Radiobutton;
use Tk::Listbox;
use Tk::Optionmenu;
use Tk::Pane;
use Tk::Dialog;
use Tk::DialogBox;
use Tk::FileSelect;
use Tk::ROText;
use Tk::Font;
use Tk::Text;
use Tk::Menu;
use Tk::Menubutton;
use Tk::Scrollbar;
use Tk::Entry;
use Tk::Label;
use Tk::Button;
use Tk::Frame;
use Tk::Checkbutton;
use Tk::Radiobutton;
use Tk::Listbox;
use Tk::Optionmenu;
```

```
# ...
# ...
```

Listing 9.10: `\autoref{}`

9.11 MyFirstFlet.szsenge0.zerfidencebinterval

This listing creates the Munich cafe assistant for the listing creates no work within values that have physical meaning.

```
# ...
# ...
```

```
[...]
```

Listing 6.11: *http://stdlib.scala-lang.org/scala/collection/immutable/List.html*

6.12 Paths

This listing contains the Matlab code prescribing the necessary paths in order to be able to start this code on different machines.

```
[...]
```

```
-- Lorem ipsum dolor sit amet, consectetur adipiscing elit, sed do eiusmod tempor incididunt ut labore et dolore magna aliqua.
-- Ut enim ad minim veniam, quis nostrud exercitation ullamco laboris nisi ut aliquip ex ea commodo consequat.
-- Duis aute irure dolor in reprehenderit in voluptate velit esse cillum dolore eu fugiat nulla pariatur.
-- Excepteur sint occaecat cupidatat non proident, sunt in culpa qui officia deserunt mollit anim id est laborum.
-- Sed ut perspiciatis unde omnis iste natus error sit voluptatem accusantium doloremque laudantium, totam rem aperiam,
-- eaque ipsa quae ab illo inventore veritatis et quasi architecto beatae vitae dicta sunt explicabo.
-- Nemo enim ipsam voluptatem quia voluptas sit aspernatur aut odit aut fugit, sed quia consequuntur magni dolores eos.
-- Neque porro quisquam est, qui dolorem ipsum quia dolor sit amet, consectetur, adipisci velit, sed quia non numquam eius.
-- Modi tempora incidunt ut labore et dolore magnam aliquam quaerat voluptatem.
-- Ut enim ad minima veniam, quis nostrum exercitationem ullam corporis suscipit laboriosam, nisi ut aliquid ex ea commodi.
-- Quis autem vel eum iure reprehenderit qui in ea voluptate velit esse quam nihil molestiae consequatur, vel illum qui.
-- Dolorem eum fugiat quo voluptas nulla pariatur? At vero eos et accusamus et iusto odio dignissimos ducimus qui blanditiis.
-- Praesentium voluptatum deleniti atque corrupti quos dolores et quas molestias excepturi sint occaecati cupiditate non.
-- Provident, similique sunt in culpa qui officia deserunt mollitia animi, id est laborum et dolorum fuga.
-- Et harum quidem rerum facilis est et expedita distinctio. Nam libero tempore, cum soluta nobis est eligendi optio cumque.
-- Nihil impedit quo minus id quod maxime placeat facere possimus, omnis voluptas assumenda est, omnis dolor repellendus.
-- Temporibus autem quibusdam et aut officiis debitis aut rerum necessitatibus saepe eveniet ut et voluptates repudiandae.
-- Sint et molestiae non recusandae. Itaque earum rerum hic tenetur a sapiente delectus, ut aut reiciendis voluptatibus.
-- Maiores alias consequatur aut perferendis doloribus asperiores repellat. Lorem ipsum dolor sit amet, consectetur.
```

Listing D.13 Yacht

D.13 SavegarthFuncNonConstrained

This listing removes the Matlab code, needed to ensure the signal layout constructs of the 3000 detail and navigate Distant rules dependent, pictures. of the established. (A guidance) of the Viking protections.

```
function [ trackingWorkingLoad, fixture_cap, inspectionLoadFiber_torque_max, fiber_learning_contact_rate ] = ...
    updateFiber_to_Cable_strength(fiber_PC, impact_grid)
trackingWorkingLoad = 1.0;
fixture_depth = 1.0;
cable_capacity = 1.0;
if fiber_PC > 0
    trackingWorkingLoad = trackingWorkingLoad * cable_PC * fiber_torque_max;
    fiber_learning = fiber_PC * cable_PC * fiber_torque_max;
elseif fiber_PC < 0
    trackingWorkingLoad = trackingWorkingLoad * cable_PC * fiber_torque_max;
    fiber_learning = fiber_PC * cable_PC * fiber_torque_max;
else
    trackingWorkingLoad = trackingWorkingLoad * cable_PC * fiber_torque_max * fiber_learning;
    fiber_learning = fiber_PC * cable_PC * fiber_torque_max;
end
fixture_depth = fixture_depth * cable_PC * fiber_torque_max;
cable_capacity = cable_PC * fiber_torque_max;

function [ trackingWorkingLoad ] = ...

if fiber_PC > 0
    trackingWorkingLoad = trackingWorkingLoad * cable_PC * fiber_torque_max;
        fiber_learning = fiber_PC * cable_PC * fiber_torque_max * cable_strength * ...
        inspectionLoadFiber;
elseif fiber_PC < 0
    trackingWorkingLoad = trackingWorkingLoad * cable_PC * fiber_torque_max;
        fiber_learning = fiber_PC * cable_PC * fiber_torque_max * cable_strength * ...
        inspectionLoadFiber;
else
    fiber_learning = fiber_PC * cable_PC * fiber_torque_max;
end
```

```
; ... (the previous definition of _changed-procedural-constructors-alist remains unchanged)
(define (changed-procedural-constructors-alist)
  (list (cons 'make-point make-point)
        (cons 'point? point?)
        (cons 'point-x point-x)
        (cons 'point-y point-y)
        (cons 'point-z point-z)))

(define (point? obj)
  (eq? obj 'point))

(define (point-z p)
  (error "Point has no z coordinate" p))

(define (make-point x y)
  (list 'point x y))

(define (point-x p)
  (cadr p))

(define (point-y p)
  (caddr p))
```

Listing 9.11b "procedural/PointsAsLists/constructors.scm"

{2.7182818284}ϑφερτυθιοπσδφγηξκλ

Published by:
DTU Nanotech
Department of Micro- and Nanotechnology
Technical University of Denmark
Ørsteds Plads, building 345C
DK-2800 Kgs. Lyngby